FOSSIL ENERGY

DOE/NBM-3007365
(DE83007365)

EVALUATION OF ADVANCED MATERIALS FOR SLURRY EROSION SERVICE

Final Report

By
I. G. Wright
A. H. Clauer
D. K. Shetty
T. R. Tucker
J. T. Stropki

November 18, 1982

Work Performed Under Contract No. W-7405-ENG-26

Battelle Columbus Laboratories
Columbus, Ohio

U. S. DEPARTMENT OF ENERGY

DISCLAIMER

DISCLAIMER

This report has been reproduced directly from the best available copy.

Available from the National Technical Information Service, U. S. Department of Commerce, Springfield, Virginia 22161.

Price: Printed Copy A08
Microfiche A01

Codes are used for pricing all publications. The code is determined by the number of pages in the publication. Information pertaining to the pricing codes can be found in the current issues of the following publications, which are generally available in most libraries: *Energy Research Abstracts, (ERA); Government Reports Announcements* and Index (*GRA* and I); *Scientific and Technical Abstract Reports (STAR);* and publication, NTIS-PR-360 available from (NTIS) at the above address.

DOE/NBM-3007365
(DE83007365)
Distribution Category UC-90b

FINAL REPORT

on

EVALUATION OF ADVANCED MATERIALS

for

SLURRY EROSION SERVICE

Work sponsored by Department of Energy, Advanced
Research and Technology Development
Fossil Energy Materials Program

Contract No. 85X-69611C

I. G. Wright, A. H. Clauer, D. K. Shetty,
T. R. Tucker and J. T. Stropki

November 18, 1982

BATTELLE
Columbus Laboratories
505 King Avenue
Columbus, Ohio

TABLE OF CONTENTS

LIST OF TABLES

LIST OF FIGURES

LIST OF FIGURES
(CONTINUED)

LIST OF FIGURES
(CONTINUED)

LIST OF FIGURES
(CONTINUED)

LIST OF FIGURES
(CONTINUED)

EXECUTIVE SUMMARY

The aim of this program was to establish erosion data on a number of candidate valve materials under a range of slurry erosion conditions which would be useful to valve and process engineers involved in materials selection and valve design.

The program comprised three major tasks: **Evaluation of Advanced Materials** in a standardized slurry erosion test to provide a basis for comparison of the performance of advanced materials suitable for application in letdown and block valves. Materials available commercially as well as developmental materials and coatings were studied. **Characterization of Erosion Behavior** of different classes of materials to investigate the causes of differences in mode and rate of degradation between different forms of the same ceramic and between different materials. **Approaches to the Development of New Materials** through the use of advanced techniques such as hot isostatic processing, chemical vapor deposition, and laser surface melting to synthesize desired materials structures.

Of the many materials evaluated in a one-hour, coal-derived slurry test (8% solids in anthracene oil), run at 343 C, 100 m/sec with a nominal impact angle of 20^{o}, several exhibited erosion depths similar to that of a cemented tungsten carbide, Kennametal K 701 (WC + 10%Co + 4%Cr), used as a reference. A few showed potential for significantly decreased erosion. In particular, two CVD coatings (SiC and TiB_2),bulk α-SiC and a compacted synthetic diamond showed excellent potential. Cemented diamond- Si-SiC materials, which can be fabricated to larger and more complicated shapes than the diamond compact, also showed promise for achieving good erosion performance.

For cemented tungsten carbide materials, erosion rate decreased with decreasing binder content to a minimum value, corresponding to 5-6% binder, and then increased with further decrease in binder content. Measured hardness increased with decreasing binder content, while fracture toughness decreased. The trend in erosion resistance of this class of materials was characterized as a transition from a ductile erosion mechanism at high binder levels, to a brittle, intergranular mechanism at low binder levels. An observation of practical significance was that apparently small differences in composition

and structure, for instance between different batches of a given grade, were capable of producing a substantial change in erosion behavior.

In order to facilitate investigation of the mode of erosion of specific classes of materials, a substitute slurry composed of amorphous silica in a petroleum-derived oil was developed and characterized. Comparisons were made between the erosion rates obtained on a reference cemented tungsten carbide target by this slurry and by the coal-derived slurry, the aging characteristics of the two slurries were compared, and relative rankings of a series of different materials were obtained. The substitute slurry was more erosive, for a given solids content, than the coal-derived slurry by a factor of about 2 to 4, which was expected assuming the silica particles to be more efficient erodents than the coal-derived solids. The ranking of the target materials based on the erosion rates in the substitute slurry was nearly identical to the ranking obtained in the coal solids slurry tests, with the exception of sintered α-SiC, which showed extremely low wear rates in the coal slurry.

The features of eroded surfaces of ceramic materials eroded in these slurry tests suggested that three basic modes of material removal can occur: ductile cutting, elastic-plastic indentation and fracture, and intergranular fracture. Several single-phase ceramics, notably hot-pressed B_4C, CVD TiB_2, and CVD α-SiC, exhibited features associated with ductile cutting, while hot-pressed or sintered materials, such as SiC, Si_3N_4 and Al_2O_3, appeared to wear by an intergranular fracture mechanism. The classic elastic-plastic indentation and fracture, brittle failure mechanism was observed in sapphire and soda-lime glass. Although the rate of material removal by the brittle fracture mechanisms may be an order of magnitude greater than by the ductile cutting mechanism, the erosion behavior of some of the materials which exhibited the latter mode of erosion was additionally degraded by other effects. These took the form of residual porosity or second phases and impurities that enhanced the erosion rates of grain boundary regions. Processing approaches to minimize these defects were discussed.

One approach to the synthesis of desired microstructures has been to develop a procedure using laser radiation to fuse preplaced powder mixtures on to steels of normally poor erosion resistance. The powder mixtures investigated contained hard particles such as TiC or WC and metallic powders of

cobalt-base alloys, such that the resultant fused layer approximated a cermet structure. Volume fractions of carbides exceeding those in conventional hard-facing alloys were attained, but these were still lower than desired for effective slurry erosion resistance. The major factor currently limiting the incorporation of larger volume fractions of carbides in crack-free, adherent layers is insufficient understanding of the effects of heat-flux on the laser-powder-substrate interaction.

An investigation of factors controlling the development of a banded structure in the chemical vapor deposition of SiC showed that a system instability was the most likely cause. Systematic process changes provided some directions for minimizing undesirable microstructural features. In particular, the development of porous areas appeared to be associated with the incorporation of SiC dust into the deposit.

I. INTRODUCTION

While erosion of critical components of coal conversion processes continues to be an area of extreme concern, and in some cases a process-limiting factor, there have been demonstrations that solutions to this problem are possible if proper attention is given to materials selection and hydraulic design.[1,2] Recent experience at one coal liquefaction pilot plant has amply reinforced the importance of understanding and controlling the factors affecting erosion performance of erosion-resistant materials. In an application where good materials selection had resulted in acceptable and reproducible performance of a critical valve, so that it was no longer the major cause of plant shutdown, apparently small process changes together with a lack of vigilance on the materials supplied for valve trim led to a return to unpredictable lives for the valves.[2]

Work at Battelle-Columbus on earlier phases of this program[3,4] has been concerned with comparing the erosion behavior of numerous candidate materials, but has also attempted to establish system and materials factors affecting the erosion behavior of the more promising materials. The cemented tungsten carbide materials currently preferred for use as valve trim and wear surfaces were found to exhibit a combination of good resistance to erosion, especially at low angles of impingement, and a moderate degree of toughness, which allows some confidence that such trim can be used in an engineering application without extreme fear of breakage. Some ceramic materials, notably certain forms of silicon carbide and titanium carbide and diboride, have shown potential for achieving better erosion resistance than the cemented tungsten carbides, but without exception these ceramics have a reduced level of toughness that renders them prone to damage and, as yet, unsuitable for engineering applications.

This report discusses:

(a) The continuation of this screening work on a range of cermet, ceramic and coating materials, using a standardized testing procedure, based on a coal-derived slurry to provide a basis for comparison

(b) The development and characterization of an easily controlled, non-toxic, silica/oil-based slurry test, and its use in characterizing the erosion behavior of new materials

(c) Approaches to the development of new materials with desired morphologies and chemistries using techniques such as laser surface alloying and hot isostatic pressing.

II. EXPERIMENTAL PROCEDURES

II.1 Laboratory Erosion Rig

The laboratory erosion rig is essentially the same as that used in previous phases of the program, and is shown schematically in Figure 1(a). It comprises basically a reservoir of slurry, a pump for charging the reservoir, and an orifice through which the slurry is passed to form a controlled jet, which impinges directly on the test specimen. The rig can be operated in two main modes, recirculating or once-through. In the recirculating mode, Figure 1(a), slurry is driven from the reservoir by gas overpressure, through a heating coil and an in-line filter (to remove any large particles or agglomerates), and then through the orifice and over the specimen. The slurry jet velocity is controlled by the gas overpressure, and is monitored by a digital readout differential pressure transducer installed across the orifice. The slurry passing over the specimen is collected in the bottom of the test chamber, and any gas desorbed from the slurry is vented off. Slurry is pumped from the test chamber, cooled in heat exchangers, and returned to the reservoir at a rate determined by a level controller adjacent to the test chamber. The techniques of working with continuously recycled slurry, and of rejuvenation procedures devised to maintain a practically constant slurry erosivity, have been discussed at length elsewhere.(3)

The once-through mode, shown in Figure 1(b), is intended to provide a test condition which minimizes uncertainties which may arise from changes in the character of the erodent after impact with the specimen target. In this

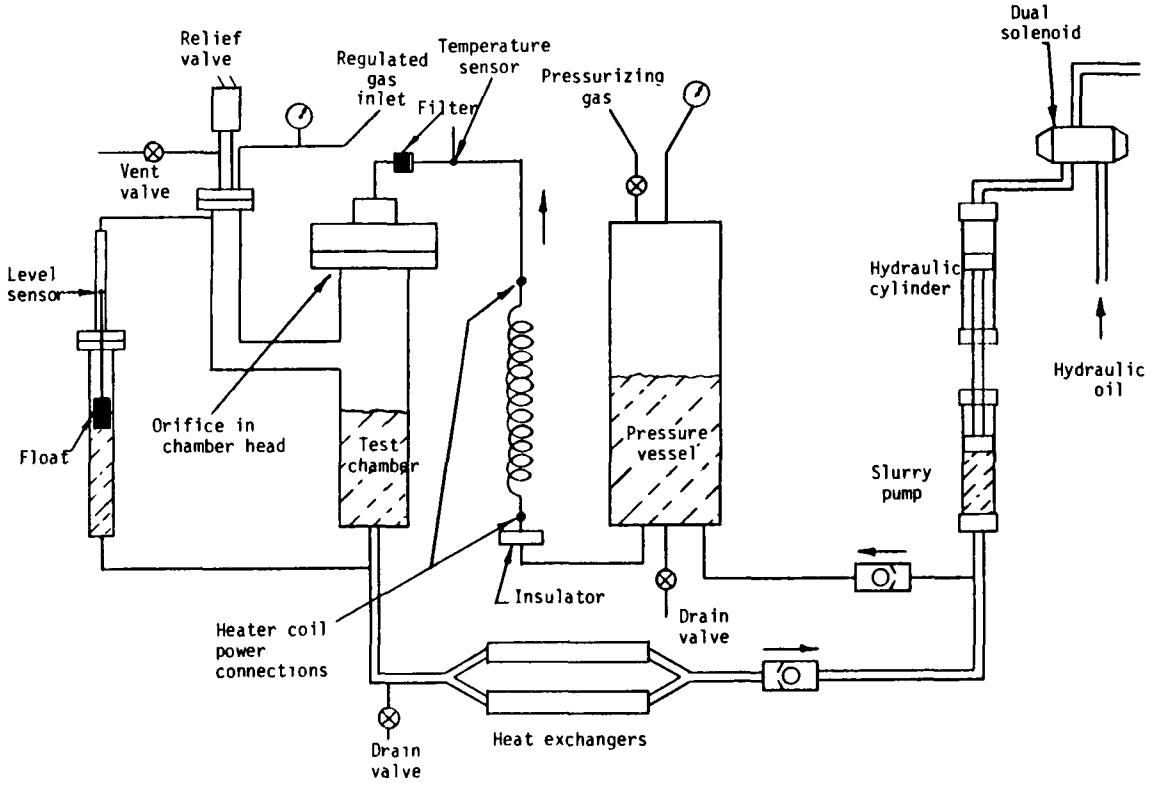

FIGURE 1(a). SCHEMATIC DIAGRAM OF SLURRY EROSION RIG, CONFIGURED FOR RECYCLING MODE OF OPERATION

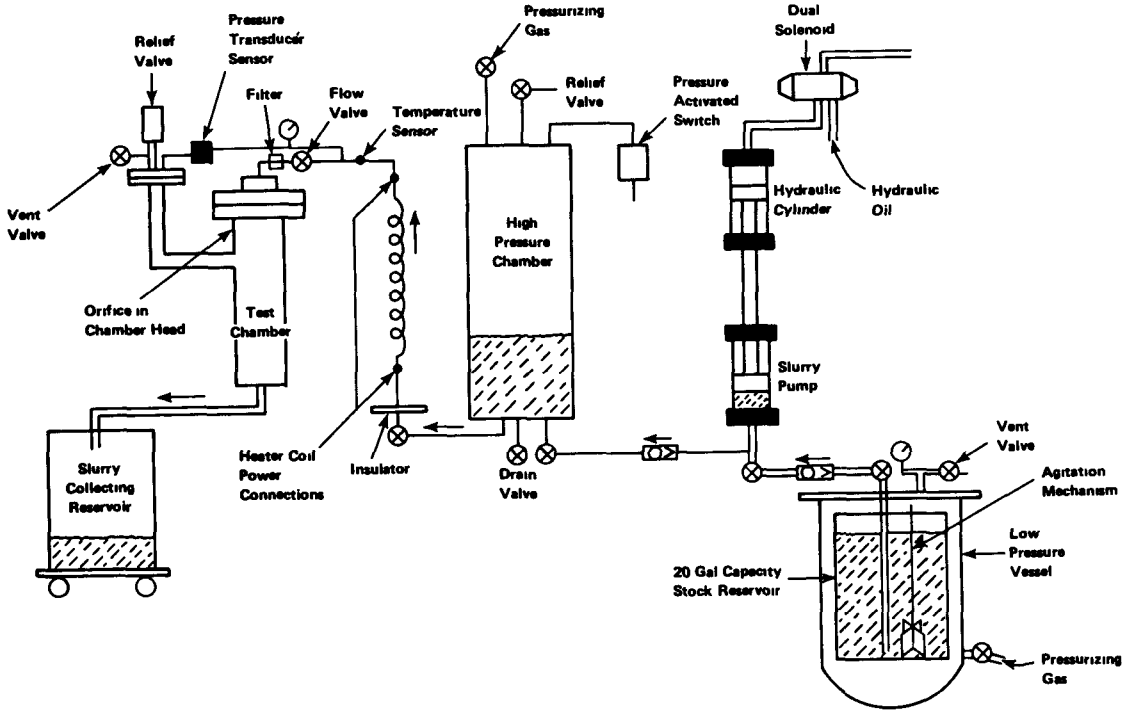

FIGURE 1(b). SLURRY EROSION RIG CONFIGURED FOR ONCE-THROUGH MODE OF OPERATION

case, a supply of slurry is fed directly to the pump inlet, and used slurry is bled from the coolers following the test chamber, into a pressurized receiving tank; no recirculation of slurry occurs, and the erodent passes over the specimen once. This mode has the disadvantages that a much larger volume of slurry is required, with the consequent increase in cost and handling, especially if the slurry constituents are expensive and involve difficult or hazardous disposal procedures. Its major advantage is in providing a better controlled test by allowing an accurate history of the erodent to be compiled.

Since the slurry jet diameter is quite small (0.5 mm), the area of specimen required for testing is correspondingly small, so that specimens can be made from almost any shape or size of original stock. Fixturing for different shapes of specimens is easily accomplished, and adapters are available for holding specimens at various angles with respect to the slurry jet. Figure 2 is a schematic diagram showing the relative positioning of the slurry jet and the specimen.

II.2 Erosive Slurries

The erosive slurry used in the standardized comparison tests was intended to simulate as well as possible that in the SRC-1 pilot plant, and consisted of 25 weight percent of unfiltered SRC product dissolved in anthracene oil. The SRC product was derived from Monterey, Illinois, No. 6 coal. The insoluble solids content of the processed coal was 34 percent by weight, which resulted in approximately 8 percent solids in the slurry. The average particle size of the solids was 23 μm. Approximately 4 percent was below 1.5 μm. In order to provide some further simulation of the actual pilot plant environment, the slurry was heated to 343 C (650 F) before being let down at the orifice from a pressure of 13.8 MPa (2000 psi). The ambient pressure in the specimen chamber was nominally 0.69 MPa (100 psi). The slurry was pressurized by a head of gas in the reservoir, consisting of approximately 80 percent hydrogen and 20 percent argon. Solution of hydrogen into the slurry and its release during letdown is apparently a major feature of the actual

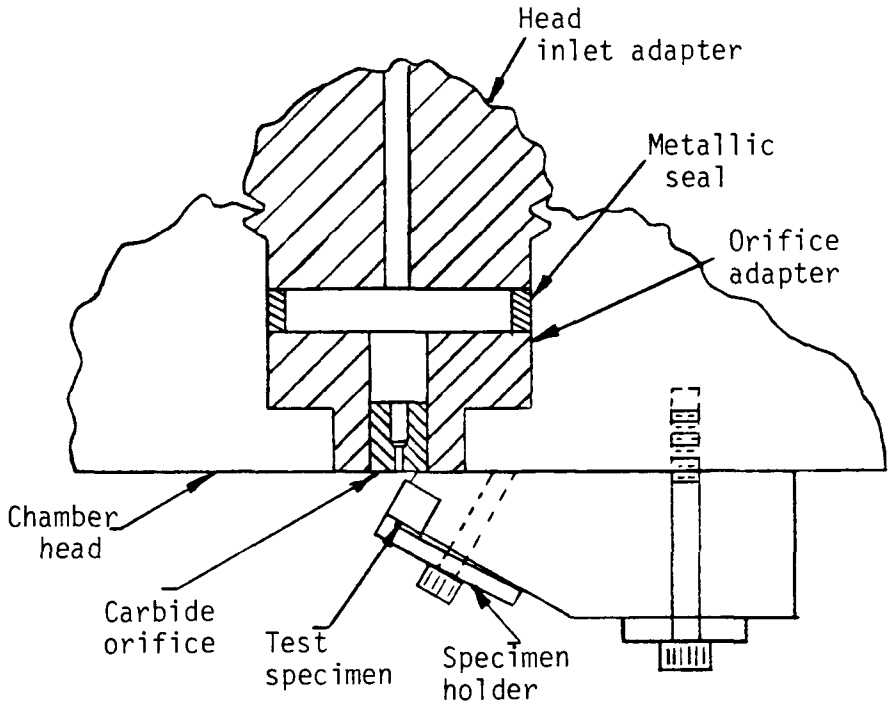

FIGURE 2. SCHEMATIC DIAGRAM OF THE SPECIMEN FIXTURING IN THE SLURRY EROSION RIG.

process, but is not well simulated in the laboratory because of the short contact time between heated slurry and the driving gas.

In all the standardized comparison testing, the specimen test surface was oriented at an angle of 20 degrees to the impinging jet of slurry. This angle was shown in the early phases of the work to produce the type of wear experienced in letdown service. The distance traversed by the slurry to the point of contact with the test surface was 2.8 mm. The tests were each run for a duration of one hour, where the specimen behavior permitted.

Previous results[3] revealed a wide diversity of undissolved solids derived from the liquefaction plant products, which prevents any reasonable estimate of the number of impacts in a given time, and suggests that the erosive efficiency will vary greatly among these solids. Hence as an aid to enabling a more mechanistic approach to be used, as well as a way to avoid the health risks and handling problems associated with coal-derived material, a silica-hydraulic oil slurry was developed. This activity is described in Section III.2.2.

III. RESULTS AND DISCUSSION

III.1 Materials Screening Activities

The testing procedure used in these activities was the standardized, coal-derived slurry test described in Section II.2. In some instances where metallic materials were compared, the slurry velocity was reduced to 56 m/sec, which was determined in previous studies[3] to provide a severe test condition for these types of materials, while allowing test durations sufficient to provide for good control.

III.1.1 Laboratory Support for Advanced Materials Development

Extensive comparative erosion testing was performed on several generic classes of materials. These consisted of:

(a) Tungsten-carbide-based cermets, with variations in carbide size, additions of other carbides, and variations in binder level and chemistry
(b) Novel cermet materials
(c) Ceramic materials
(d) Coatings.

Because of the large number of samples involved, characterization of the erosion behavior of the majority of these materials was by surface profilometry only. In instances where the results were very different from those of materials of the same class, or where the type of erosion behavior to be expected was not known, additional characterization involving scanning-electron microscopy and/or metallography was undertaken.

III.1.1.A. Tungsten Carbide-Based Cermets. The results for a range of tungsten carbide-based cermets are listed in Table 1, along with the values for a sample of Kennametal K 701 (used as an internal standard) which was run at intervals in the test. A wide range of known binder contents from nominally zero (Kennametal WCX and SP 278 grades) to 14 percent (K 714) was covered by the materials studied. Binder compositions were Co, Ni, Co-Cr, Ni-Mo, Ni-Cu-Fe, Ti-C-N, plus others which were not disclosed. Variations were also present in the grain size and size distribution of the carbide phase, and in the proportions of carbides other than WC that were present. The overall trend of the erosion results was that the materials with equal or better performance than K 701 were either those with a Co-Cr binder (K 703, K 714), or those with a low level of Co-binder (SPZ 313, K 68, K 11, WA-4, with binder levels of up to 5.8 percent). Microstructural factors such as grain size and size distribution are variables whose influences could not be individually assessed at this stage. The Co-Cr-bound K 703 and K 714 have higher relative impact resistance than K 701 (12 and 21, respectively, compared to 7; manufacturer's data), while the hardnesses (Rockwell A) are 92.0 for K 701; 91.5 for K 703, and 92.5 for K 714. Manufacturer's data for the Co-bound materials K 11 and K 68 indicate relative impact resistance values of 14 and 52, respectively, and Rockwell A hardnesses of 93.0 and 92.6, respectively. Interestingly, the abrasion resistances (1/volume loss, measured in a standard test) of the cobalt-bound K 11 and K 68 are lower than for the K 701 and K 703

TABLE 1. EROSION DATA FOR NEW AND MODIFIED WC-BASED CERMETS IN STANDARD COMPARISON TEST

Material	Designation	Source	Composition	K 701[a] Ref.	Erosion Crater	
					Depth (μm)	Length (μm)
WC (binderless)	WCX	Kennametal	tungsten monocarbide	A	15.2	2.08×10^3
WC (binderless)	SP 278	Kennametal	--	B	8.5	3.00×10^3
WC-TaC-Co	K 602	Kennametal	1.5% Co	B	3.3	3.34×10^3
WC-Co	K 6T	Kennametal	low Co	A	2.7	0.747×10^3
WC-Co	SPZ 313	Kennametal	low Co, micrograin WC	B	1.5/None	0.70×10^3
WC-Co	K 11	Kennametal	2.8% Co	B	2.5	2.51×10^3
WC-Co	K 68	Kennametal	5.8% Co	B	2.0	3.23×10^3
WC-Co	K 3406	Kennametal	7.8 % Co	B	3.3	0.84×10^3
WC-Co	K 3560	Kennametal	9.5% Co	A	2.5	---
WC-Co	K 3109	Kennametal	12.2% Co	B	4.3	1.84×10^3
WC-Co-multicarbides	CRZ 316-25	Kennametal	--	A	4.3	1.52×10^3
WC-Ni-multicarbides	SP 269	Kennametal	--	A	14.8	1.117×10^3
WC-Ni	K 801	Kennametal	6% Ni	B	11.4	2.59×10^3
WC-Ni	K 803	Kennametal	--	B	7.1	3.35×10^3
WC-Ni-Mo	K 165	Kennametal	contains TiC	B	53.3	2.44×10^3
WC-Ni-Cu-Fe	W 2	Kennametal	94% W, 2.6% (Ni, Cu, Fe)	B	too deep to measure	
WC-Ni-Cu-Fe	W 11	Kennametal	--	B	too deep to measure	
WC-Co-Cr	K 701	Kennametal	8.5% Co, 4.5% Cr	B	1.8-3.0	$2.24\text{-}3.56 \times 10^3$
WC-Co-Cr	K 703	Kennametal	6.0% Co, 1.0% Cr	B	1.2	2.08×10^3
WC-Co-Cr	K 714	Kennametal	14% Co+Cr	B	2.0	2.84×10^3
WC-TiCN	SP 293A	Kennametal	high Ti, fine grained	A	10.4	1.477×10^3

TABLE 1. (Continued)

Material	Designation	Source	Composition	K 701[a] Ref.	Erosion Crater Depth (μm)	Erosion Crater Length (μm)
WC-TiCN	SP 293B	Kennametal	HIP-version of SP293A	A	10.8	1.57×10^3
WC-proprietary binder	SP 317	Kennametal	--	A	6.8	0.508×10^3
WC-Co	WA-41	GTE	WC-9.0% Co	C	9.6	2.72×10^3
WC-Co	WA-1	GTE	WC-6.0% Co	C	7.8	2.44×10^3
WC-Co	WA-2	GTE	WC-6.0% Co	C	6.7	2.29×10^3
WC-Co	WA-35	GTE	WC-6.0% Co	C	5.6	2.34×10^3
WC-Co	X-614	GTE	6% Co, total composition unknown	C	6.6	2.84×10^3
WC-Co	WA-3	GTE	WC-4.3% Co	C	6.6	2.59×10^3
WC-Co	WA-4	GTE	WC-3.0% Co	C	4.7	3.00×10^3
WC-Co	WA-107	GTE	composition unknown	C	5.1	2.49×10^3
WC-Co	WA-110	GTE	submicron carbide, composition unknown	C	6.6	3.00×10^3
WC-Co	WA-114	GTE	composition unknown	C	12.7	2.49×10^3
WC-Co	WA-119	GTE	composition unknown	C	15.2	2.39×10^3
WC-Co	WA-510	GTE	non-magnetic carbide, composition unknown	C	86.4	2.64×10^3

[a]: Erosion crater dimensions for reference K 701 material in the same test:

A: depth = 1.2 - 1.5 μm, length = 0.79 - 0.91 x 10^3 μm.

B: depth = 1.9 - 3.5 μm, length = 1.07 - 3.43 x 10^3 μm.

C: depth = 3.4 - 5.6 μm, length = 2.31 - 3.15 x 10^3 μm.

Co-Cr grades (300 compared to 825 and 760) but similar to that for K 714 (380).

More systematic studies of the influence of the hardness and fracture toughess of these cermets were carried out on samples chosen from those listed in Table 1, and are reported in Section III.2.1.

III.1.1.B Novel Cermets. Five main classes of novel cermet materials were evaluated in the standard slurry erosion test. These consisted of synthetic diamonds in a silicon-silicon carbide matrix; titanium diboride - Ni, with controlled oxygen contents; chromium-based cermets; chromium boride-based cermets; and boron carbide-based cermets. The erosion crater dimensions are listed in Table 2 and show that three groups showed potential to erode at a similar rate or slower than the standard K 701 cermets. These were diamond-Si-SiC compacts with a high volume fraction of fine diamonds, the B_4C-Ni or -Co cermets, and the GTE composites.

The performance of the diamond-Si-SiC compacts with a high volume fraction of fine diamond particles was difficult to assess, because of the initial surface roughness of these materials, which were difficult to polish to the usual surface finish. In addition, the erosion test did not produce any distinct crater. The diamond particles were not obviously eroded, but the Si-SiC matrix suffered some attack especially at the matrix-particle interfaces immediately in the jet impact area. No measurable erosion was detected on the Stratapax 2538, which is apparently a binderless sintered diamond product, although the area which had been beneath the jet could be distinguished by eye under oblique lighting.

The features of the eroded surfaces of some of the diamond compacts are shown in Figures 3-5. The sample (B) with a high volume fraction of the coarsest diamond particles studied lost large amounts of matrix material such that some of the diamonds were partially exposed and undercut, Figure 3a. No diamonds were actually liberated from the surface, however. Some evidence of damage is evident on individual diamond particles; it seems probable that this may have resulted from preexisting faults in these particles. Figure 3b shows an area of untested surface of this material in which some such faults, or

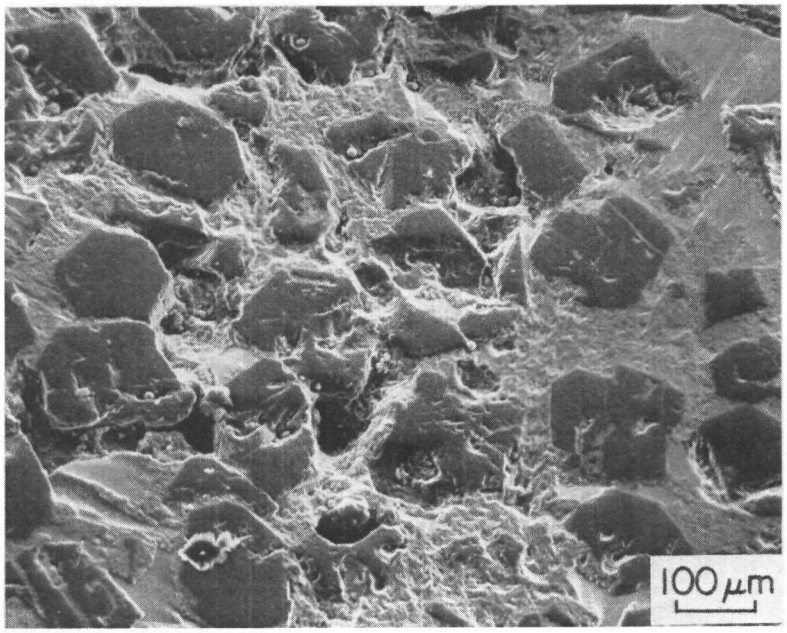

(a)

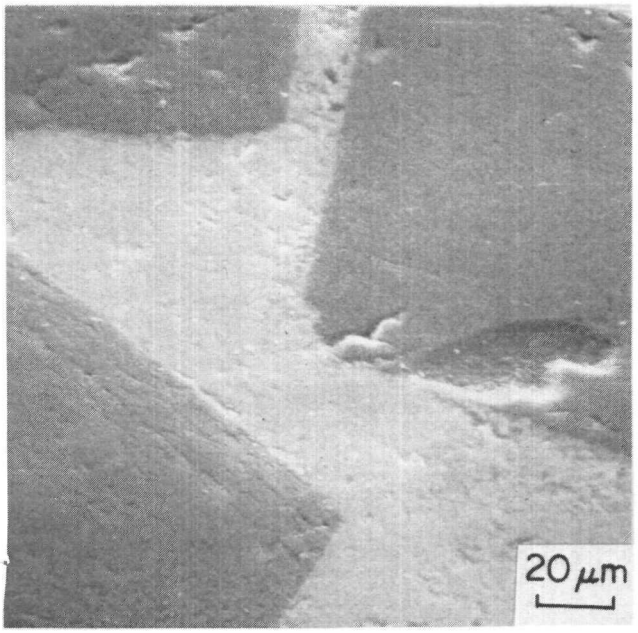

(b)

FIGURE 3. SURFACE OF DIAMOND - Si-SiC [HIGH DIAMOND SIZE 1(B)] SHOWING

(a) Undercutting of Diamonds in Erosion Crater
(b) Good Diamond-to-Matrix Bonding in Uneroded Area

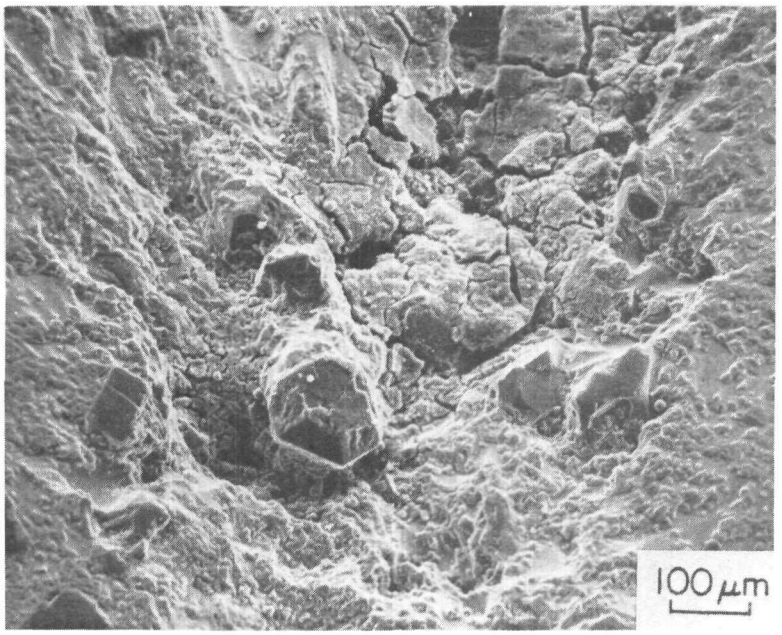

(a)

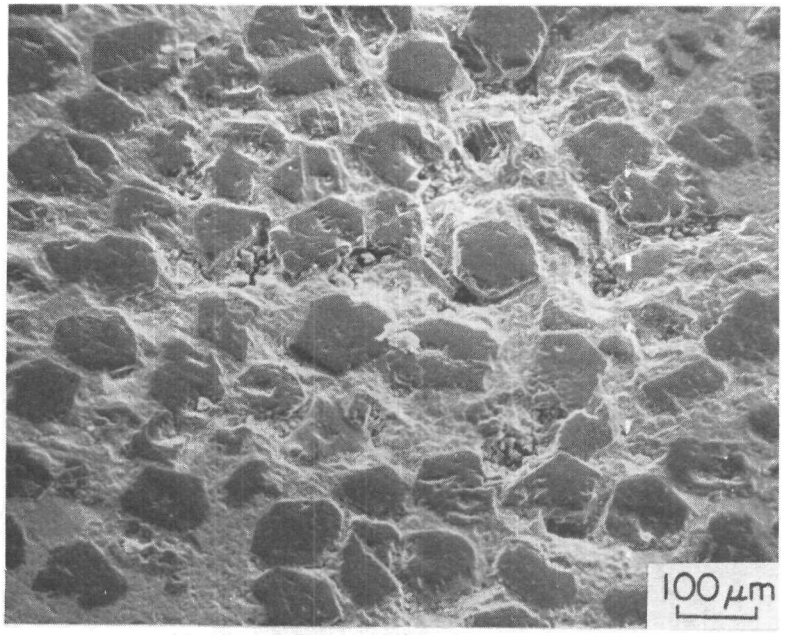

(b)

FIGURE 4. ERODED SURFACE OF DIAMOND - Si-SiC

(a) Low Diamond, Size 2 (C)

(b) High Diamond, Size 2 (D)

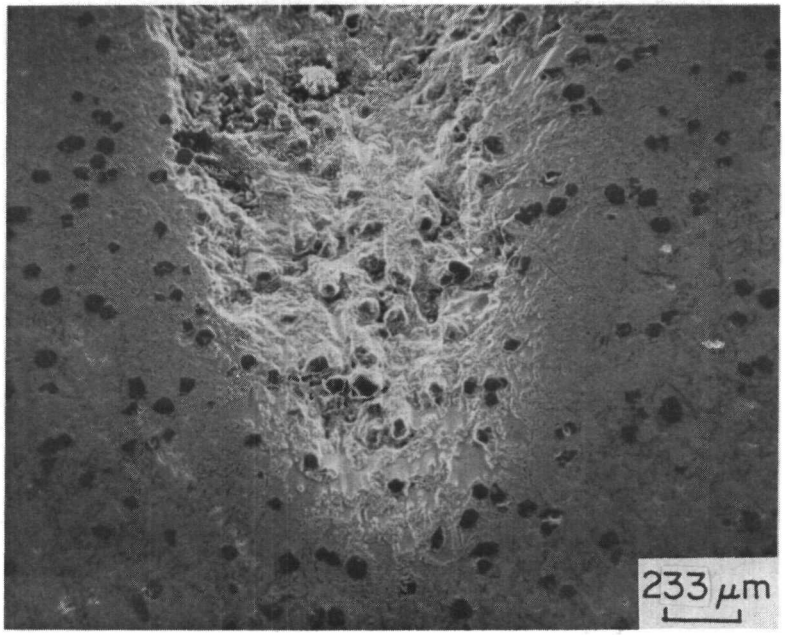

(a)

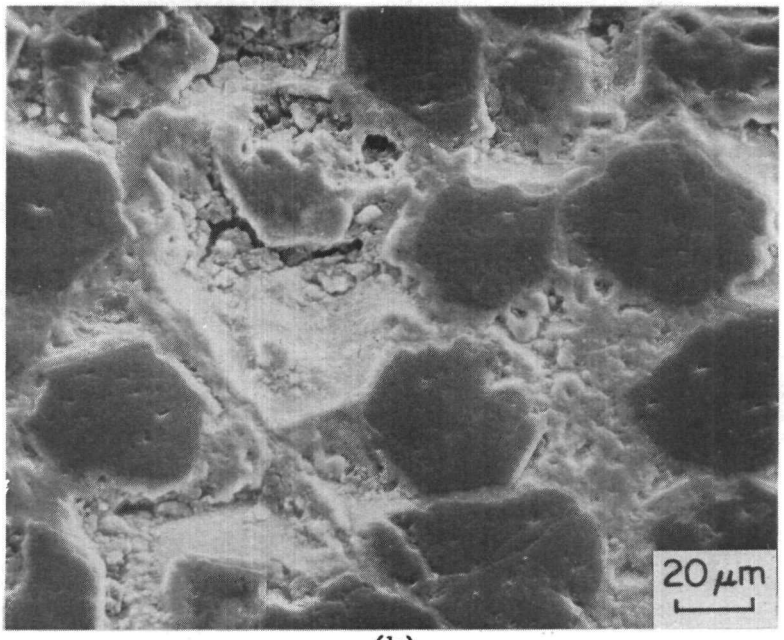

(b)

FIGURE 5. ERODED SURFACES OF DIAMOND - Si-SiC

(a) Low Diamond, Size 3 (E)

(b) High Diamond, Size 3 (F)

TABLE 2. EROSION DATA FOR NOVEL CERMET MATERIALS IN STANDARD COMPARISON TEST

Material	Designation	Source	Composition	K 701[a] Ref.	Erosion Crater	
					Depth (μm)	Length (μm)
Diamond	Stratapax/2538	GE	diamond compact	A	none*	
Diamond/Si-SiC	A	GE	low diamond, size 1*	A	135	2.95×10^3
Diamond/Si-SiC	B	GE	high diamond, size 1	A	∿22.9	--
Diamond/Si-SiC	C	GE	low diamond, size 2	A	135	2.57×10^3
Diamond/Si-SiC	D	GE	high diamond, size 2	A	25-27	∿150
Diamond/Si-SiC	E	GE	low diamond, size 3	A	187	2.94×10^3
Diamond/Si-SiC	F	GE	high diamond, size 3	A	7.7-10.2	--
Diamond/Si-SiC	CDC/3-G	GE	high diamond, size 6	A	∿4.8	--
Diamond/Si-SiC	CDC/4-H	GE	high diamond, size 5	A	∿6.9	--
Diamond/Si-SiC	CDC/5-I	GE	high diamond, size 4	A	∿4.6	--
Diamond/Si-SiC	CDC/J	GE	high diamond, size 3	A	∿7.9	--
TiB_2-Ni	NT 85 Q	ORNL	Bal TiB_2, 0.4% Ni, 1% O_2	A	17.0	--
TiB_2-Ni	NT 85 R	ORNL	Bal TiB_2, 0.4% Ni, 1% O_2	A	19.1	--
TiB_2-Ni	NT 85 S	ORNL	Bal TiB_2, 1.5% Ni, 2.2% O_2	A	22.5	--
TiB_2-Ni	NT 85 T	ORNL	Bal TiB_2, 1.0% Ni, 2.0% O_2	A	14.9	--
TiB_2-Ni	NM T-85	ORNL	Bal TiB_2, 8.6% (Ni-90%, Mo-10%)	A	16.8	--
Cr-cermets	C-HM-9	ORNL	56.7% wt. Al_2O_3, 38.8% wt. B_4C, 4.5% wt. Cr	A	19.1	2.93×10^3
Cr-cermets	C-HM-10	ORNL	38.9% wt. Al_2O_3, 56.6% wt. CrB, 4.5% wt. Cr	A	30.0	3.00×10^3
Cr-cermets	C-HM-12	ORNL	47.3% wt. Al_2O_3, 48.2% wt. B_4C, 4.5% wt. Cr	A	9.7	2.59×10^3

TABLE 2. (Continued)

Material	Designation	Source	Composition	K 701[a] Ref.	Erosion Crater Depth (μm)	Erosion Crater Length (μm)
CrB-cermets	HM-7	ORNL	50.5% wt. CrB, 49.5% at Colmonoy No. 6	A	35.1	2.27×10^3
CrB-cermets	100/CBC	ORNL	CrB-2% wt. Co	A	excessive erosion in 1 hr.	
CrB-cermets	101/CBF	ORNL	CrB-2% wt. Fe	A	excessive erosion in 35 min.	
B_4C-Ni	256	ORNL	98% B_4C, 2% Ni	B	specimen broken during test assembly	
B_4C-Ni	260	ORNL	94% B_4C, 6% Ni	B	7.1	1.15×10^3
B_4C-Co	257	ORNL	98% B_4C, 2% Co	B	6.6	0.90×10^3
B_4C-Co	259	ORNL	96% B_4C, 4% Co	B	6.0	1.32×10^3
B_4C-Co	263	ORNL	92% B_4C, 8% Co	B	1.9	0.76×10^3
B_4C-SiB_4	320	ORNL	0.9/0.1 molar B_4C/SiB_4	B	too deep to measure	
B_4C-SiB_4-Co	342	ORNL	4% Co+B_4C/SiB_4, 0.9/0.1	B	111.7	1.19×10^3
B_4C-SiB_4-Ni	343	ORNL	6% Ni+B_4C/SiB_4, 0.9/0.1	B	68.6	1.34×10^3
B_4C-SiB_4-Ni	347	ORNL	10% Ni+B_4C/SiB_4, 0.9/0.1	B	25.0	0.98×10^3
Composite	SNT	GTE	--	C	5.4	0.96×10^3
Composite	X622	GTE	--	C	6.5	0.82×10^3

* Diamond size designations are 1 = coarse, 6 = fine.

a: Erosion crater dimensions for reference K 701 material in the same test:

A: depth = 3.4 - 5.6 μm, length = 2.31 - 3.15 x 10^3 μm.

B: depth = 1.9 - 3.5 μm, length = 1.07 - 3.43 x 10^3 μm.

C: depth = 3.1 - 4.7 μm, length = 1.04 - 1.73 x 10^3 μm.

possibly damage incurred in the surface polishing operations, are observed. Note the very clean particle-matrix interfaces.

Figures 4 and 5 show the difference in behavior of samples having a low volume fraction (4a, 5a) and a high volume fraction (4b, 5b) of the same size of diamond particle; Figure 4 shows samples C and D with relatively coarse particles, while Figure 5 shows samples E and F with relatively fine particles. For samples with a low volume fraction of particles, sufficient loss of matrix material occurred in the erosion craters that individual diamond particles were completely undermined and eventually liberated from the surface. In these cases the erosion behavior was obviously a reflection of that of the Si-SiC matrix, rather than the diamond particles. With the high particle volume fraction materials, much less erosion of the matrix was evident, although undercutting of the leading edges of some diamond particles can be seen. In Figure 5b, a diamond particle has apparently been lost from the area of slurry jet impact. Overall, however, it appears that with the high volume fraction of diamond particles much of the Si-SiC matrix was shielded from the slurry jet at the 20-degree impact angle used, so that the erosion behavior of these materials was less dominated by the intrinsic erosion resistance of the matrix phase.

The characteristics of the eroded surfaces of the Cr-bound cermets are shown in Figures 6-8. The secondary electron images of the Al_2O_3-B_4C-Cr cermets in Figures 6 and 7 show a degree of back scatter, which allows differentiation of the phases by atomic number contrast. Hence the B_4C particles appear dark, and the Al_2O_3 particles, and any free chromium, appear bright, but are less discernible. The sharp, angular shapes of the B_4C particles appear to be slightly smoothed in the eroded areas. Although both exhibited quite smooth erosion craters, the leading edges of the B_4C particles in the 57-39 weight percent Al_2O_3-B_4C material (51 volume percent B_4C) were more prominently exposed than in the 47-48 (60 volume percent B_4C) material. Occasional particles had been lost from the erosion craters of each material.

Figure 7B suggests that preferential removal of the Al_2O_3 (darker) phase is the main mode of erosion of the CrB-Al_2O_3-Cr cermet, number C-HM-10. The eroded surface of the CrB-Colmonoy alloy cermet in Figure 8 shows that the

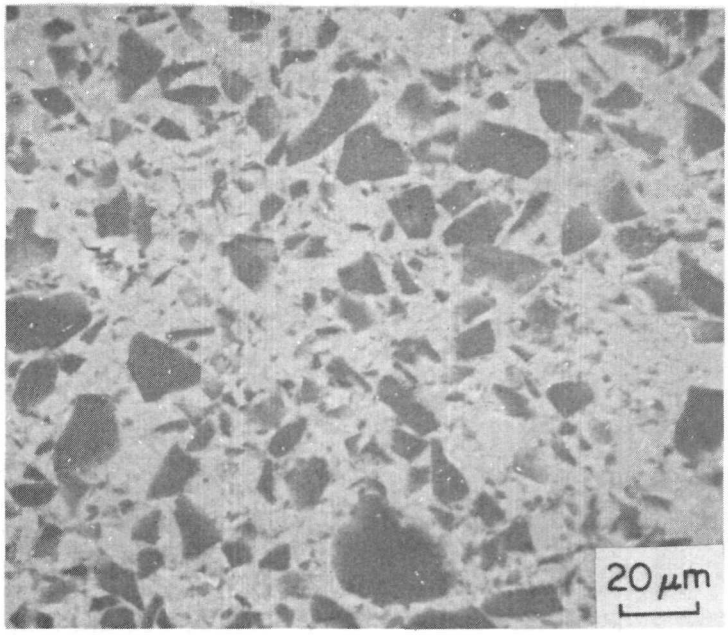

(a)

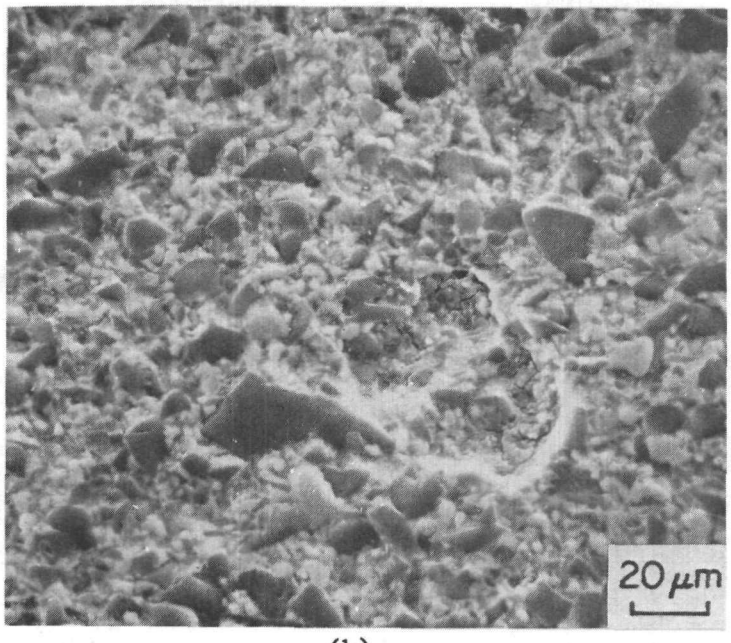

(b)

FIGURE 6. $A\ell_2O_3$ - B_4C - Cr CERMET, CHM - 9

(a) As Polished

(b) After Erosion

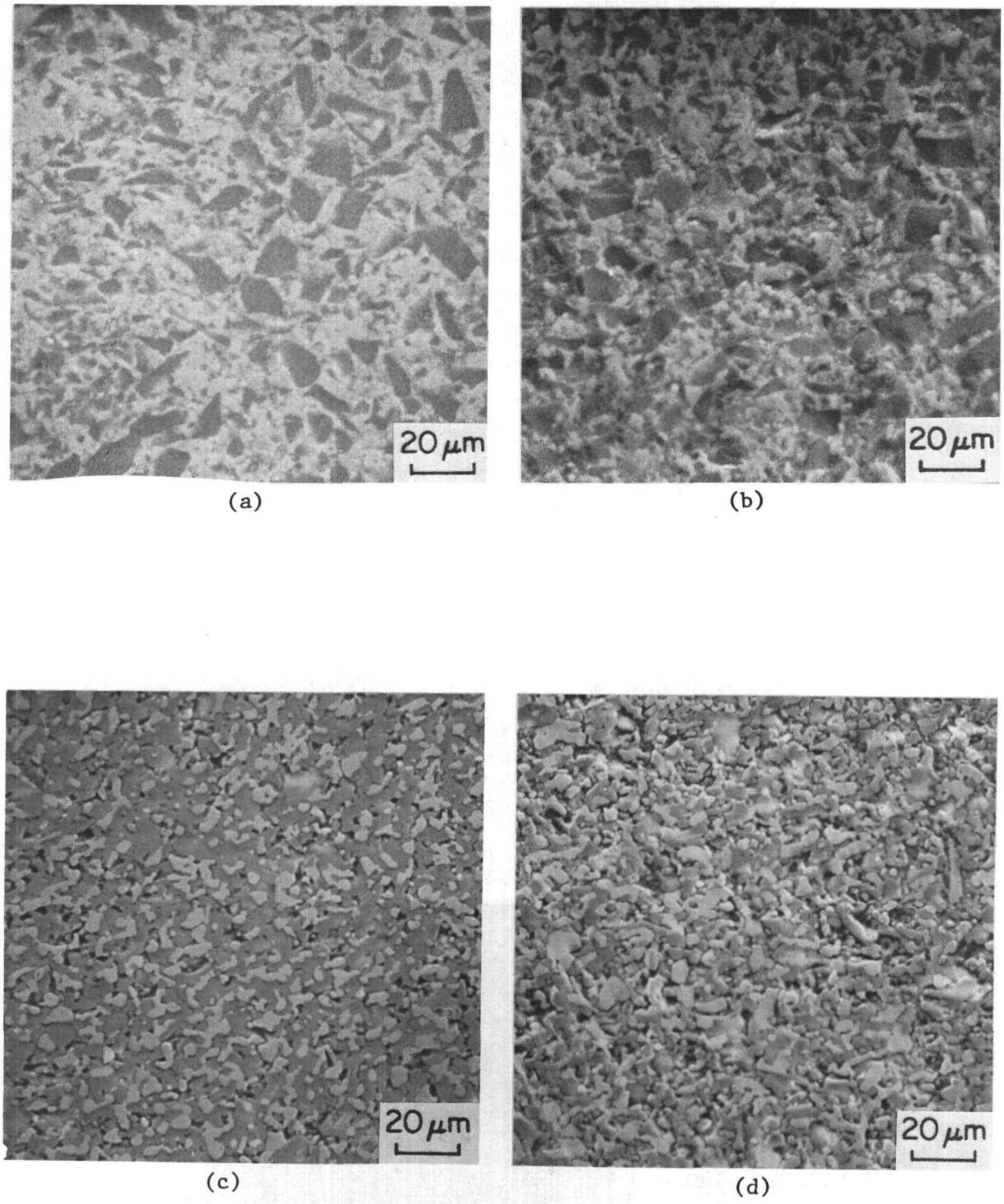

FIGURE 7. SURFACE FEATURES OF NOVEL CERMETS

(a) Al_2O_3 - B_4C - Cr (CHM - 12) As Polished, (b) After Erosion

(c) Al_2O_3 - CrB - Cr (CHM - 10) As Polished, (d) After Erosion

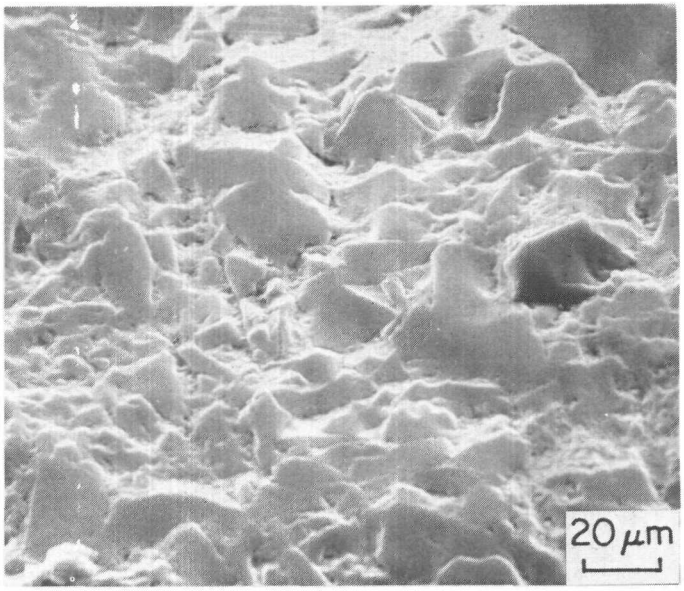

(a)

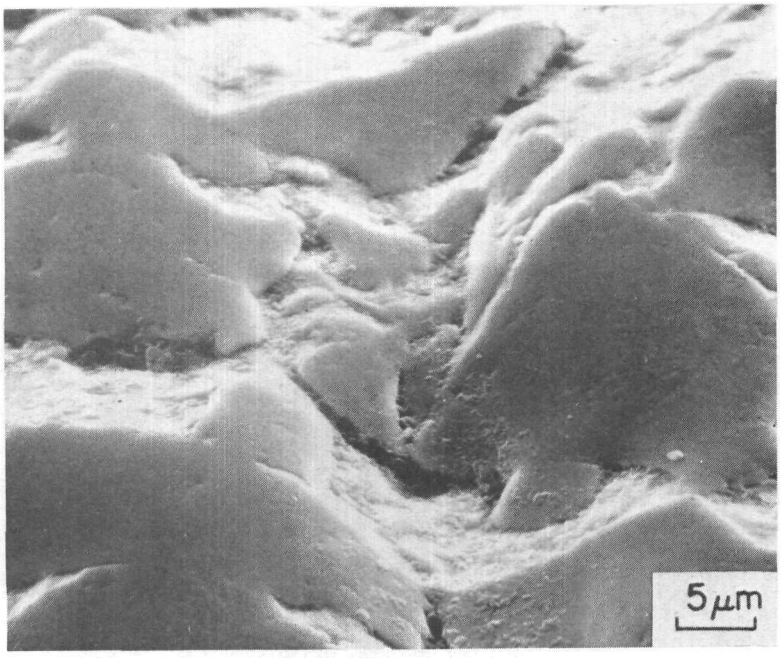

(b)

FIGURE 8. ERODED SURFACE OF CrB - COLMONOY NO. 6 CERMET, SHOWING PREFERENTIAL LOSS OF BINDER, AND ROUNDING OF CrB

binder phase has been removed, leaving the CrB grains exposed. Detailed examination of these CrB grains shows them to have eroded to rounded shapes by what appears to be a ductile mechanism similar to that observed for B_4C, for example. A few small areas were also observed where brittle chipping had caused removal of material, but the contribution of this mechanism appeared to be minor. The performance of this material in the standard erosion test is considered to be good.

The series of Co-bound B_4C-base cermets exhibited erosion values of a low order, with one composition performing almost as well as the best of the WC-cermets. The trend with these materials was to increased erosion resistance with increased binder content over the range 2 to 8 percent Co. The erosion observed on a single Ni-bound composition of this series was of a similar but slightly greater degree than that of the equivalent Co-bound specimen. A similar trend with binder content was found with B_4C-SiB_4 (0.9 to 0.1 molar ratio) material. With no binder, the erosion crater was too deep to traverse with the Talysurf profilometer, while additions to 10 percent Ni (or Co) reduced the depth of erosion substantially, though not to the low levels of the B_4C-Co cermets.

A similar trend to increased erosion resistance with increased binder content was found for a series of chromium boride cermets, tested under less severely erosive conditions. The results are listed in Table 3. The trend for all three binder types was the same. For these materials and the B_4C-Co cermets, this behavior appears to be directly related to the ability of the binder to effectively wet the cemented phase, and to fill the interstices between adjacent grains. At low binder levels, significant areas of porosity remained which provided a focus for erosive attack. With increasing levels of binder, these pores or unfilled interstices were substantially filled and provided more resistance to erosion; in fact, at the higher binder levels, these materials eroded in a manner similar to the established WC-Co cermets.

The results for modified Nitinol materials in the standard comparison test are shown in Table 4. These materials showed considerably more resistance to erosion in this test than did other metallics examined in previous programs (for instance, Type 304 stainless steel was severely eroded

TABLE 3. EROSION DATA IN COAL-DERIVED SLURRY AT REDUCED VELOCITY OF 56 m/sec

(Other conditions same as standard comparison test)

Material	Reference	Source	Composition	Erosion Crater	
				Depth, μm	Length, μm
CrB-Cermets	100/CBC	ORNL	CrB - 2% wt. Co	23.0	0.50×10^3
CrB-Cermets	109/CBC	ORNL	CrB - 12% wt. Co	0.5	1.30×10^3
CrB-Cermets	112/CBC	ORNL	CrB - 16% wt. Co	1.5	1.93×10^3
CrB-Cermets	115/CBC	ORNL	CrB - 20% wt. Co	2.5	0.97×10^3
CrB-Cermets	101/CBF	ORNL	CrB - 2% wt. Fe	340.0	--
CrB-Cermets	110/CBF	ORNL	CrB - 12% wt. Fe	13.7	1.14×10^3
CrB-Cermets	116/CBF	ORNL	CrB - 20% wt. Fe	1.2	1.23×10^3
CrB-Cermets	102/CBN	ORNL	CrB - 2% wt. Ni	204.0	1.02×10^3
CrB-Cermets	111/CBN	ORNL	CrB - 12% wt. Ni	1.8	1.33×10^3
CrB-Cermets	114/CBN	ORNL	CrB - 16% wt. Ni	1.5	1.17×10^3

TABLE 4. EROSION DATA FOR MODIFIED NITINOL IN STANDARD COMPARISON TEST

Material	Specimen Designation	Source	Composition	Erosion Crater	
				Depth (μm)	Length (μm)
Nitinol + B*	H-1	ORNL	53.1% wt. Ni 45.7% wt. Ti 1.1% wt. B	163	1.12×10^3
Nitinol + B*	H-2	ORNL	49.1% wt. Ni 47.5% wt. Ti 3.4% wt. B	130	1.36×10^3
Nitinol + B*	H-3	ORNL	46.55% wt. Ni 48.45% wt. Ti 5.0% wt. B	--	--
K 701	Reference			3.8	2.8×10^3

* Alloy of 50-50 atomic percent Ni-Ti, + TiB_2.

in 5 min). However, the standard test conditions are exceptionally severe and probably do not provide a fair test of the concepts investigated by these Nitinol materials.

III.1.1.C Ceramic Materials. Four ceramics were subjected to the standard comparison test, and duplicate tests of three were run because of concern over the possible effect of surface finish. As can be seen from Table 5, the differences between as received and ground finishes of the specimens tested in duplicate were small. Hot-pressed alumina materials have not performed well in this test in the past; the erosion behavior of K 060 and K 090 rank among the best observed for this class of ceramics. The performance of the SiAlON material, however, was excellent and similar to that of the best WC- and B_4C-cermets.

III.1.1.D Coatings. A large number of coatings from five different sources was evaluated in the standard comparison test, and the results are listed in Table 6. A surprising feature of these data is the general similarity in erosion performance of different coating types. Only two coating systems: CVD TiB_2 on cemented TiB_2-Ni; and CVD SiC on graphite, showed potential for significantly outperforming the reference K 701.

The former coatings were returned to Oak Ridge National Laboratory after exposure in the erosion rig, and the evaluation of these coatings has been reported elsewhere.(5)

The features of the eroded surfaces of the CVD TiB_2 coatings on Kennametal K 151A (essentially TiC-Ni) are shown in Figures 9 and 10. The 35 μm thick coating shown in Figure 9 and the 50 μm thick coating in Figure 10 exhibited very similar features; the eroded surfaces were very smooth on a micro scale, with some evidence of material removal by gouging.

The results for the Turbine Metals Technology coatings in this test were disappointing since field experience with similar coatings has been excellent. The erosion craters on both samples of TMT-745A were very similar in appearance, Figures 11, 12, even though the slurry flow direction in one case was parallel to the surface finish grinding direction, Figure 11, and in

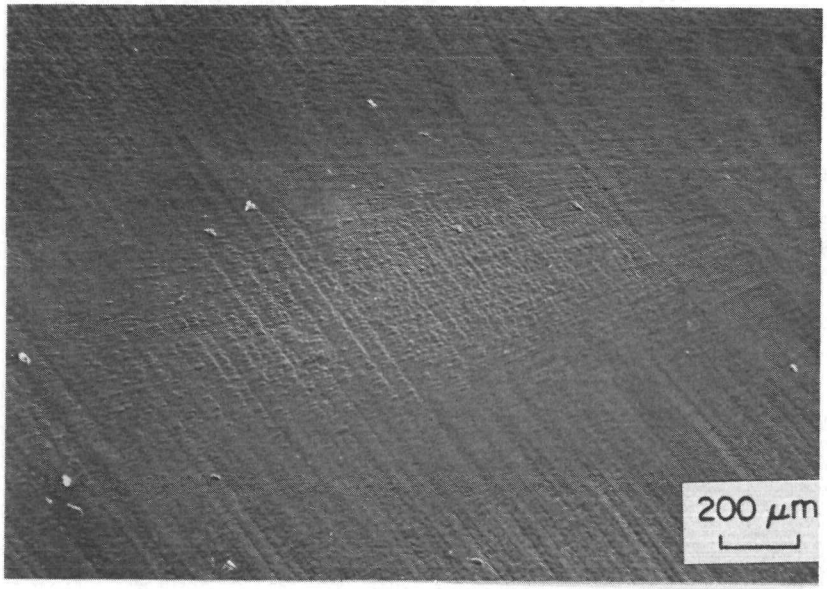

(a)

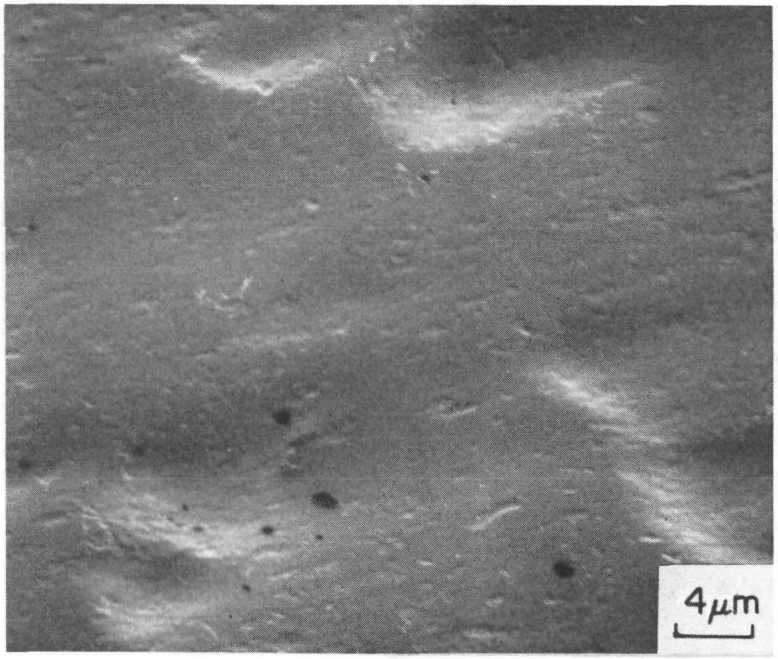

(b)

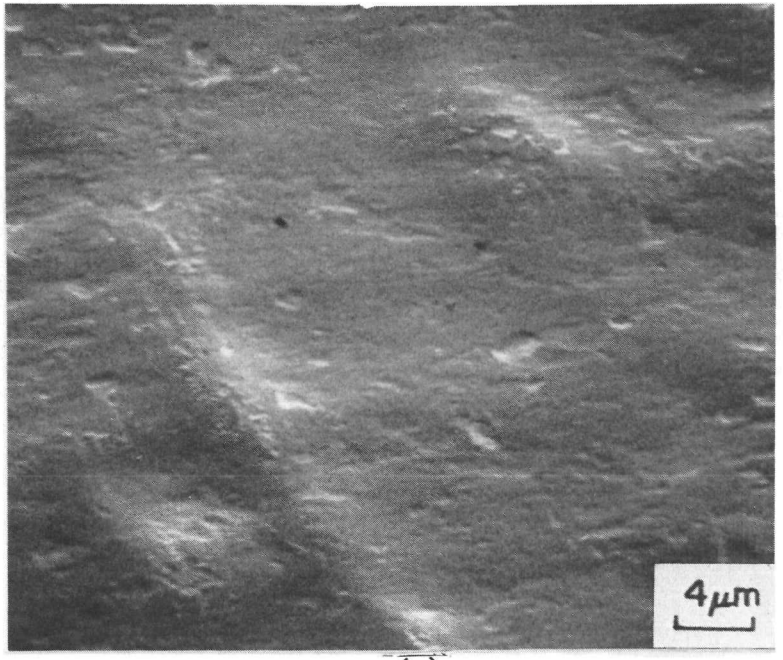

(c)

FIGURE 9. ERODED SURFACE OF CVD TiB_2 COATING, A5057-3-2; (a) Erosion Crater, (b) Exit End of Crater, (c) Inlet End of Crater

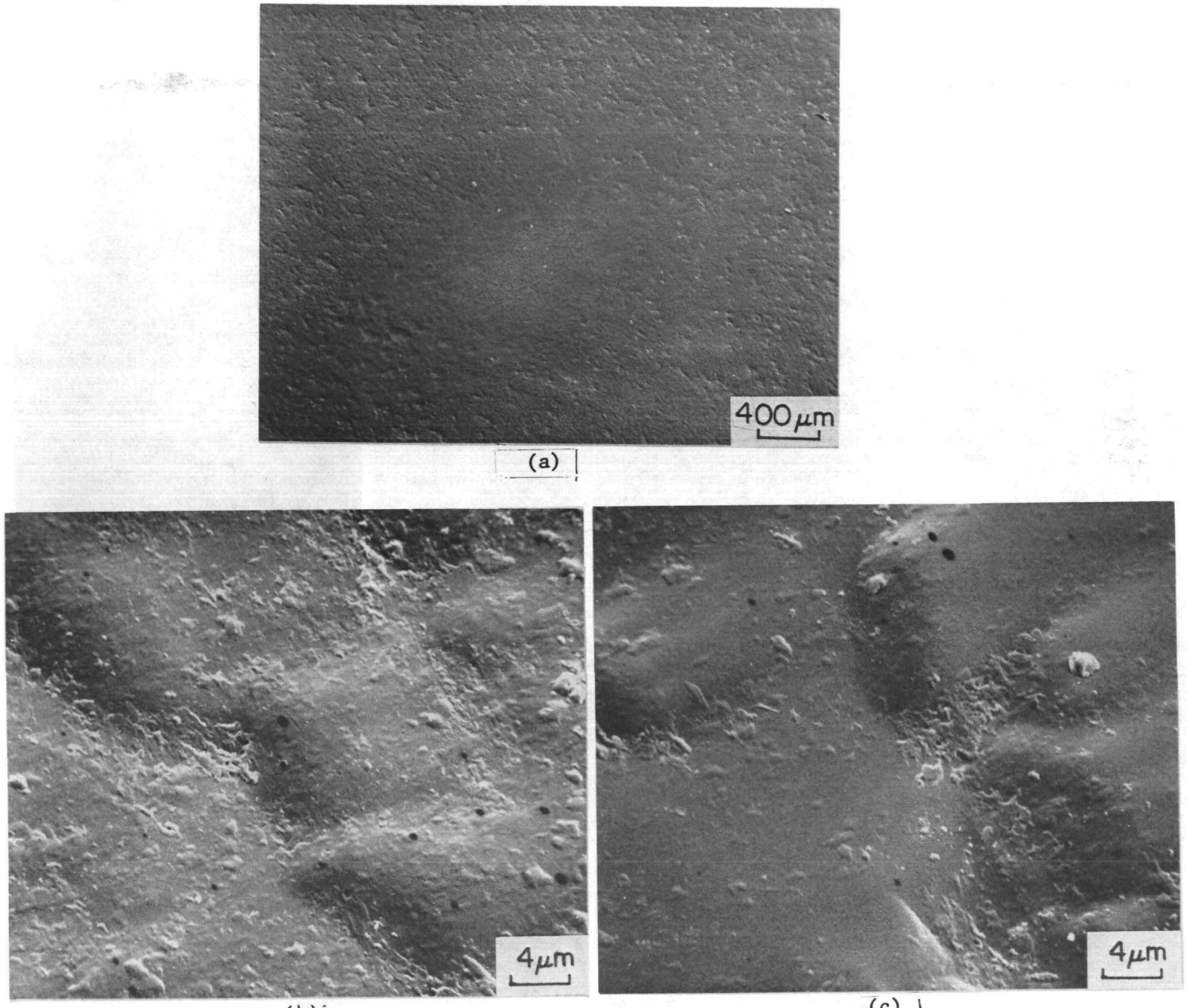

FIGURE 10. ERODED SURFACE OF CVD TiB_2 COATING A5057-2-3; (a) Erosion Crater, (b) Inlet End of Crater, (c) Exit End of Crater

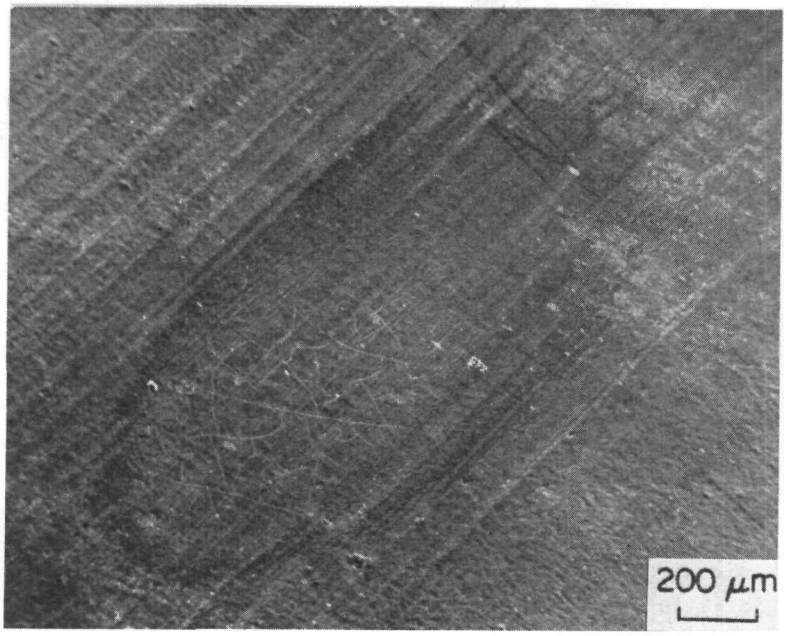

(a)

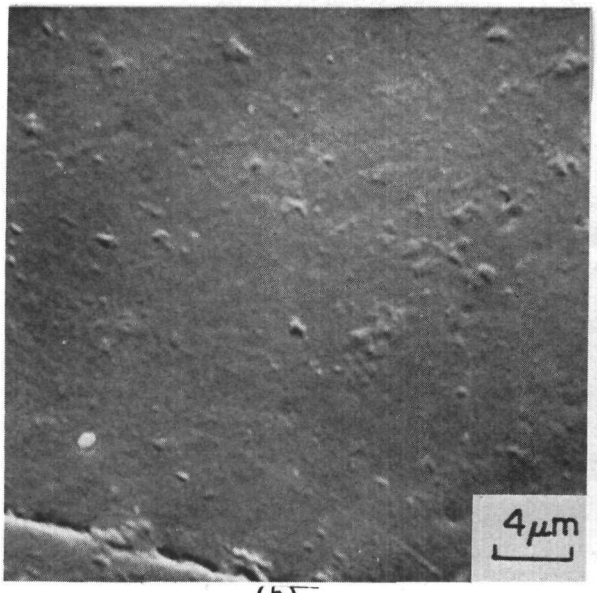

(b)

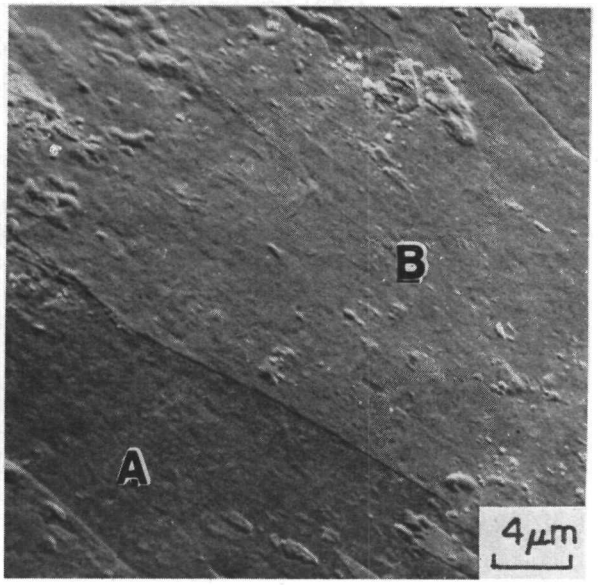

(c)

FIGURE 11. ERODED SURFACE OF TMT-745A ON K-701

(a) Erosion Crater, Showing Cracking, (b) Inlet End of Crater, (c) Exit End of Crater

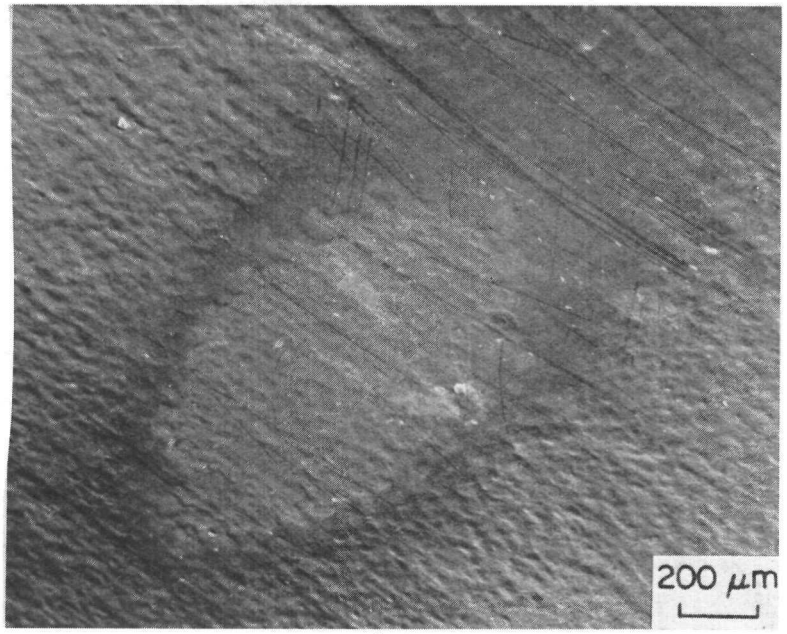

(a)

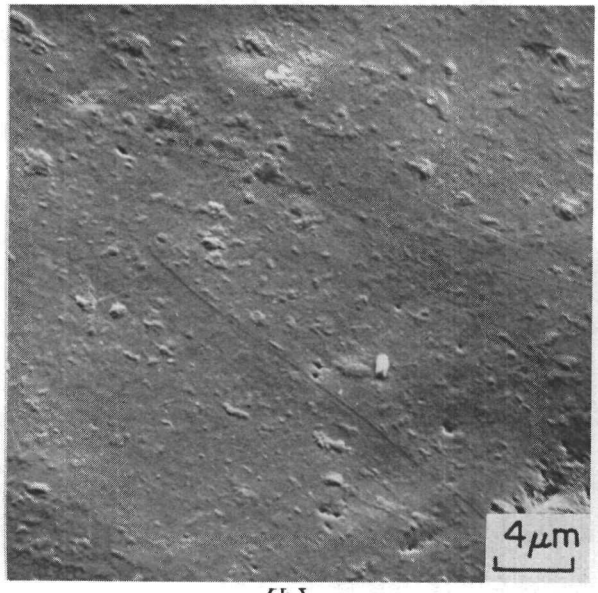

(b)

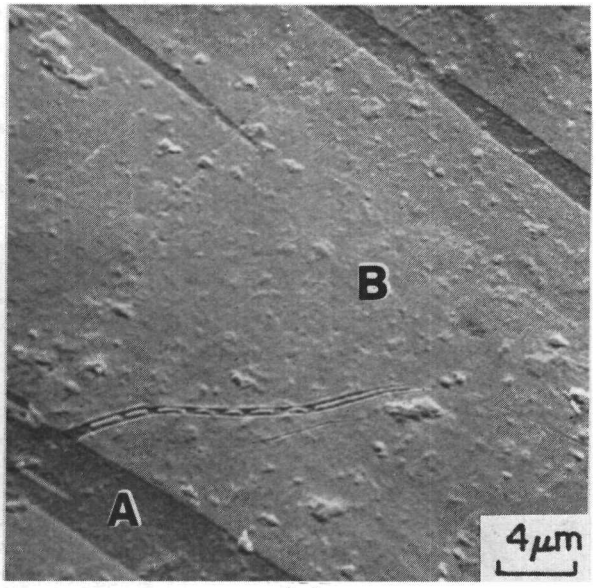

(c)

FIGURE 12. ERODED SURFACE OF TMT-745A ON K 703
(a) Erosion Crater, (b) Inlet End of Crater, (c) Exit End of Crater

TABLE 5. EROSION DATA FOR CERAMICS IN STANDARD COMPARISON TEST

Material	Designation	Source	Composition	K 701[a] Ref.	Erosion Crater	
					Depth (μm)	Length (μm)
Al_2O_3	K 060	Kennametal	Hot Pressed-SNG452T	A	17.8/22.3#	1.44/3.87 x 10^3
Al_2O_3-TiC	K 090	Kennametal	Hot Pressed	A	21.3/19.1#	1.22/3.66 x 10^3
SiAlON	Kyon 2000	Kennametal	---	A	1.4/2.3#	1.02/2.35 x 10^3
B_4C	I-HIP	Norton/BCL	Hot Isostatically Pressed B_4C	B	2.8	1.16 x 10^3

[a]: Erosion crater dimensions for reference K 701 material in the same test:

A: depth = 1.9 - 3.5 μm length = 1.07 - 3.54 x 10^3 μm.

B: depth = 3.1 - 4.7 μm length = 1.04 = 1.73 x 10^3 μm.

Duplicate runs.

TABLE 6. EROSION DATA FOR COATINGS IN STANDARD COMPARISON TEST

Material	Designation	Source	Composition	K 701[a] Ref.	Erosion Crater Depth (μm)	Erosion Crater Length (μm)
TMT-K 701	K 701/TMT 745A	Turbine Metals Technology	--	A	7.1	1.06×10^3
TMT-K 703	K 703/TMT 745A	Turbine Metals Technology	--	A	7.1	2.02×10^3
TMT-K 703	K 703/TMT 745B	Turbine Metals Technology	--	B	14.6	$1.4\text{-}4.0 \times 10^3$
CVD TiB_2 K 701	A5057-3-1	SNLA	35 μm TiB_2 coating	A	3.5	1.35×10^3
CVD TiB_2 K 701	A5057-3-2	SNLA	35 μm TiB_2 coating	A	3.3	2.59×10^3
CVD TiB_2 K 151A	A5057-2-1	SNLA	50 μm TiB_2 coating	A	7.4	0.97×10^3
CVD TiB_2 K 151A	A5057-2-2	SNLA	50 μm TiB_2 coating	A	3.5	1.12×10^3
CVD TiB_2 K 151A	A5057-2-3	SNLA	50 μm TiB_2 coating	A	6.6	1.24×10^3
CVD TiB_2-cemented TiB_2	NT90AC	ORNL/SNLA	50-100 m TiB_2 on (0.8% Ni, 1% Ni, 1% O_2, TiB_2)	A	3.4	1.54×10^3
CVD TiB_2-cemented TiB_2	NT90AD	ORNL/SNLA	50-100 m TiB_2 on (1% Ni, 1% O_2, TiB_2)	A	No measurable wear	
CVD TiB_2-cemented TiB_2	NT90J	ORNL/SNLA	50-100 m TiB_2 on (9.6% Ni, 0.7% O_2, TiB_2)	A	5.0	2.47×10^3
CVD TiB_2-cemented TiB_2	NT80"0"	ORNL/SNLA	50-100 m TiB_2 on (0.9% Ni, 8.1% O_2, TiB_2)	A	1.5	1.01×10^3
TiC-K 701	RPC-1	R-P&C Valve	20 m TiC coating	A	5.8	2.03×10^3

TABLE 6. (Continued)

Material	Designation	Source	Composition	K 701[a] Ref.	Erosion Crater Depth (μm)	Erosion Crater Length (μm)
TiC-WC	RPC-4	R-P&C Valve	20 μm TiC, 75-100 μm WC on 420 stainless steel (buffed)	A	84.8	2.13×10^3
TiC-WC	RPC-5	R-P&C Valve	20 μm TiC, 75-100 μm WC on 420 stainless steel (as dep.)	A	96.5	2.39×10^3
TiC-WC	RPC-A	R-P&C Valve	--	B	T*	---
TiC-WC	RPC-B	R-P&C Valve	--	B	T*	---
TiC-WC	RPC-C	R-P&C Valve	--	B	T*	---
TiC-K 703	T-573-4	Kennametal	25 μm TiC coating	A	7.0	2.0×10^3
TiN-K 703	T-572-2	Kennametal	37 μm TiN coating	A	9.8	1.85×10^3
η-K 703	K 703-5μ	Kennametal	5 μm^{η} on K 703	A	4.3	2.79×10^3
η-K 703	K 703-7μ	Kennametal	7 μm^{η} on K 703	A	6.3	3.00×10^3
CVD-SiC	34568-91-5	BCL	CVD SiC on graphite	B	1.1	0.97×10^3
CVD-SiC	34568-93-6	BCL	CVD SiC on graphite	B	0.6	0.29×10^3
CVD-SiC	34568-88-3	BCL	CVD SiC on graphite	B	2.5 (10.1 max)	0.93×10^3

a: Erosion crater dimensions for reference K 701 material in the same test:

A: depth = 5.3 - 6.3 μm, length = 0.76×10^3 μm.

B: depth = 3.1 - 4.7 μm, length = $1.04 - 1.73 \times 10^3$ μm.

*: depth too great to measure with profilometer.

the other normal to it, Figure 12. Cracking or crazing of the coatings had occurred in both craters, and some apparent delamination occurred in both cases at the exit ends of the craters. Surface analysis (by EDAX) indicated that the center of each crater (deepest erosion) consisted of 99% Ti, compared to the 49% Ti, 45% Co, 4% Fe, 2% Al of the non-eroded surfaces remote from the crater. The compositions of the areas A and B in Figure 11 (TMT-745A on K 701) were 97% Ti, 2% Co, 1% Cr, and 93% Ti, 3% Co, 2% Cr, and 2% Al respectively. The A and B compositions for the TMT-745A on K 703, Figure 12, were 72% Ti, 15% Co, 9% Al, 3% Fe, and 67% Ti, 22% Co, 6% Al, and 3% Fe, respectively. These results indicate that on K 701 the coating composition has a sharply rising gradient of Ti, and sharply falling gradient of Co from the surface to the 7 μm depth of the crater. In the case of the coating on K 703, the gradients of Ti and Co are less steep, but an additional gradient of Al, increasing from the surface, is present. Considerable interdiffusion is apparently a feature of this coating process, so that the delamination observed may possibly be linked to local changes in properties or compound formation resulting from the compositional gradients in the surface. The samples were returned to the supplier before any metallographic examination was performed. The cause of the cracking or crazing of the coating in the crater is not known; the specimens are subjected to a substantial thermal shock at the start of the test when they are initially impacted by the hot slurry, which could be a likely source of cracking.

The Turbine Metals Technology TMT-745B coating eroded to twice the depth of the 745A versions, but with no gross cracking or delamination. The slurry flow direction was normal to the direction of surface finish grinding lines, Figure 13, which appear to have influenced the erosion behavior to some extent. The degree of roughness or porosity of the non-eroded surface at location 4, Figure 13, is shown in Figure 14d. The structure of the eroded surface at the entrance, center, and exit points of the crater, Figures 14a, b and c, was very smooth, with small particles protruding from but apparently attached to the surface.

A 20 μm TiC coating on K 701 (RPC-1) eroded in a very smooth, uniform manner, with no evidence of preferential removal of material, except

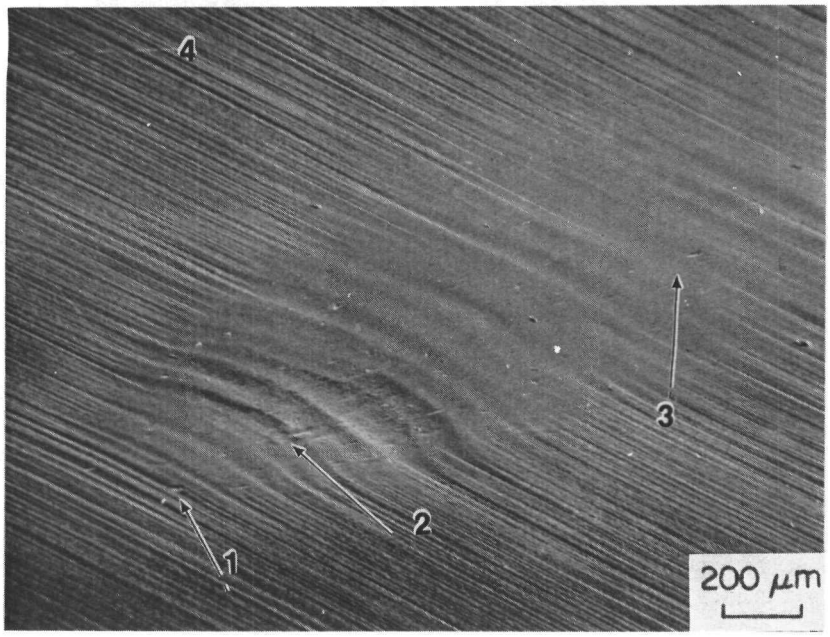

FIGURE 13. ERODED SURFACE OF TMT-745B COATING

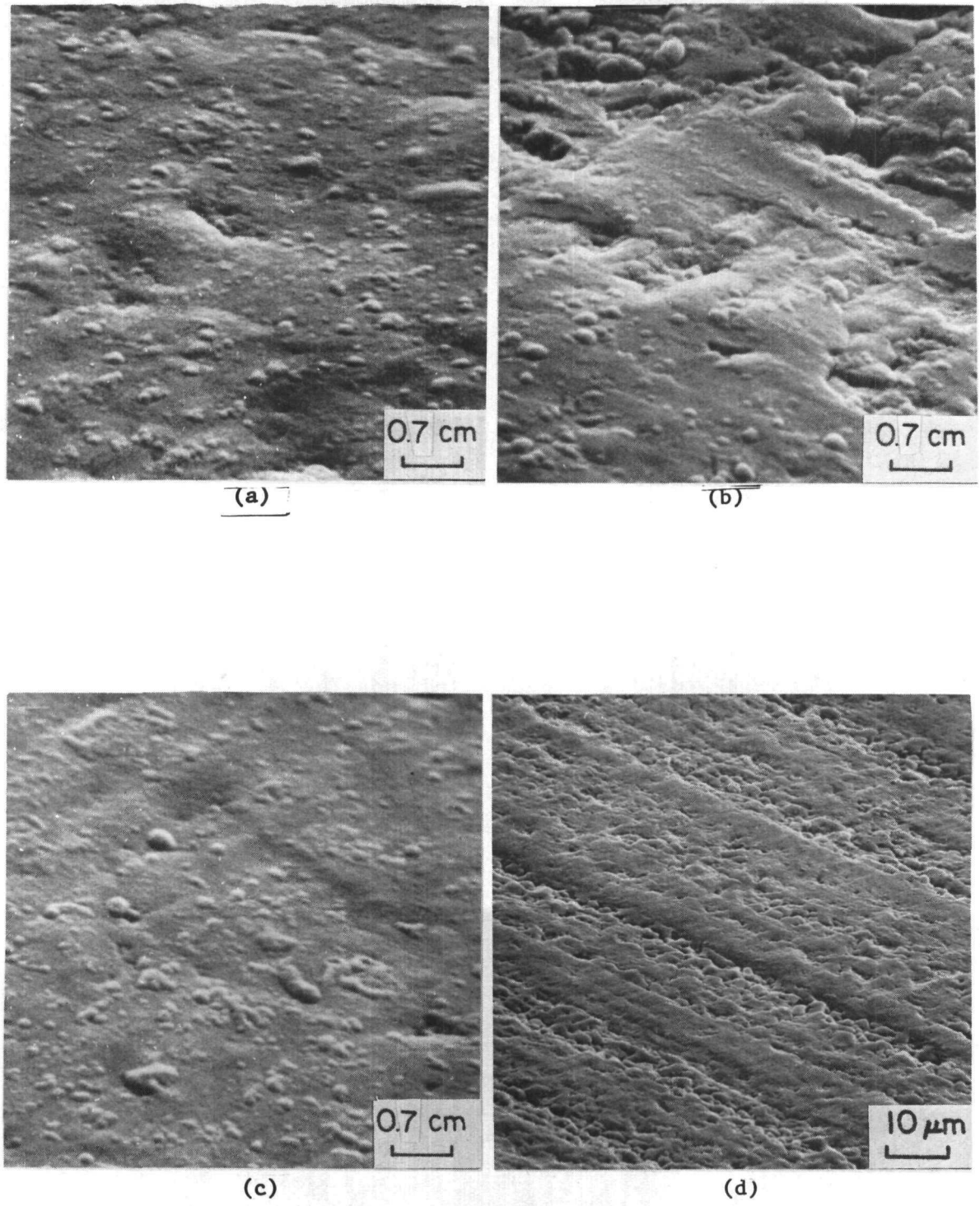

FIGURE 14. DETAILS OF SURFACE IN FIGURE 13

(a) Area 1, Entrance End, (b) Area 2, Center,

(c) Area 3, Exit End, (d) Area 4, Remote From Erosion

around areas of apparent porosity near the crater entrance, Figure 15. In contrast, a composite comprising a 20 μm TiC coating on top of a WC coating on an AISI 420 steel substrate (RPC-4,5) performed poorly. This system suffered gross cracking around the erosion crater, Figure 16, and rapid penetration of the TiC layer. There is some evidence that the TiC layer spalled or flaked in pieces up to 100 μm. The WC layer was almost completely penetrated at the end of the one-hour test exposure. The features of the eroded WC layer are shown in Figures 17 and 18; Figure 18b shows the exit end of the crater, with the smoothly polished edge of the outer TiC layer.

III.1.2 Materials Qualification Support for Pilot Plants

Pieces of actual valve stems which had been in service at the Fort Lewis SRC-2 plant, and at the Wilsonville SRC-1 plant, were prepared and run in the standard slurry erosion test, with the results shown in Table 7. The consistently good performance of the materials from Fort Lewis suggests that efficient quality control of trim materials procurement was maintained. The actual test results obtained were all similar to the best performance of the standard K 701, which is surprising. All the specimens exhibited similar erosion crater shapes, Figures 19-24, but detailed examination of the eroded surfaces showed some differences. The characteristics of the K 701 and K 703 samples corresponded to the range of erosion morphologies observed in previous tests for these materials: at the jet inlet end of the crater, more rapid removal of binder than carbide grains occurred, although obvious rounding of grains was observed. The extent of the preferential loss of binder was less at the exit end of the craters, where the slurry impact angle was presumably small. In all cases, groups of several carbide grains had been removed, leaving obvious small craters along the whole length of the macro erosion crater. Presumably these features were related to localized erosion associated with areas of porosity.

The K 602 samples exhibited a higher level of surface porosity, possibly resulting from removal of binder phase, than K 701 or K 703, but the extent of local crater formation was not obviously different from these

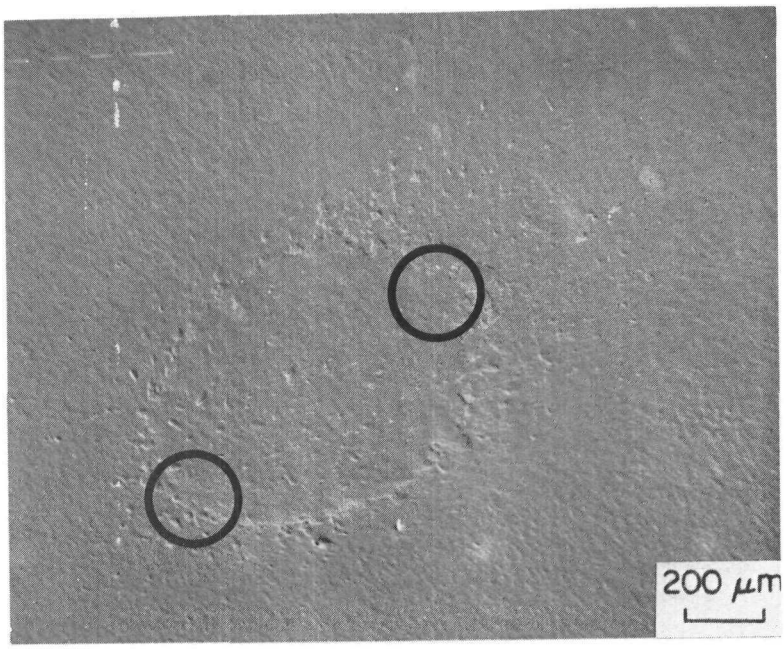

(a)

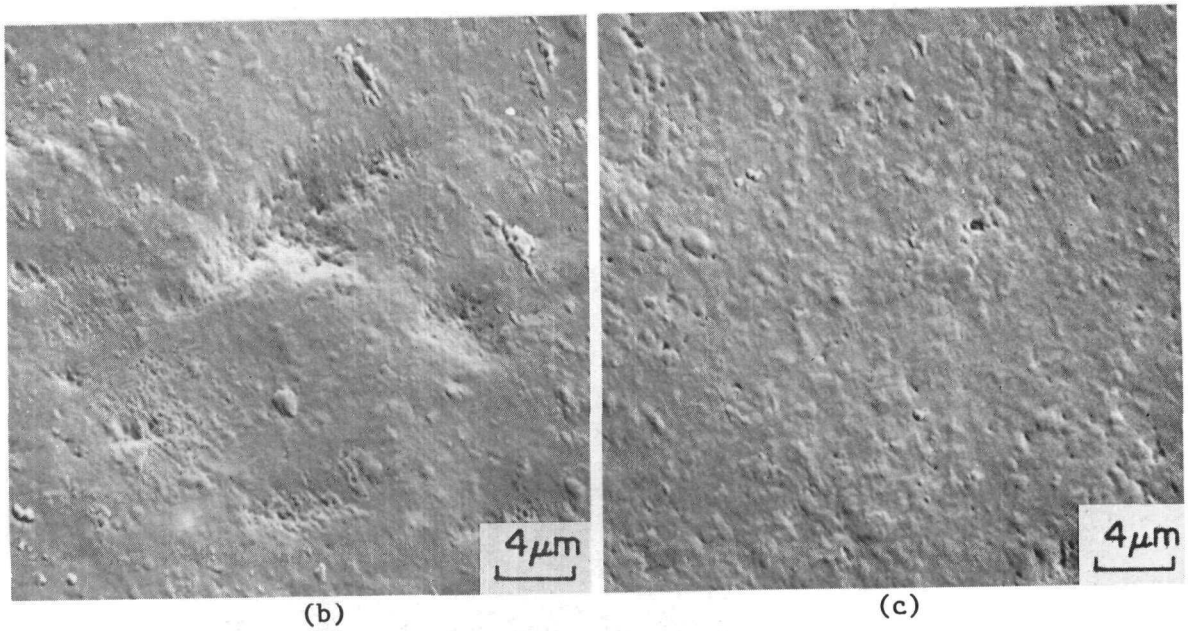

(b) (c)

FIGURE 15. ERODED SURFACE OF RPC-1 ON K 701

(a) Erosion Crater
(b) Inlet End of Crater
(c) Exit End of Crater

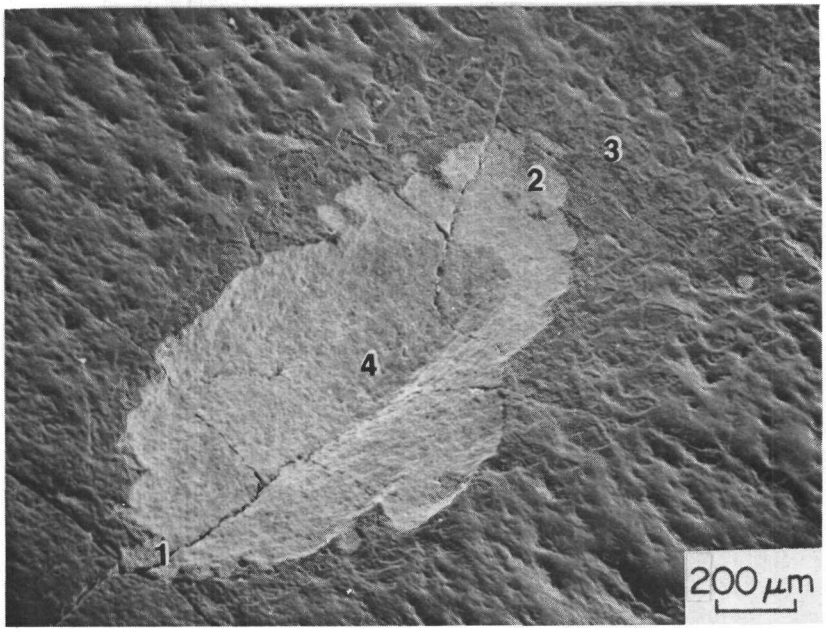

(a)

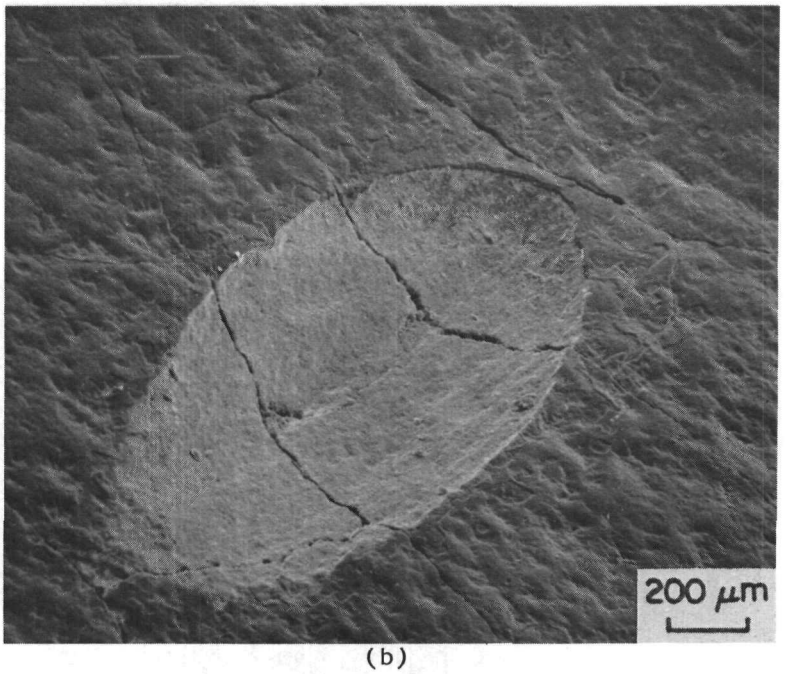

(b)

FIGURE 16. EROSION CRATERS ON:

(a) RPC-4 and
(b) RPC-5, Showing Cracking

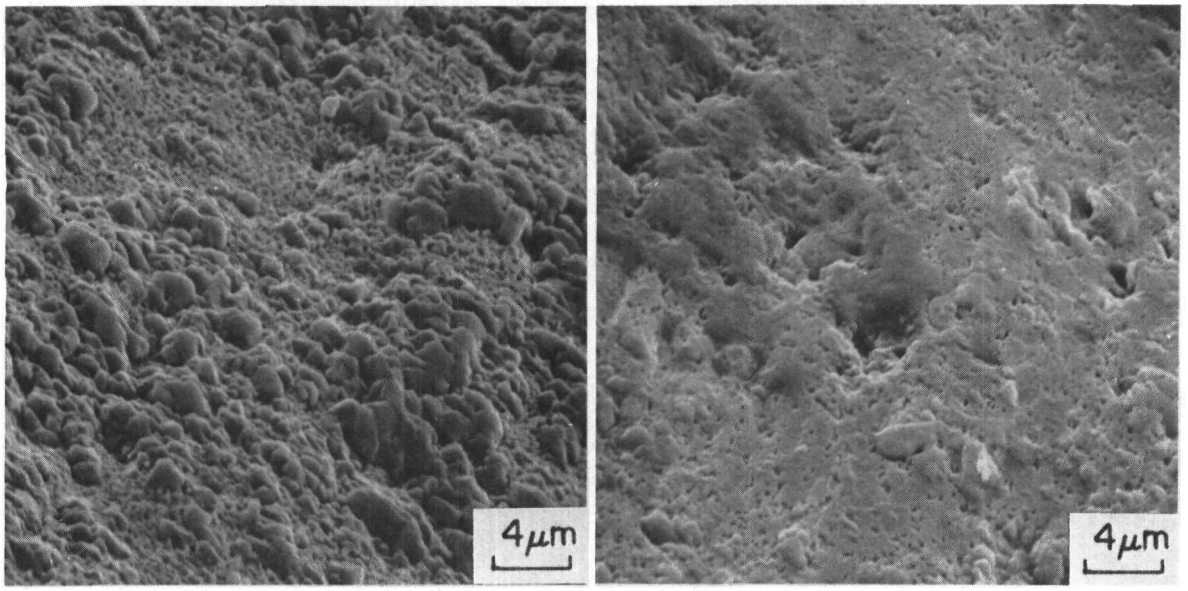

(a) (b)

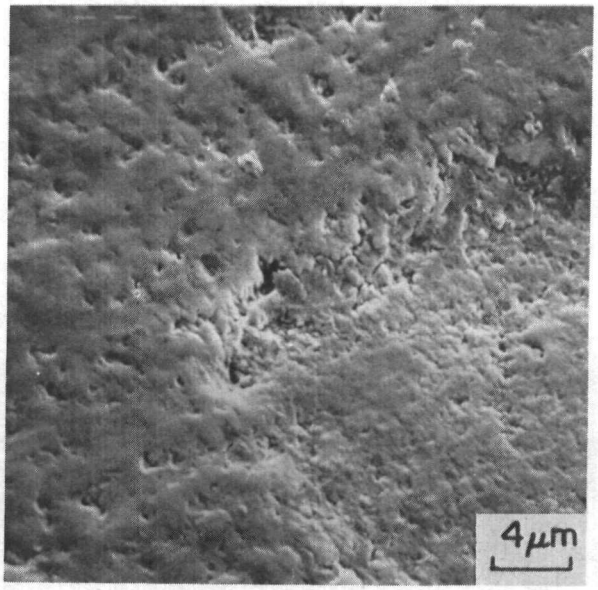

(c)

FIGURE 17. DETAILS OF ERODED SURFACE OF RPC-4

(a) Inlet End of Crater, Area 1
(b) Exit End of Crater, Area 2
(c) Center of Crater, Area 4

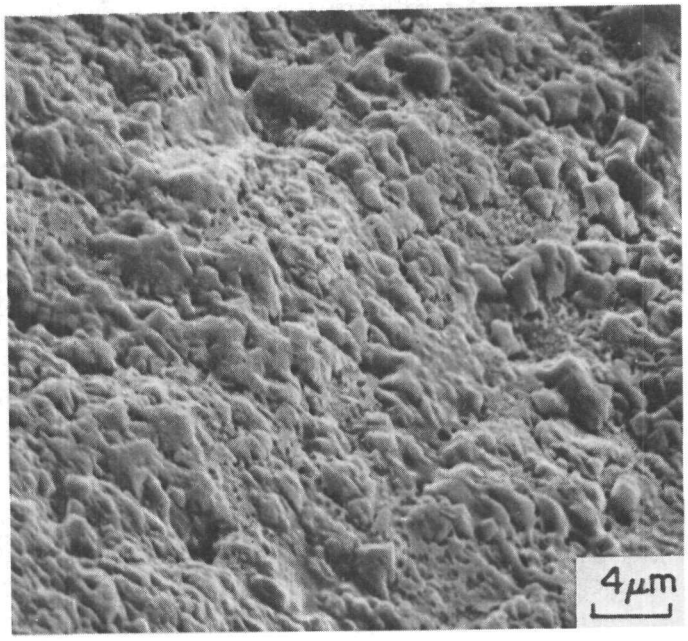

(a)

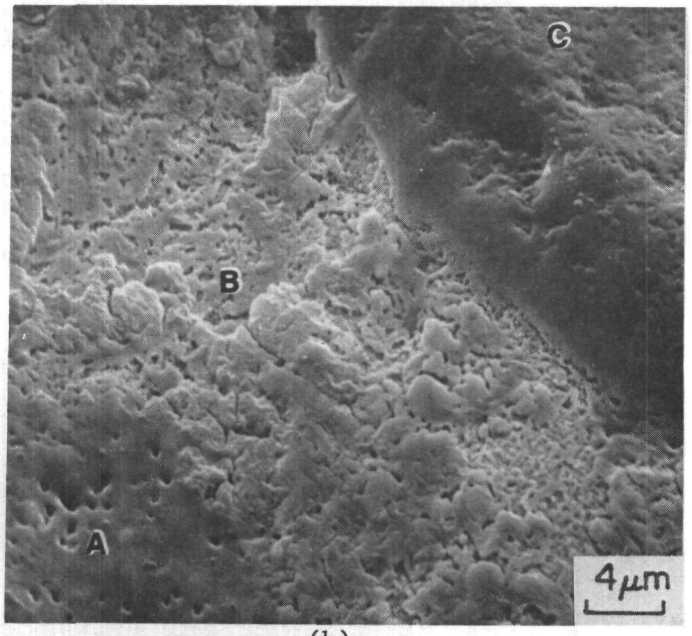

(b)

FIGURE 18. DETAILS OF ERODED SURFACE OF RPC-5

(a) Inlet End of Crater
(b) Exit End, Showing Smooth Surface of Underlying Steel (A); Loss of Apparently Whole Grains of Steel (B); and Edge of Coating (C)

TABLE 7. TRIM MATERIALS FROM PILOT PLANTS, STANDARD TEST

Material	Specimen Designation	Source	K 701[a] Ref.	Erosion Crater Depth (μm)	Erosion Crater Length (μm)
K 602	FL-1	Fort Lewis	A	2.9	2.29×10^3
K 602	FL-5	Fort Lewis	A	3.4	2.08×10^3
K 701	FL-3	Fort Lewis	A	3.9	2.21×10^3
K 701	FL-4	Fort Lewis	A	2.7	2.08×10^3
K 701	FL-6	Fort Lewis	A	3.4	1.78×10^3
K 703	FL-2	Fort Lewis	A	2.3	2.41×10^3
WC/TMT	TMT-5	H-Coal, Catlettsburg	A	Too deep to measure	
K 703	E-288	Wilsonville (McCartney)	B	Too deep to measure	
K 703	E-1200	Wilsonville (McCartney)	B	2.8	1.27×10^3
GEM 550	E-2000	Wilsonville (GEMOCO)	B	3.8	1.28×10^3
GEM 550	E-4000	Wilsonville (GEMOCO)	B	1.6	0.71×10^3

[a]A: depth = 3.1 - 5.8 μm, length = 1.1 - 1.3 x 10^3 μm.
B: depth = 1.8 - 2.8 μm, length = 3.1 - 3.6 x 10^3 μm.

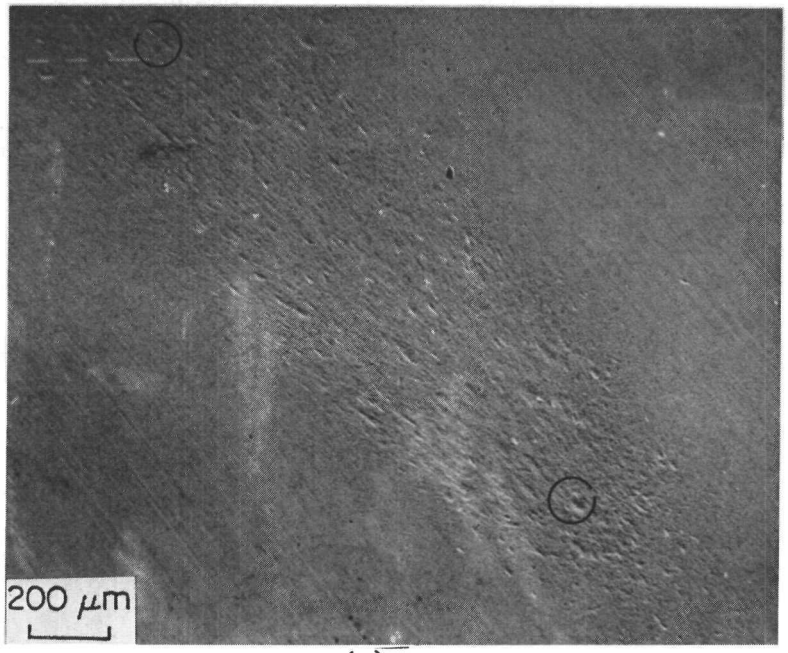

(a)

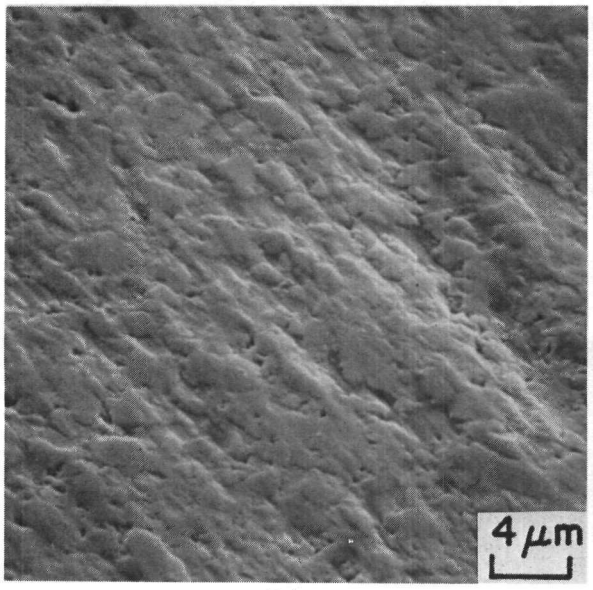

(b)

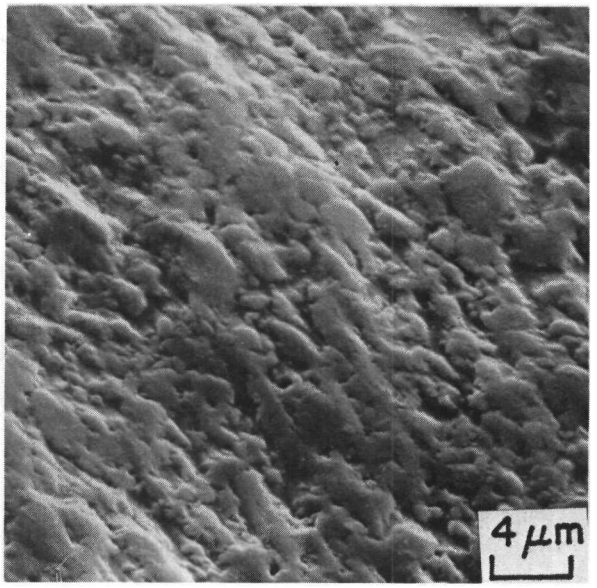

(c)

FIGURE 19. ERODED SURFACE OF K 701 TRIM (FORT LEWIS, FL-3)

(a) Erosion Crater
(b) Exit End
(c) Inlet End

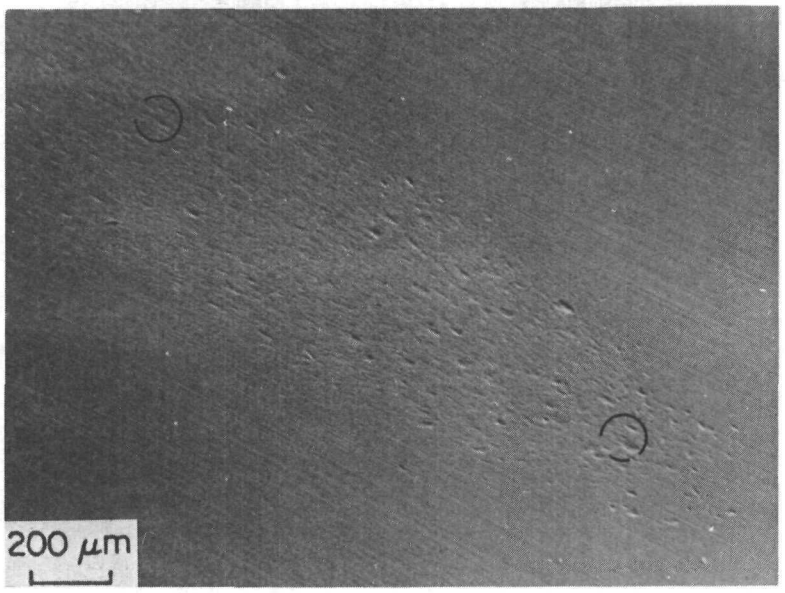

(a)

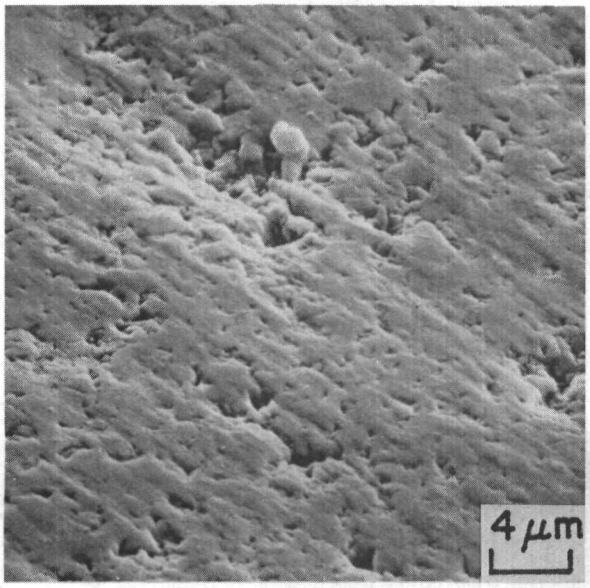

(b)

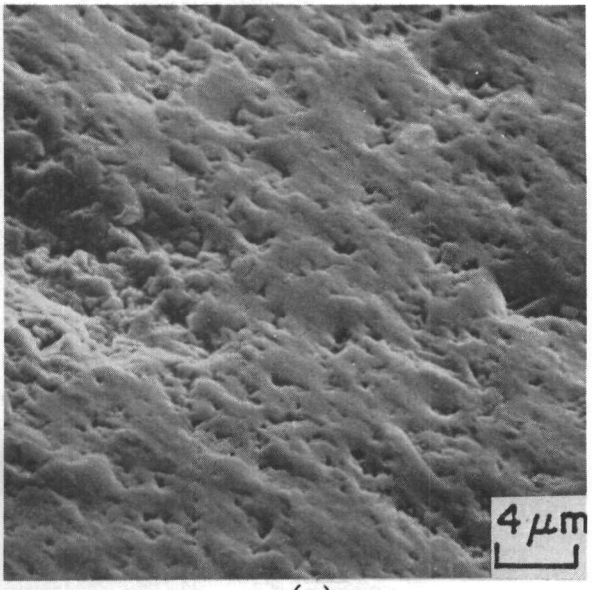

(c)

FIGURE 20. ERODED SURFACE OF K 701 TRIM (FORT LEWIS, FL-4)

(a) Erosion crater
(b) Exit end
(c) Inlet end

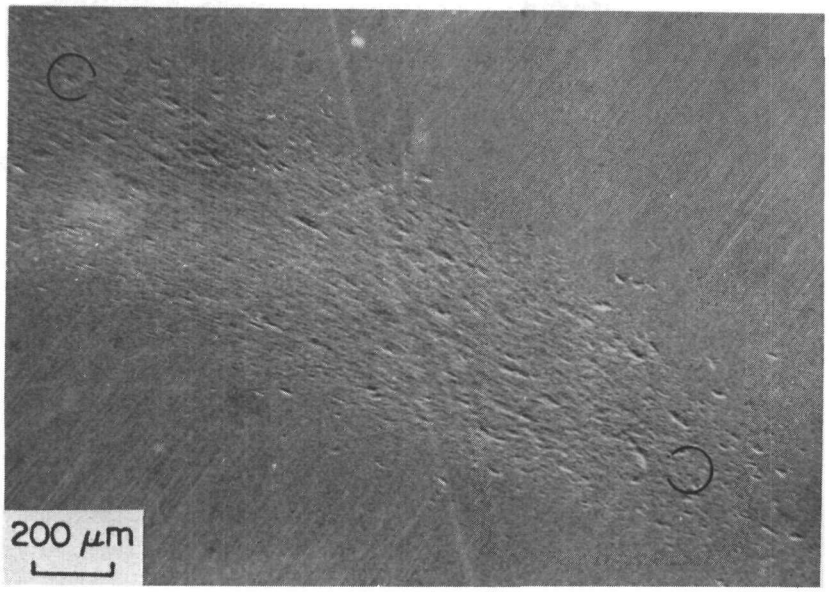

(a)

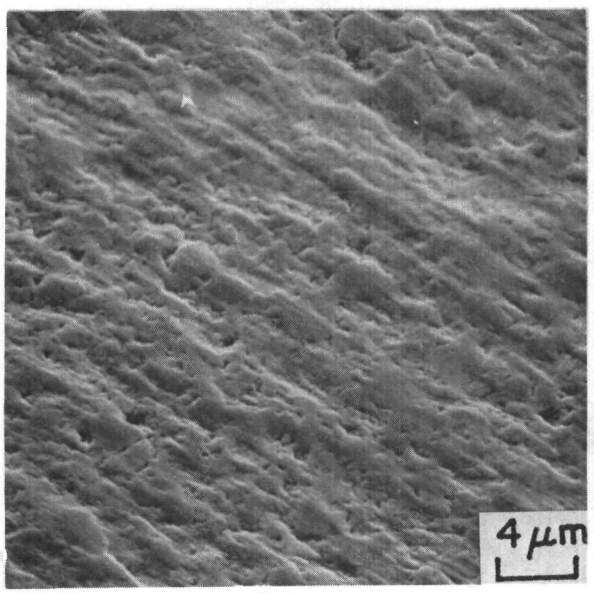

(b)

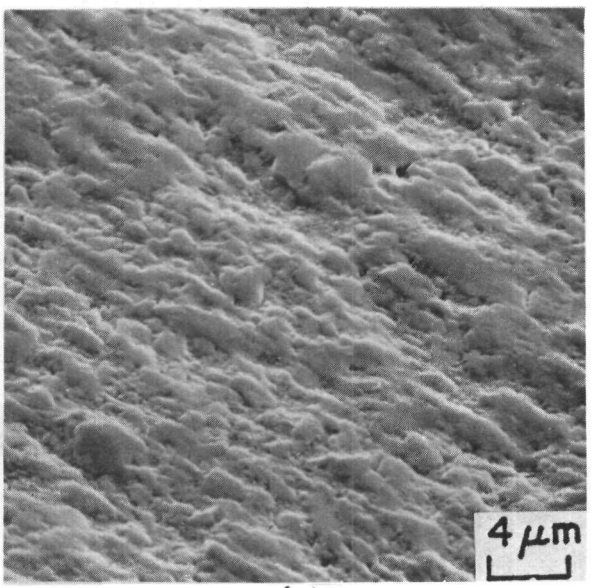

(c)

FIGURE 21. ERODED SURFACE OF K 701 TRIM (FORT LEWIS, FL-6)

(a) Erosion crater
(b) Exit end
(c) Inlet end

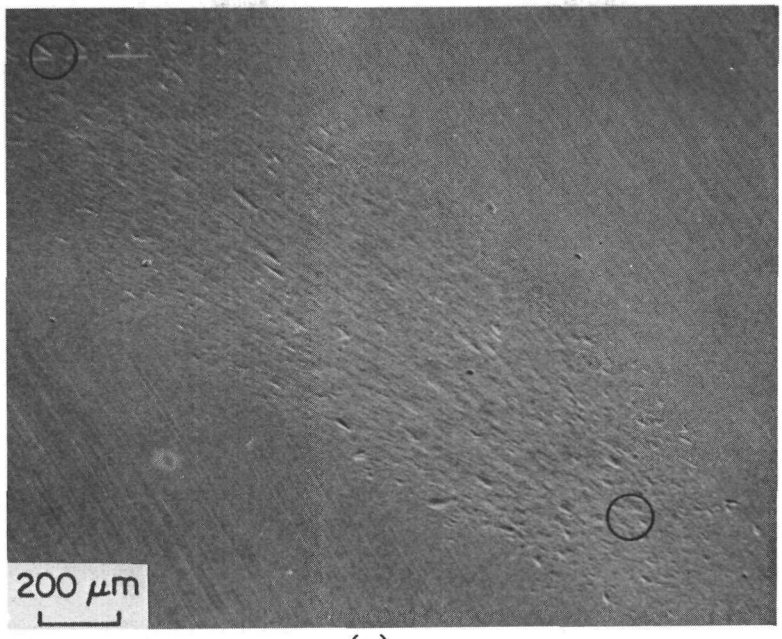

(a)

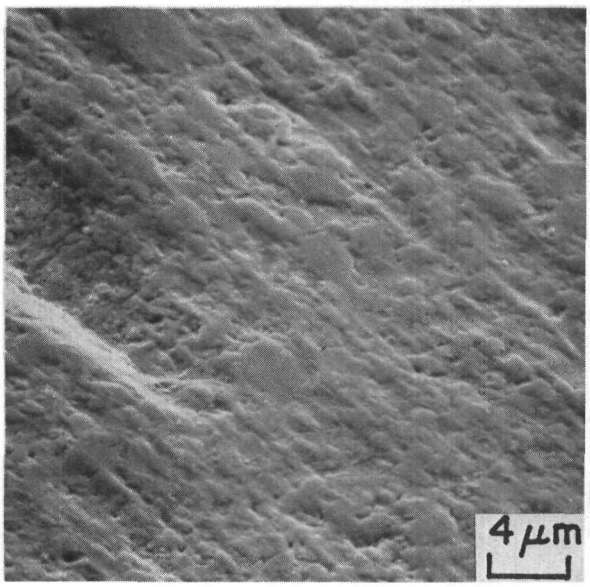

(b)

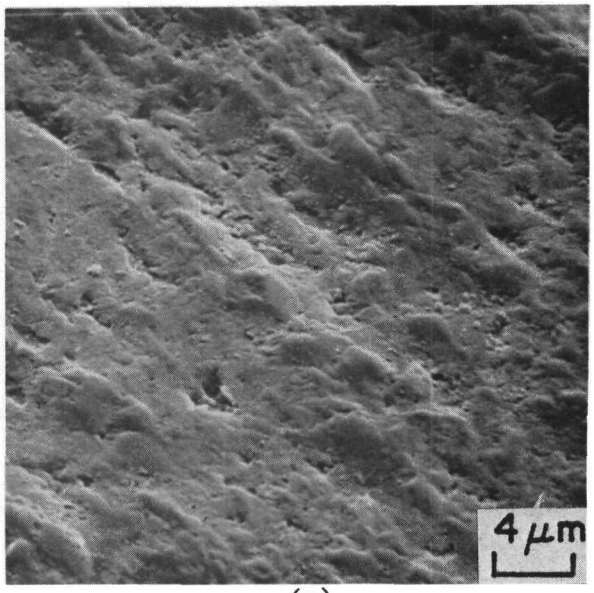

(c)

FIGURE 22. ERODED SURFACE OF K 703 TRIM (FORT LEWIS, FL-2)

(a) Erosion crater
(b) Exit end
(c) Inlet end

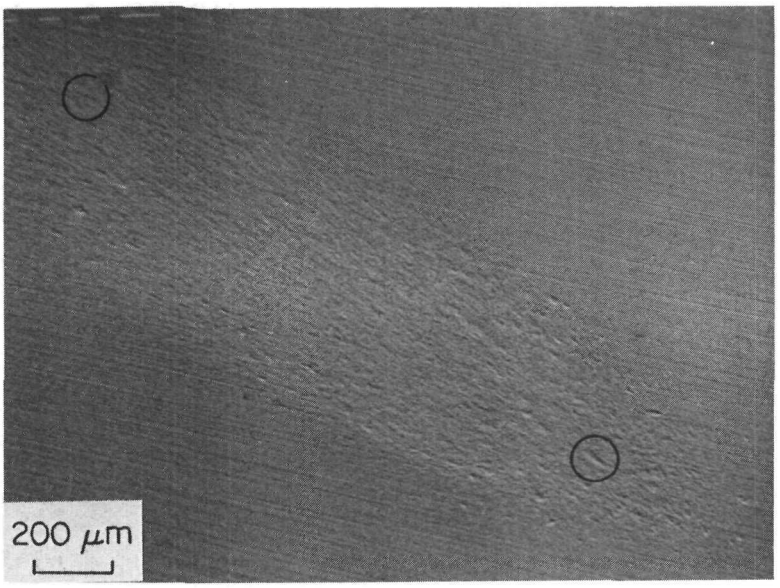

(a)

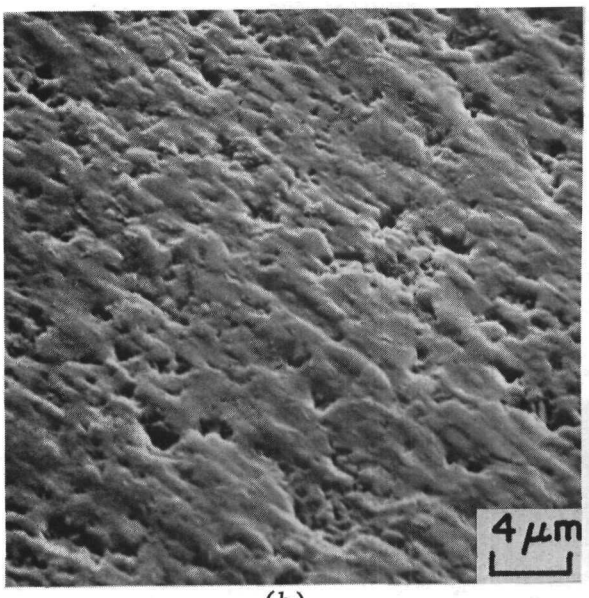

(b)

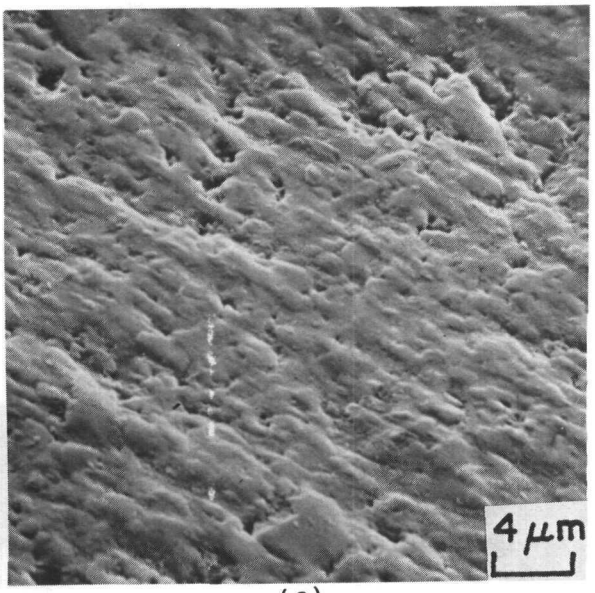

(c)

FIGURE 23. ERODED SURFACE OF K 602 TRIM (FORT LEWIS, FL-1)

(a) Erosion crater
(b) Exit end
(c) Inlet end

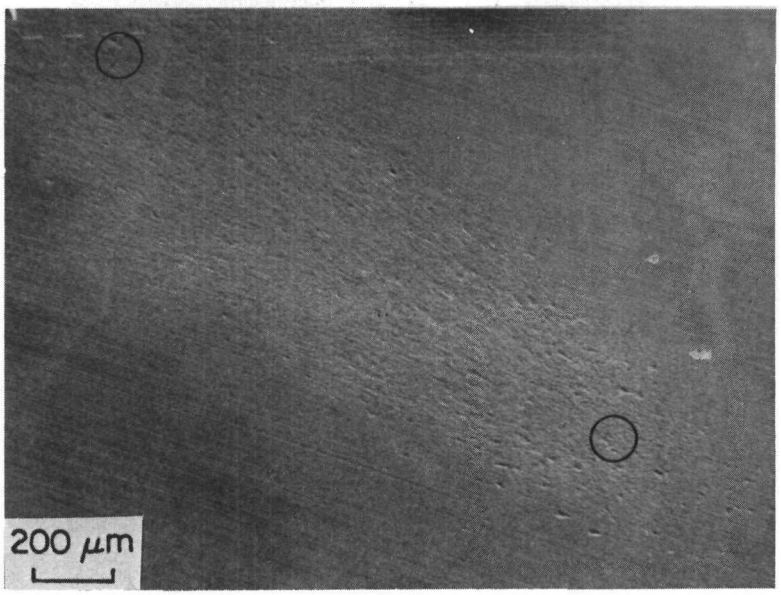

(a)

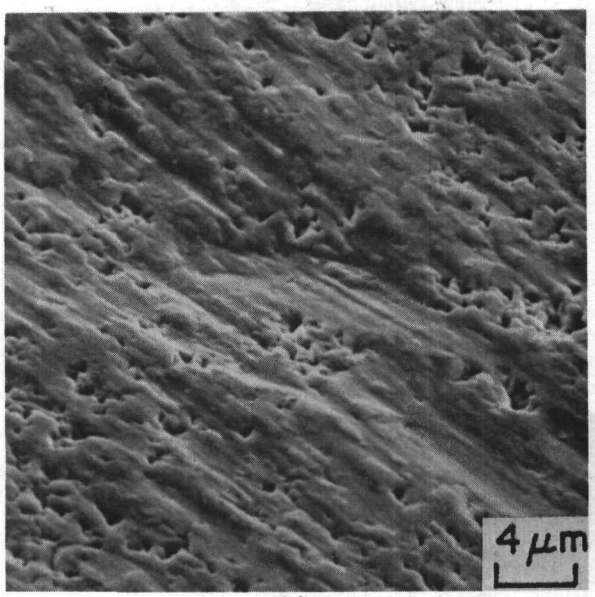

(b)

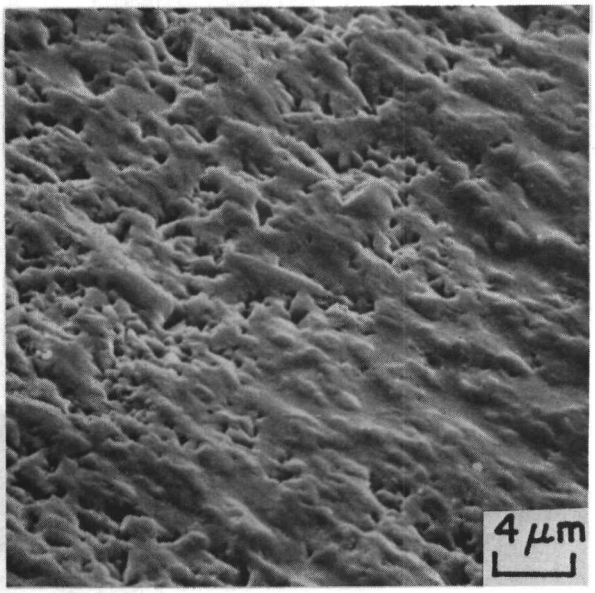

(c)

FIGURE 24. ERODED SURFACE OF K 602 TRIM (FORT LEWIS, FL-5)

(a) Erosion crater
(b) Exit end
(c) Inlet end

materials. Smooth groove-like features in the exit end of the crater on FL-5 suggested that a process of ductile ploughing by large erodent particles may have occurred in this specimen, although it is difficult to explain how this could have happened in the test system used. No effects of the large eta-phase precipitates usually present in K 602 were observed in the erosion behavior.

The cemented tungsten carbide trim from Wilsonville gave erosion test results which corresponded reasonably well with the erosion lifetimes found in practice. Metallographic examination of these materials at the Oak Ridge National Laboratory revealed undesirable microstructural features such as porosity in sample E-288, inhomogeneity in E-4000, and eta-phase precipitates in E-1200.

The performance in the standard test of a specimen cut from a TMT-5 coated, cemented tungsten carbide disc from a Willis choke valve used at the Catlettsburg H-Coal Plant was very poor (Table 7). Metallographic examination of cross sections revealed that the outer 10-15 μm of surface responded differently to metallographic preparation than the bulk of the material, Figure 25, and contained some fine porosity. This appears to represent an outer case of material affected by the coating process. Spot analysis by EDAX indicated no great difference in composition between the bulk (presumed unaffected) alloy and the case. Typical analyses are:

bulk: 92% W, 7% Co, 1% Fe
case: 89-92% W, 8-10% Co, 1% Fe.

The edges of the holes in the disc, and the outer edges of the disc, exhibited gross porosity, as shown in Figure 25(b). The origin of this porosity is not known. The edges of the holes would have experienced the full force of slurry flow during throttling of the Willis valve, hence such porosity may have been a contributing factor to the irregular performance that was observed.

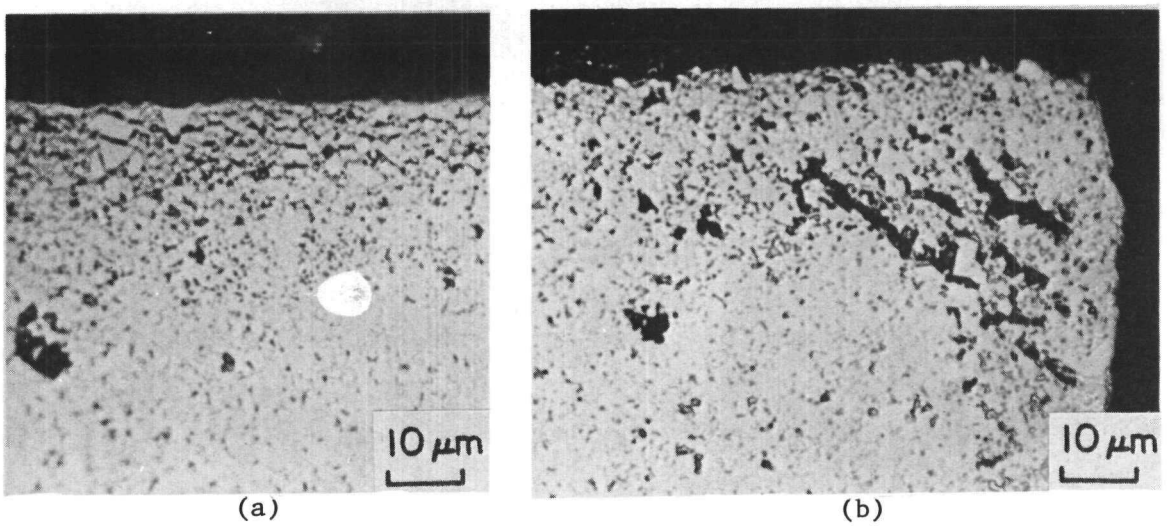

(a) (b)

FIGURE 25. CROSS SECTIONS OF TMT-5 COATED WC-Co DISC, FROM WILLIS VALVE, CATLETTSBURG

(a) Typical appearance
(b) Corner of hole (flow passage)

III.2 Characterization of Erosion Behavior of Selected Materials

The objective of this task was to investigate the mechanisms by which specific classes of advanced materials are eroded by coal-derived slurries. The mechanisms of erosion were assessed on the basis of the results obtained in one or more of the following studies.

- Examination of the eroded target surfaces to assess the role of the material microstructures
- Correlation of the erosion wear rates with critical target mechanical properties such as hardness and fracture toughness
- Evaluation of the slurry jet angle and velocity dependence of erosion rates
- Comparison of the experimental results with predictions of theoretical models.

The majority of the erosion mechanism studies were conducted with the coal-derived slurry prepared by dissolving the Wilsonville SRC product in anthracene oil. While this reconstituted slurry served to simulate the slurry conditions in letdown valves in coal-liquefaction pilot plants, it was found to be less than ideally suited for mechanistic studies. It is well known from studies of erosion from particle impingement that erosion response of targets is significantly influenced by the physical characteristics of the impinging particles (size, shape, hardness, and elastic properties) in addition to the target properties (hardness and/or fracture toughness) or the particle impingement variables (velocity and impingement angle)[6]. Insoluble particles in the reconstituted coal slurry are quite variable in size, shape, and composition.[3] Target erosion from the coal slurry was also complicated by the agglomeration and deagglomeration of inorganic ash and undissolved, long-chain organic residue. To eliminate these limitations of the coal-slurry, a substitute, artificial slurry with well-defined erodent characteristics was developed. The artificial slurry was used to characterize the erosion behavior of selected target materials. The erosion rates and the erosion mechanisms obtained from both the artificial slurry and the coal-derived slurry were critically compared with a number of target materials.

In addition to these needs for a well characterized erodent and slurry for the basic research aspects of erosion behavior, there is also a continuing and growing demand for a standardized test procedure for use in comparing the erosion performance of new or modified materials. While Battelle's slurry erosion test, using the reconstituted Wilsonville SRC product in anthracene oil, has been used for this purpose, experiments with a less complicated and potentially more easily duplicated test system would be desirable.

III.2.1 Erosion Behavior of Cemented Carbides of Different Binder Contents and Compositions

In an attempt to provide some rationalization of the erosion behavior of the many cermet materials studied, values of hardness and, where elastic modulus data were available, fracture toughness were measured for selected samples of the WC-series by an indentation technique described in Appendix A. The measured values are listed in Table 8. The trend of increasing fracture toughness with increasing binder content, shown in Figure 26, is similar (with the notable exception of K 701) to that determined by other workers[7], albeit for a constant carbide grain size of 2.2 μm. These same workers also found that fracture toughness increased with increasing WC grain size over the range 0.7 to 2.2 μm. As can be seen from the micrographs of some of the WC-cermets used in the present work, Figure 28, the grain size ranged from apparently uniformly small ($\sim$ 1-2 μm, for K 68 and SP 2313) to large (5-25 μm for K 6T, K 3560, WCX). In addition, the compositions of the carbide and binder phases spanned a range (Table 8). Similarly, the relationship of fracture toughness to hardness, shown in Figure 27, follows trends observed elsewhere.

Figure 29 shows the apparent relationship of normalized erosion rates (with respect to K 701 using the erosion data from Table 1) to the inverse of hardness. There appears to be a trend to decreasing erosion rate with increasing hardness (i.e., decreasing binder level and fracture toughness), with a minimum occurring at a given hardness, followed by a very sharp

TABLE 8. MEASURED HARDNESS AND FRACTURE TOUGHNESS VALUES

Material	Reference	Composition (wt %)	Hardness (GPa)	K_{Ic} (MPa. $m^{1/2}$)
WC	WCX	WC-0.75 Ni	13.0	a
WC/TiC	SP 278	WC-0.5 Co, 3TaC, 20 TiC, 0.1 NbC	17.6	b
WC-Co	K 602	WC-1.7 Co, 10 TaC, 0.2 TiC, 0.1 NbC	20.2	5.0
WC-Co	K 6T	WC-6 Co, 0.5 (TaC, TiC, NbC)	12.3	a
WC-Co	SPZ 313		18.7	b
WC-Co	K 11	WC-2.8 Co	19.1	8.5
WC-Co	K 68	WC-5.8 Co	17.6	10.9
WC-Co	K 3406	WC-7.8 Co	13.2	17.9
WC-Co	K 3560	WC-9.5 Co	10.6	a
WC-Co	K 3109	WC-12.2 Co	11.6	a
WC-Co	WA-4	WC-3 Co	17.8	7.7
WC-Co	WA-3	WC-4.3 Co	16.8	9.4
WC-Co	WA-2	WC-6 Co	16.0	11.3
WC-Co	WA-41	WC-9 Co	13.7	15.6
WC-Co	WA-110	submicron carbide	15.2	b
WC-Co, Cr	K 714	WC-6 Co, 0.9 Cr, 4.2 TaC, 4 TiC, 0.9 NbC	16.5	13.0
WC-Co, Cr	K 701	WC-8.5 Co, 4.5 Cr	16.1	7.0
WC-CO, Cr	K 703	WC-6 Co, 1.0 Cr	17.0	10.2
WC-Co, Cr	K 703	WC-6 Co, 1.0 Cr	16.8	10.6
TiB_2-Ni			25.3	b
Al_2O_3	BCL-HIP	Hot isostatically pressed	21.9	b

(a) No cracks observed around indentations.
(b) Modulus value unknown.

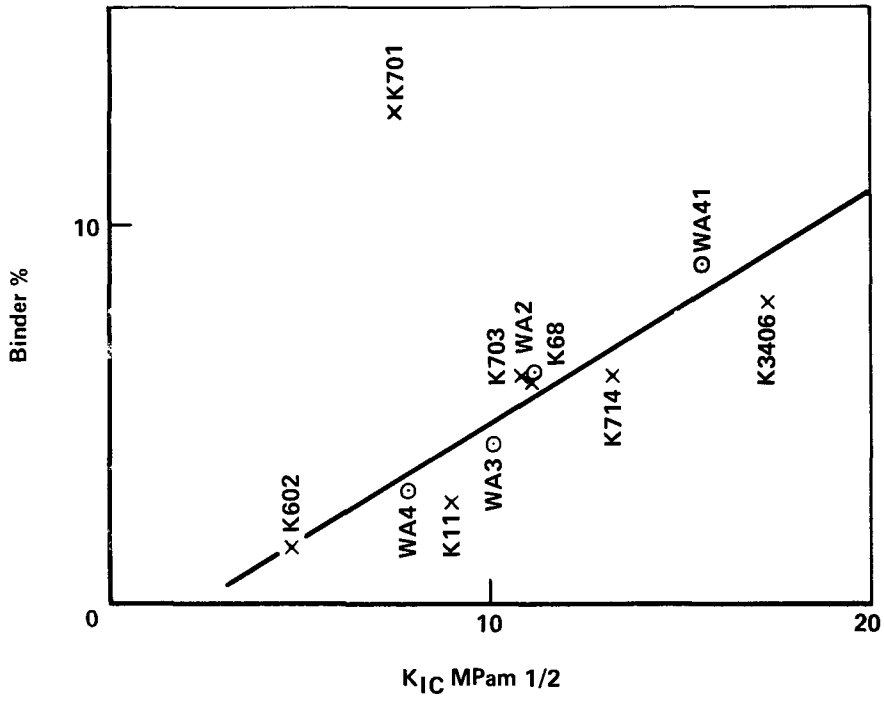

FIGURE 26. RELATIONSHIP OF FRACTURE TOUGHNESS TO BINDER CONTENT FOR WC-CERMETS

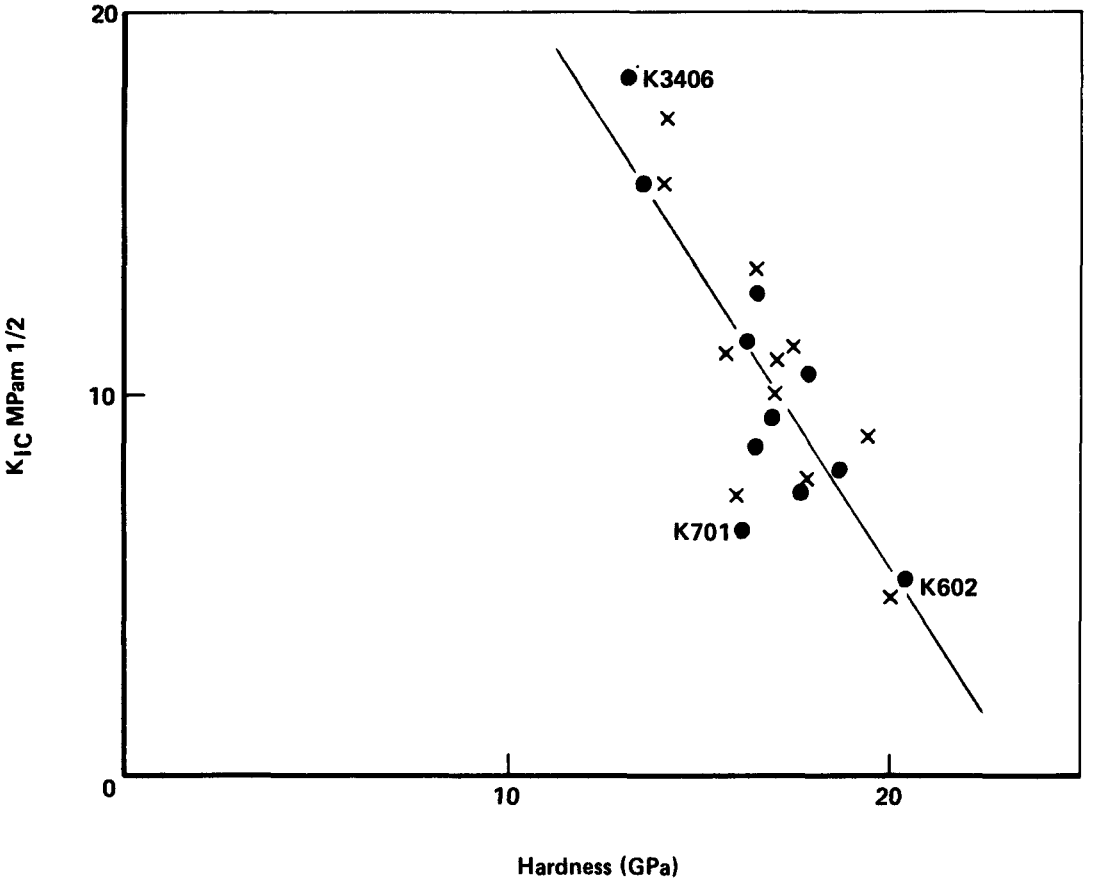

FIGURE 27. FRACTURE TOUGHNESS-HARDNESS RELATIONSHIP FOR WC-CERMETS

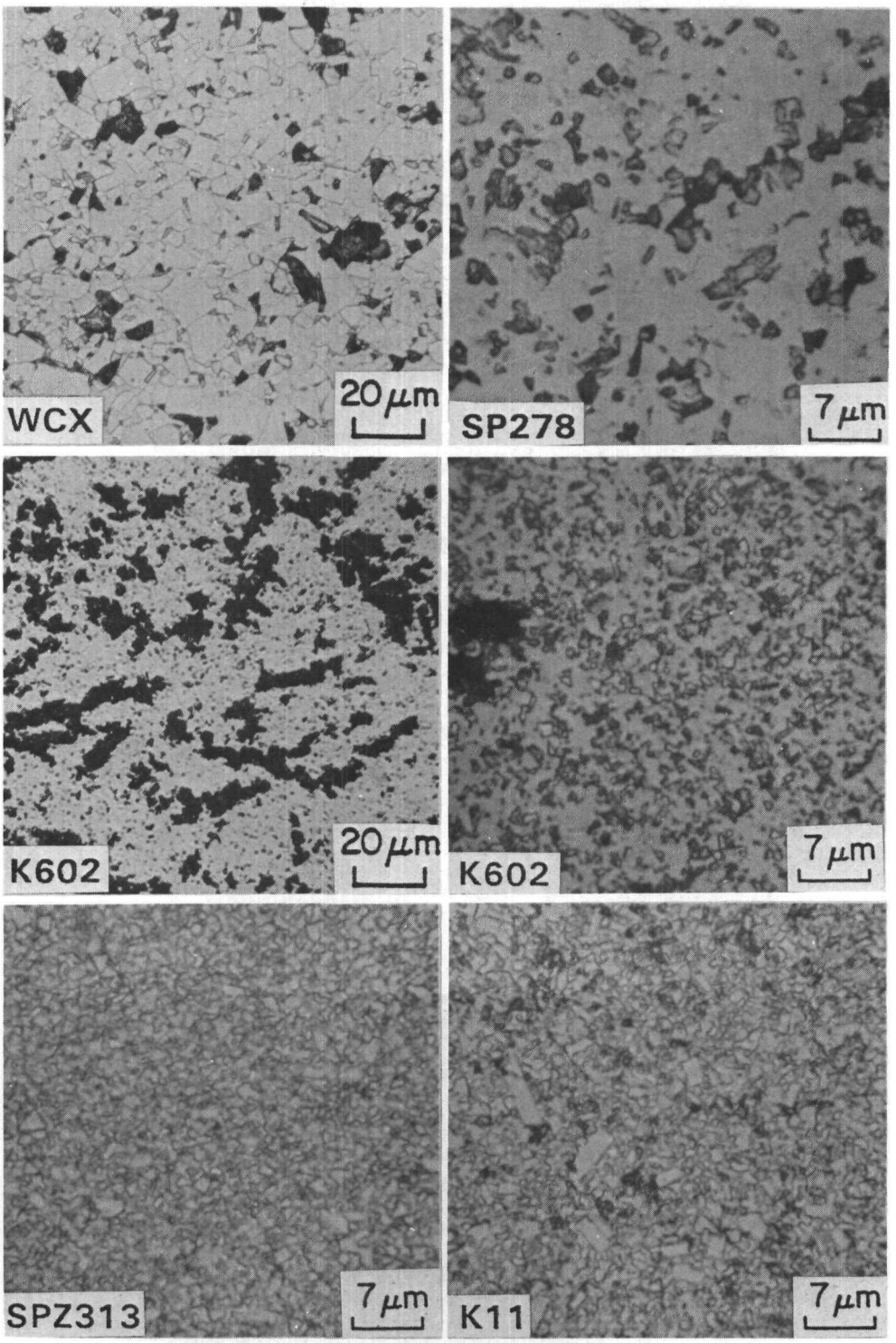

FIGURE 28. MICROSTRUCTURES OF SOME WC-Co CERMETS

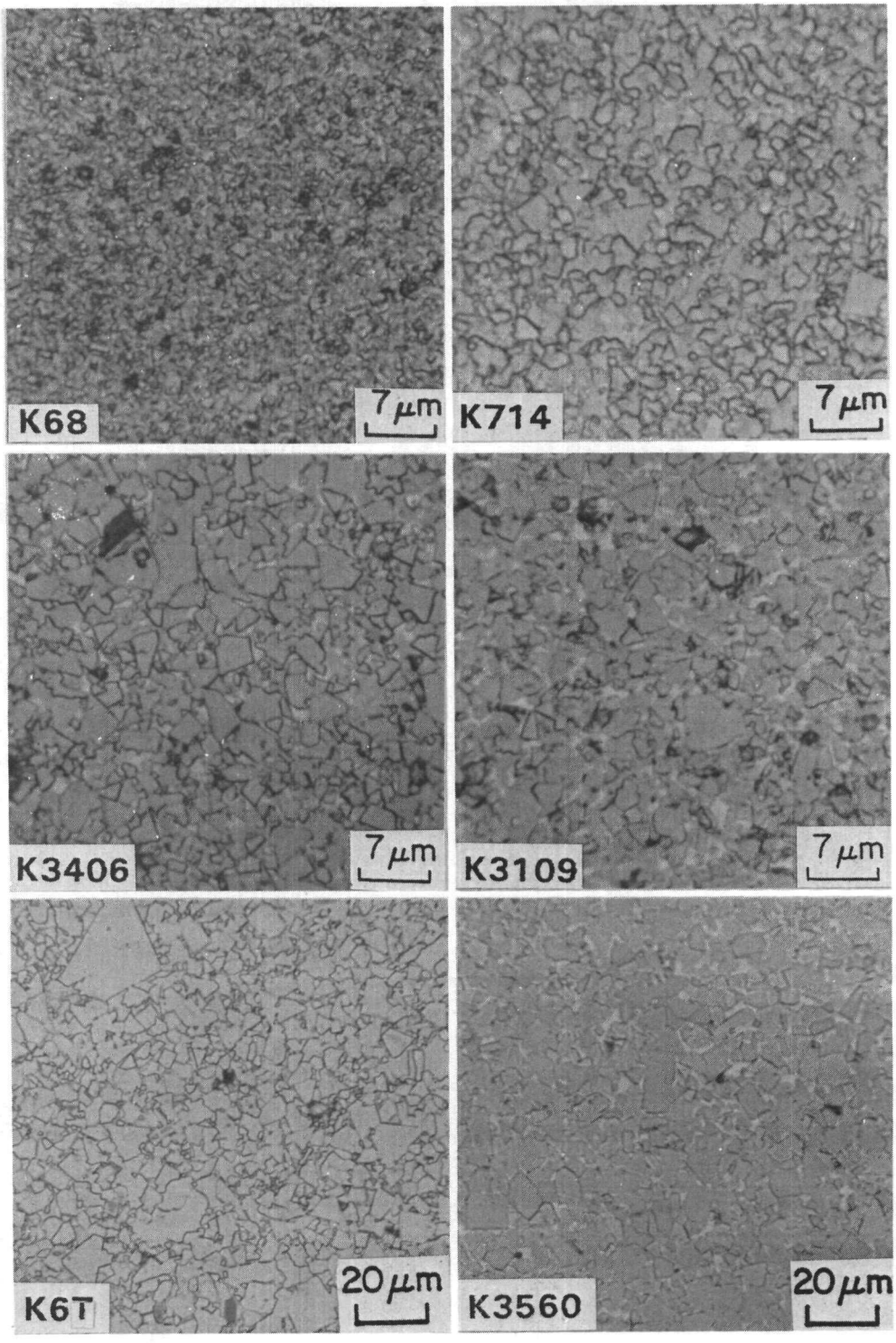

FIGURE 28. (Continued)

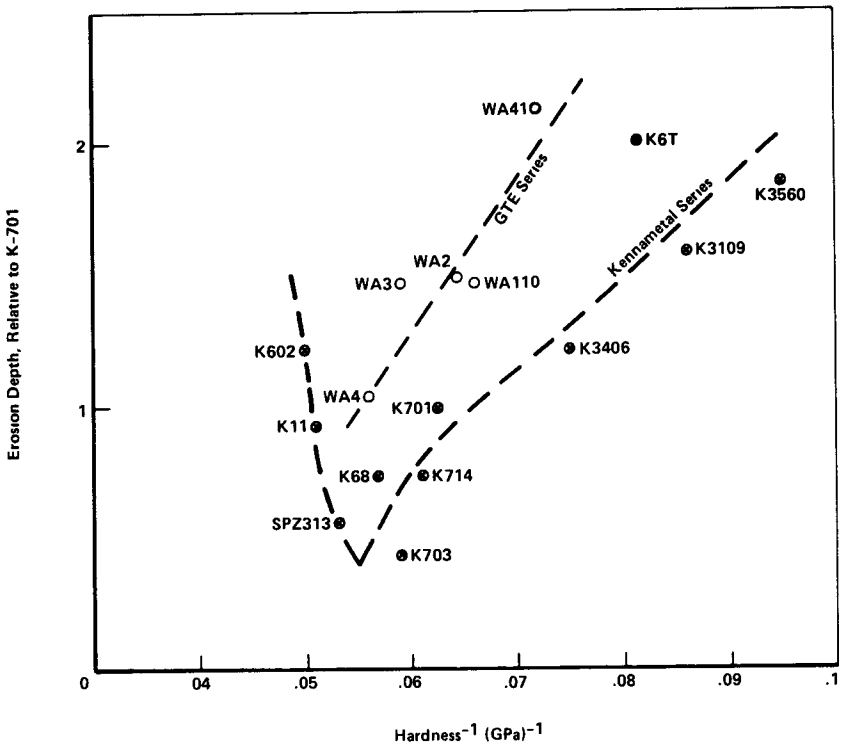

FIGURE 29. RELATIONSHIP OF EROSION DEPTH TO HARDNESS FOR TWO GROUPS OF WC-CERMETS

increase in erosion with further increase in hardness levels. Incomplete observations of the erosion craters suggested that materials with hardnesses higher than that corresponding to minimum erosion, eroded in a manner similar to hot-pressed ceramics, that is, via damage concentrated at particle edges and interfaces. The materials with lower hardness, which also tend to be those with increased binder levels, generally appeared to erode by modes which suggested ductile mechanisms.

This trend might be described as a transition in erosion behavior from one of ductile erosion involving deformation processes at high-binder levels to a brittle, intergranular erosion mechanism at low-binder levels. Such a trend of the erosion rates with the key mechanical properties of hardness and fracture toughness is consistent with some of the established theories of erosion. Finnie[8], for example, developed a model of erosion for targets responding in a ductile manner to impinging particles by equating the volume of the particle trajectory through the target to volume loss. The model envisaged a ductile cutting mechanism and the volume of the target material removed per impacting particle, ΔV, was given as[8]:

$$\Delta V = \frac{k \rho r^3 v_o^2 f(\theta)}{H} \qquad (1)$$

where k = a constant related to the contact geometry

ρ = particle density

r = particle size

v_o = particle velocity

$f(\theta)$ = a function of the impact angle, θ, with a maximum value at $\theta \simeq 15$-20 degrees.

H = hardness of the target.

Although Finnie developed his model specifically for single-phase ductile materials, it can be extended to two-phase alloys such as cemented carbides in two limiting situations. When the microstructural dimensions such as WC particle size ($\bar{d}$) and binder mean free path (λ) are small relative to the size of the impacting particle, the two-phase target is expected to respond

effectively like a single-phase target with the relevant mechanical property, i.e., hardness, of the two-phase microstructure. For WC-Co alloys Lee and Gurland[9] have suggested the following relation for indentation hardness of the aggregate:

$$H_c = H_{WC}\, V_{WC}C + H_m\, (1-V_{WC}C) \tag{2}$$

where

H_c = hardness of the WC-Co alloys

V_{WC} = volume fraction of WC

C = contiguity

H_{WC} = in situ hardness of WC particle in the alloy

H_m = in situ hardness of metal binder in the alloy.

The in situ hardnesses are related to the bulk hardnesses and microstructural variables through Petch-type relations[9]:

$$H_{WC} = H_{WCb} + A\bar{d}^{-1/2} \tag{3}$$

$$H_m = H_{mb} + B\lambda^{-1/2} \tag{4}$$

where

H_{WCb} = bulk hardness of WC

H_{mb} = bulk hardness of metal binder

A, B = characteristic constants.

The characteristic target hardness in Finnie's equation, Equation 1, would be the aggregate hardness, Equation 2, when the impinging particles are large relative to $\bar{d}$ and λ. On the other hand, when the particles are small relative to $\bar{d}$ and λ, the WC and metal binder phases would respond individually with erosion rates controlled by their in situ hardnesses (Equations 3 and 4). In either case, however, the predicted trend of erosion rates of the alloys with binder level is consistent with the behavior shown at low-hardness levels in Figure 29. Increasing the binder content decreases H_m through increase of λ (Equation 4) and also decreases H_C, through a decrease of both H_m and V_{WC}

(Equation 2). These effects of decreasing hardness increase the erosion rate as inferred from Equation 1.

Currently there are no theories that treat erosion of two-phase alloys by a brittle, intergranular failure mechanism. But it is safe to assume that fracture toughness, K_{Ic}, is a key material property that controls the erosion rate in this mechanism. The erosion rate is expected to increase with decreasing fracture toughness.

For cemented carbides, it has been shown that K_{Ic} is related to the effective yield strength of the binder ligaments, $_y$, and the binder mean free path, λ (10), by:

$$K_{Ic} = \left[\frac{\sigma_y \quad \lambda E}{\alpha (1-\nu^2)} \right]^{1/2} \tag{5}$$

where

E = Young's modulus

υ = Poisson's ratio

α = a constant.

The effective yield strength of the binder is assumed to be proportional to the in situ hardness of the binder (Equation 4), with a value of 1/3 for the proportionality factor. It is clear from Equations 4 and 5 that fracture toughness of cemented carbide alloys should increase monotonically with increasing binder mean free path, as is evident (see Figure 26). Since indentation hardness of the aggregate decreases with the binder mean free path, the trend of the erosion rate at high hardness levels, Figure 29, reflects the influence of fracture toughness.

III.2.2 Development of an Artificial Slurry for Standardized Erosion Testing

The constituents of the artificial slurry were selected such that their physical characteristics were typical of the constituents in a coal-derived slurry. Thus, mean size, size distribution, hardness, and elastic properties of the erodent and viscosity, and viscosity-temperature relations

for the slurry medium were desired to be typical of these properties in a coal-derived slurry. Energy-dispersive X-ray analysis (EDAX) of the undissolved solids separated from the coal slurries indicated a variety of compositions, but a preferential concentration of Si was noted in the majority of the particles.(3) SiO_2 was chosen as the substitute erodent, assuming that Si was present in the coal inorganic materials as SiO_2.

III.2.2.1 Characteristics of the Substitute Silica Erodent. The selected, substitute erodent was fused silica, grade GP 7I, obtained from Harbison-Walker Refractories. This is a 99.5 percent by weight, amorphous grade SiO_2, with Al_2O_3 as the major contaminant. The chemical composition, mean particle size, and specific surface area, as reported by the supplier, are given in Table 9. Figure 30 shows the silica particle shapes in the mean-size range. Particles are generally angular with sharp edges. Submicron particles appear to adhere to the larger particles.

The particle size distributions determined by two different techniques are shown in Figure 31. Circles in the figure indicate the size distribution determined by a centrifugal sedimentation technique (ASTM standard Test Method C 678-75). The median particle size is 6 μm and this agrees closely with the mean size reported by the supplier (Table 9). The second technique used to evaluate particle size distribution employed a Leeds-Northrup Laser Microtrac Analyzer. The size distributions obtained by this technique are indicated by the squares in Figure 31. The laser technique uses a dilute slurry of the particles in a colorless liquid medium. The size distribution obtained with water as the suspending medium is shown by the open squares, while the filled squares are for the artificial slurry diluted with 50 percent by volume of toluene. There is reasonable agreement between the distributions for the two media, with some differences apparent at small particle sizes. It is not clear whether this difference reflects intrinsic differences in the powder specimens sampled or is due to the differences in the suspending media. A much larger difference is noted between the size distributions obtained by the laser technique and that by the sedimentation technique. The median particle size by the laser technique is 14-17 μm. It

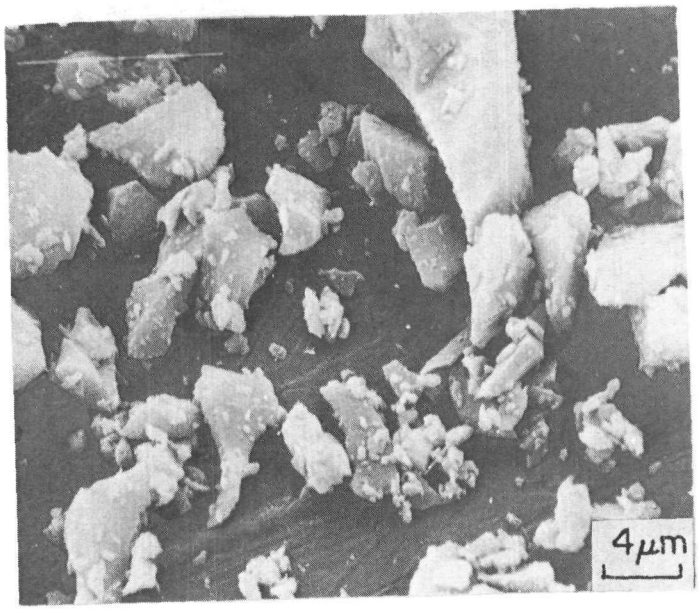

FIGURE 30. SCANNING ELECTRON MICROGRAPH OF FUSED SILICA POWDER, GRADE GP 71, OBTAINED FROM HARBISON-WALKER REFRACTORIES

TABLE 9. COMPOSITION, MEAN PARTICLE SIZE, AND SPECIFIC SURFACE AREA OF HARBISON-WALKER GRADE GP 7I FUSED SILICA POWDER

Composition	Percent
SiO_2	99.5
Al_2O_3	0.2
Fe_2O_3	0.05
Na_2O	0.004
K_2O	0.004
Mean particle size, microns	7
Specific surface area, m^2/gm	1.38

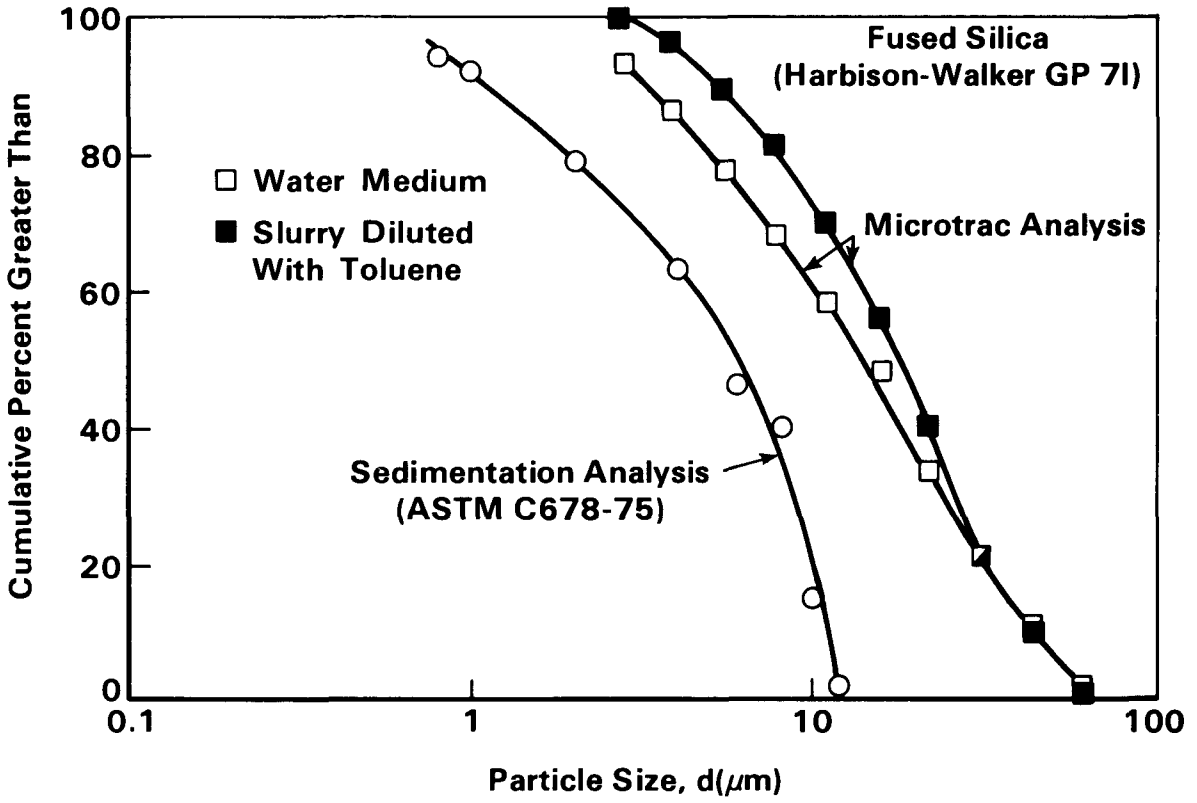

FIGURE 31. PARTICLE-SIZE DISTRIBUTION OF AS-RECEIVED HARBISON-WALKER GP-7I FUSED SILICA POWDER

is suggested that this difference could well be due to the intrinsic limitations of the two techniques. The sedimentation technique is generally accurate and limited to particle sizes less than 30 μm. Small fractions in the larger size range, 10-30 μm, can be missed in the analysis because of difficulties in determining sedimentation heights. The Microtrac Analyzer, on the other hand, is designed to analyze particle sizes greater than 2.8 μm. Very small particles are not detected by this technique. Based on these arguments it might be reasonable to assume that the median particle size is approximately 10 μm, a value in between the median values indicated by the two techniques.

III.2.2.2 Preparation of the Substitute Slurry. The Harbison-Walker fused silica powder, GP7I, served as a suitable substitute erodent. The size range of the silica powder, in spite of the uncertainties involved in the size distribution analyses, is well within the range of sizes noted for the insoluble particles from the coal-derived slurries.(3) A suitable liquid suspending medium was required to prepare the substitute slurry. The selection was guided by two considerations. The particle-carrying liquid medium should have viscosity and viscosity-temperature relations similar to those for the coal-derived slurries. Viscosity of the slurry has a significant influence on slurry erosion. It can influence the erosion rates directly by affecting the slurry-flow velocity through a letdown valve or a slurry-jet orifice in a jet impingement test rig operating under a set pressure drop. Also the viscosity influences the particle trajectories within a slurry stream and, thus, affects erosion rates through the particle impingement angle. Secondly, the selected liquid should be stable at the temperatures of interest, i.e., up to a maximum temperature of 350 C. An oxidation-resistant, petroleum-derived machine oil, Sohio grade Energol HL-32, met these requirements adequately. The low cost of this oil (approximately $2.50/gallon) was also a factor favoring its selection.

All of the substitute slurry erosion-test data discussed in this report were obtained on slurries prepared by suspending the Harbison-Walker, fused-silica powder in the Energol HL-32 oil.

III.2.2.3 Erosion Rates of the Substitute Slurry and the Coal-Derived Slurry - A Critical Comparison. Initial experiments with the substitute slurry were designed to examine its erosion characteristics, especially in relation to the erosion rates typically obtained in a coal-slurry erosion test. These experiments were conducted in the Battelle jet-impingement test rig with a slight modification. The closed-loop, slurry cycling system was modified to run jet-impingement tests with a continuous supply of fresh slurry. A large-capacity (20-gallon) slurry tank was connected to the original slurry chamber to maintain a constant supply of fresh slurry. This modification was introduced in the test procedure in order to avoid the complications that arise from slurry degradation from particle breakage or blunting that is inherent in the recycling system. All of the initial slurry-comparison tests were conducted on the same reference target material-cemented WC, Kennametal Grade K 701 (WC-10% Co-4% Cr).

Figure 32 shows a comparison of the variation of erosion depth, determined from a surface profilometer trace, as a function of test duration for the two types of slurries. The substitute slurry consisted of 8 weight percent silica powder in Energol oil. This weight fraction was selected to match the insoluble concentration in a coal-derived slurry that is typically obtained when 24 weight percent of the Wilsonville SRC product derived from Illinois No. 6 coal is dissolved in anthracene. This is the coal slurry that is typically used in all the material screening activities. A linear variation of the crater depth with test duration is observed for both the substitute slurry and the coal-derived slurry from the Wilsonville SRC product for a test duration up to 18 minutes. In this time range the substitute slurry erodes the cemented WC target at a rate 2.5 times the rate of erosion from the coal-derived slurry. This enhanced erosion rate could be due to any of a number of reasons. All of the 8 weight percent insoluble particles in the coal-derived slurry may not be as erosive as the fused-silica particles. It is known that some of these particles are undissolved coal particles which are expected to be less erosive because of their lower hardness, density, and probably rounded edges. Even among the inorganic particles in the coal slurry some are likely to be CaO, FeO, and other less erosive metal oxides.

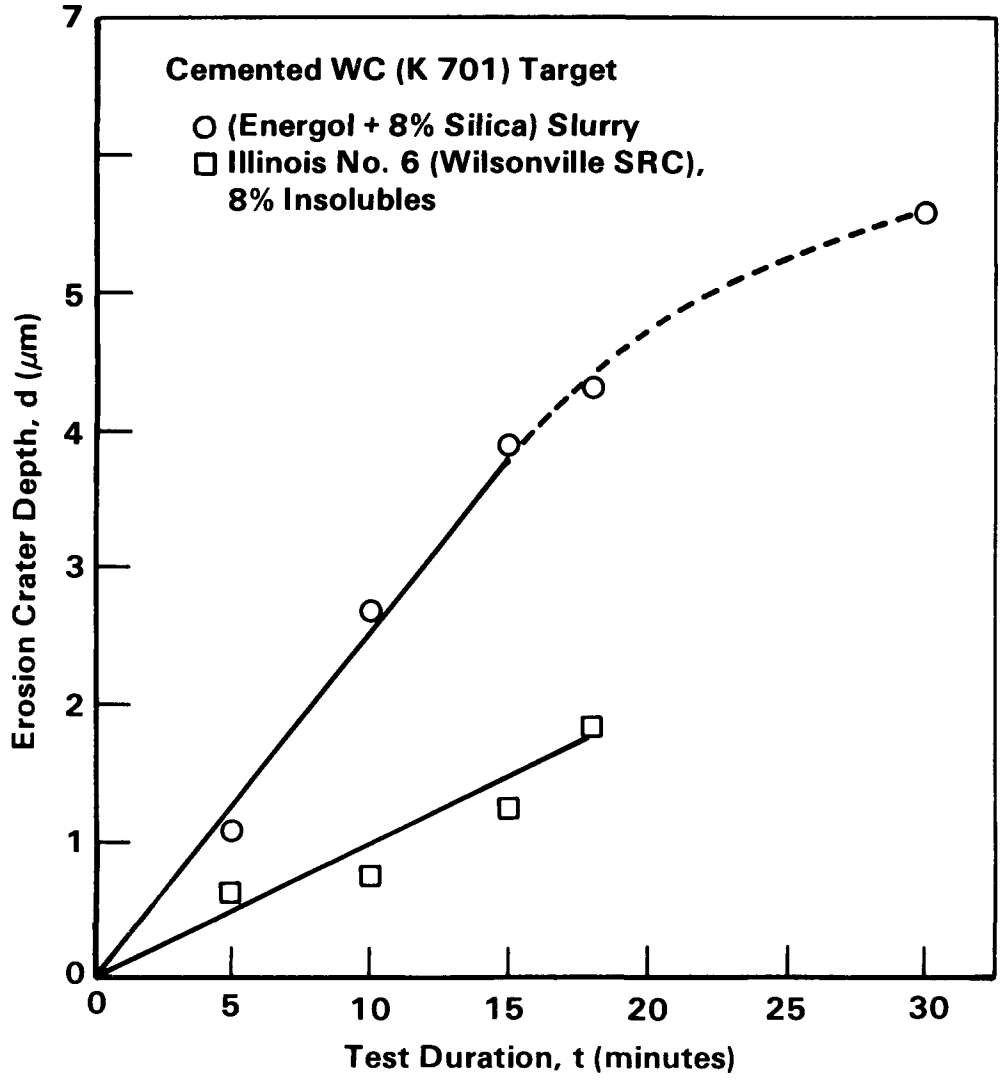

FIGURE 32. EROSION CRATER DEPTH AS A FUNCTION OF TEST DURATION IN JET IMPINGEMENT TESTS USING THE SUBSTITUTE SLURRY AND THE COAL-DERIVED SLURRY. JET VELOCITY = 145 m/second IMPINGEMENT ANGLE = 20°

The substitute slurry test conducted for a period of 30 minutes shows an indication of a deviation from the linear relation observed at shorter intervals. It is not clear whether this deviation is a true reflection of the development of the crater morphology or simply a statistical deviation. If the crater depth does indeed increase nonlinearly with decreasing rates, it can be argued that it may be related to the decrease of the effective angle of attack of the particles as the crater profile develops. Results presented in the next section, however, suggest that crater depths do vary linearly for periods of up to at least 45 minutes. The deviation observed in Figure 32 appears to be a statistical scatter.

III.2.2.4 Aging Characterisitics of the Slurries. It is known from experiments with the coal-derived slurries[3] that repeated use of the same slurry reduces its erosivity, which probably indicates either a reduction of the insoluble particle sizes (erosion rate is typically α (particle size)$^{\eta}$ where η is a positive exponent) through breakdown or blunting of the sharp corners of the particles. The modified, once-through slurry flow system was used to examine the characteristics of this "aging" of both the substitute and the coal-derived slurries. The 20-gallon reservoir of slurry typically lasted 45 minutes in a jet test at a nominal slurry velocity of 145 m/second. Following completion of this 45-minute test, the slurry was returned to the reservoir chamber and a new test was commenced with the once-used slurry. This procedure was repeated a number of times and in each cycle the erosion rates on the standard cemented WC reference material were established.

Figure 33 shows the aging effect of the two slurries. The erosion rates, expressed as crater depths (μm) normalized to 1-hour test duration, are plotted versus the number of slurry iterations, i.e., number of repetitive uses of the same slurry. The erosion rates decreased systematically with the number of slurry iterations for both the slurries. As before, the substitute slurry was more erosive than the coal-derived slurry. The coal slurry appeared to lose its erosivity completely after about 6 iterations. The substitute slurry showed some indications of a saturation, i.e., erosion rates decreased at decreasing rates. It should also be noted that the erosion rates

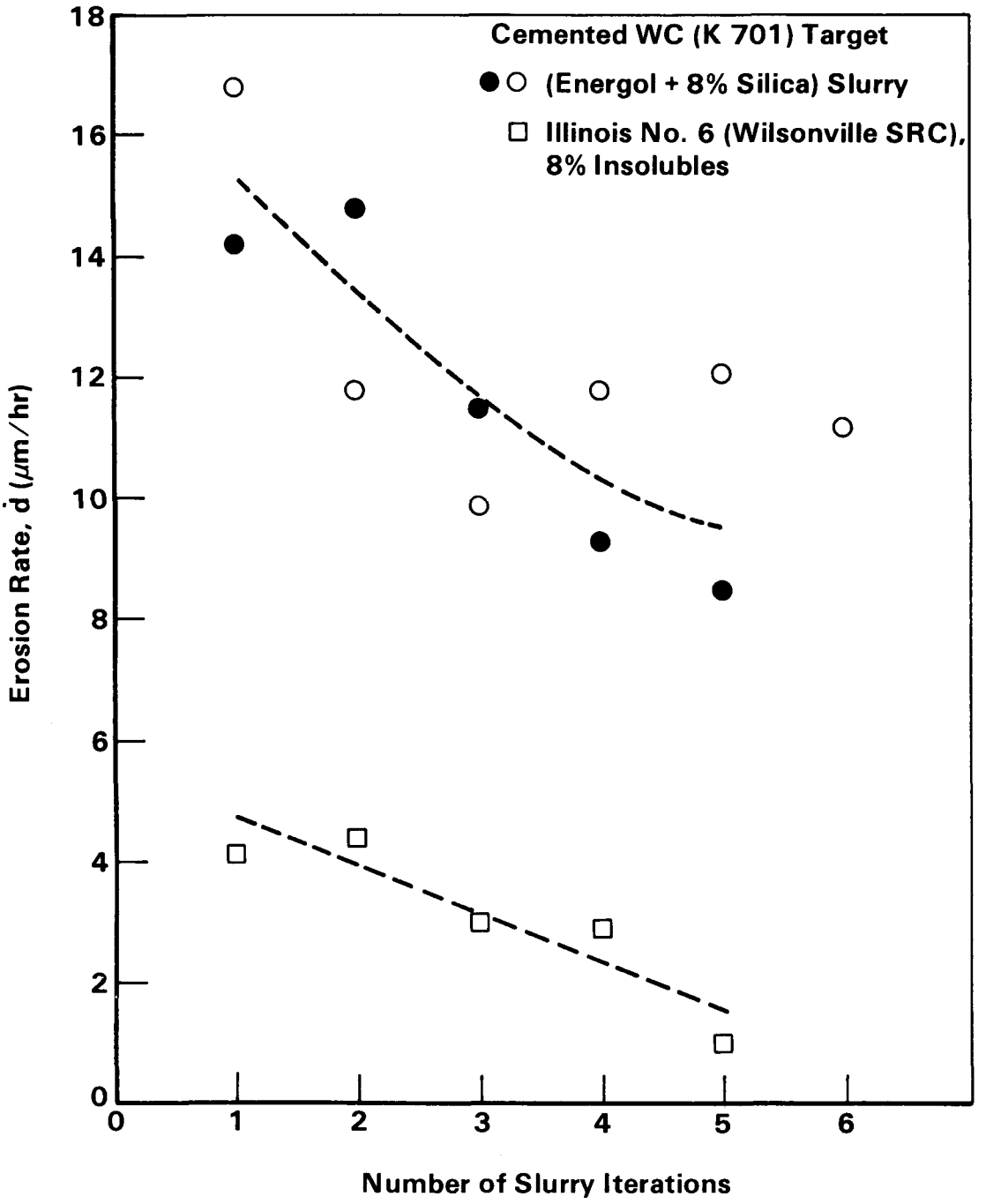

FIGURE 33. AGING EFFECTS OF SLURRIES AS INDICATED BY THE DECREASE OF EROSION RATES WITH NUMBER OF ITERATIONS OF SLURRY USE. JET VELOCITY = 145 m/s. JET IMPINGEMENT ANGLE = 20°

for the substitute slurry, when extrapolated back to zero iteration, i.e., fresh slurry, indicated an erosion rate of 15-18 μm/hour. This would approximately be the erosion depth expected if the linear relations of Figure 32 were extrapolated to 1 hour. The data for the substitute slurry include two separate series. There is significant scatter in the data which is attributed primarily to fluctuations in velocity caused either by fluctuations in the pressure head or the temperature.

To determine the cause of aging, samples of slurries were taken after each test iteration and the insolubles in the slurries were examined for size distribution using the Laser Microtrac Analyzer. The test slurries were diluted with 50 percent by volume of toluene before they were used for particle-size analysis. Figure 34 shows the particle size analysis for the silica-Energol synthetic slurry. The circles and the squares correspond to fresh slurry and a slurry subjected to six test iterations. Only a moderate decrease in particle size with repeated slurry use was noted and most of this decrease appeared in the large size regime as might be expected. Although this moderate decrease in particle size might have contributed to slurry-aging, the decrease in erosion rates observed in Figure 33 appears to be too large to be solely accounted for by the particle size change. A logical conclusion might be that particle blunting might be a contributing process in the phenomenon of slurry aging.

Triangles in Figure 34 show the size distribution of fresh (unused) silica powder dispersed in pyridine. There is a significant difference between this size distribution and that determined with the 50 percent Energol - 50 percent toluene slurry mixture (circles in Figure 34). It is not clear whether this difference reflects sensitivity of the technique to the suspending medium or it is a genuine indication of the size distributions as influenced by the different tendencies of the particles to agglomerate in different liquid media. Note that the median particle size using pyridine is around 10 μm, which agrees with the conclusions of Section III.2.2.1.

III.2.2.5 Slurry Recycling and Influence of Periodic Rejuvenation. The once-through slurry flow test procedure is intrinsically superior to the

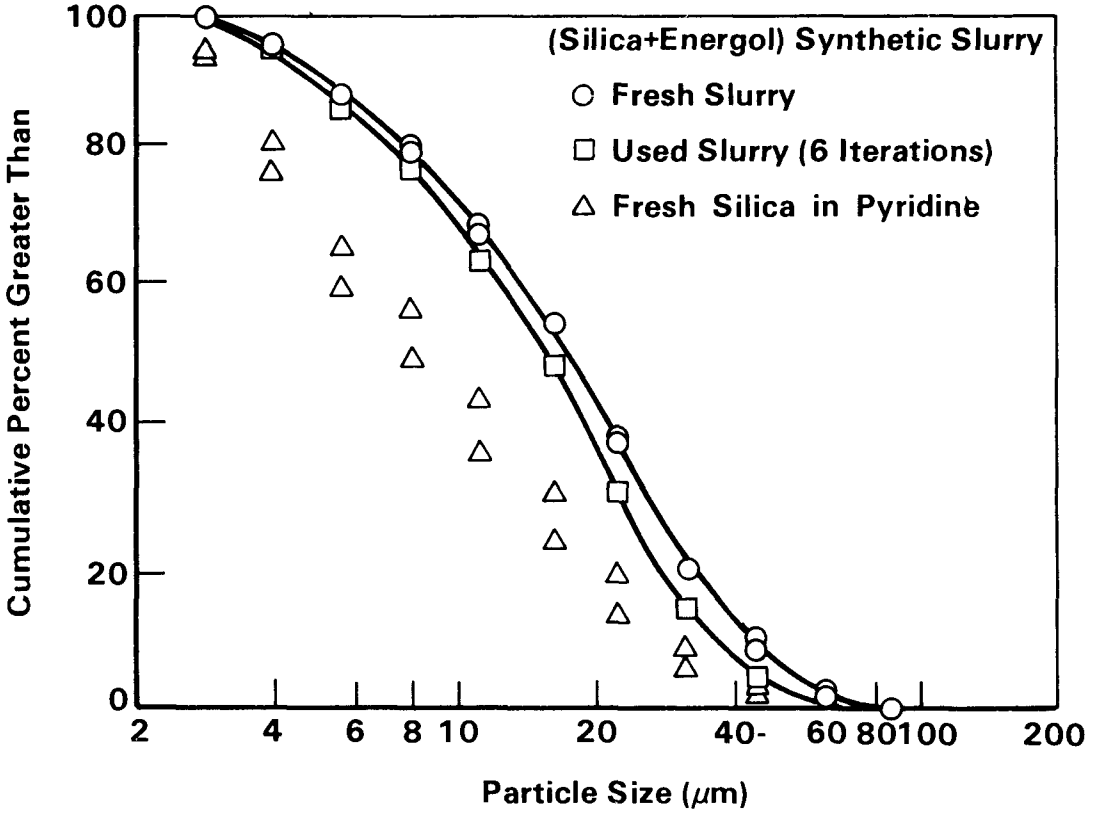

FIGURE 34. SILICA PARTICLE SIZE DISTRIBUTION IN THE SYNTHETIC SUBSTITUTE SLURRY DETERMINED BY THE LASER-MICROTRAC TECHNIQUE

slurry recycling test procedure since it avoids the time-dependent degradation characteristics of the slurry. But, it is also expensive and involves the handling of large volumes of slurry. To avoid these complications, the routine screening tests with the reconstituted coal slurry were usually conducted in the cyclic loop system where about 2 gallons of the slurry were continuously cycled between the slurry chamber and the test chamber. A procedure that involves substituting 25 percent by weight of the coal slurry after every three, 1-hour material screening tests has been used in the coal slurry screening tests.(3) With this rejuvenation procedure, the erosion rates do decrease with time, but periodic partial substitution of the used slurry with fresh slurry rejuvenate the test slurry and produce erosion rates that are nearly constant after two cycles of slurry additions. This is taken as an indication of a stabilization of the slurry condition.

The effect of periodic slurry substitutions on erosion rates was examined for the substitute slurry. Results are summarized in Figure 35. The behavior of the substitute slurry and the coal slurry in the continuously cycling tests were significantly different. Specifically, for the substitute slurry the periodic substitution of 25 percent volume of fresh slurry did not restore the erosion rates, and the slurry continued to show signs of aging, i.e., decreasing erosion rates with time. Reasons for this different behavior of the substitute slurry are not yet clear. Because of the high rate of deterioration of the substitute slurry in the recycling mode, all subsequent tests were conducted in the once-through mode.

III.2.2.6 Material Screening With the Substitute Slurry. As a final qualification of the substitute slurry, it was used in screening tests for ranking a number of advanced ceramics in terms of their erosion rates relative to the reference standard cemented carbide (K 701). The ranking obtained with the substitute slurry was compared with that obtained in the conventional screening tests which used the coal-derived slurry. The screening tests with the substitue slurry were conducted with a silica-loading of 8 percent by weight, a nominal slurry velocity of 145 m/s, slurry-impingement angle of 90 degrees and a test duration of 5 min. The 90-degree impingement

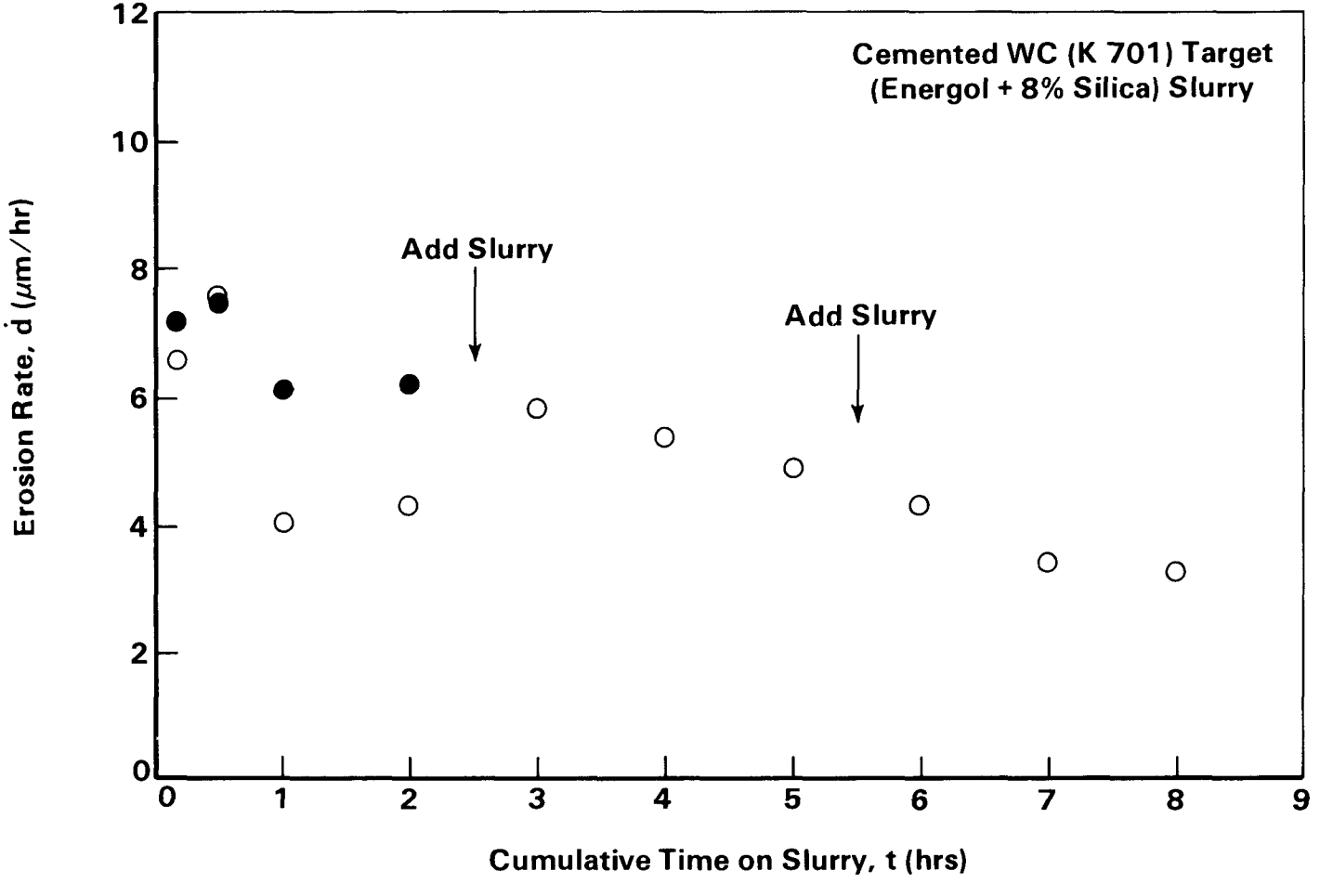

FIGURE 35. EFFECT OF PERIODIC SLURRY ADDITIONS ON THE EROSION RATES. SUBSTITUTE SLURRY. SLURRY VELOCITY = 145 m/second. IMPINGEMENT ANGLE = 20° (OPEN AND CLOSED SYMBOLS REPRESENT DIFFERENT RUNS)

angle and the high velocity were used in order to obtain measurable erosion depths in the short duration tests. The duration of each test was limited because of the limitation of the total volume of slurry available for a given series of tests in the once-through test mode. The screening tests with the coal-derived slurry employed the Wilsonville SRC product, 24 percent by weight, dissolved in anthracene oil to give nominally the same insoluble concentration as the substitute slurry. These tests were conducted in the recycling mode with 145 m/s nominal slurry velocity, 20 degrees slurry-jet impingement angle, and 1-hour test duration.

The test materials selected for the comparative screening, and their mechanical properties, are listed in Table 10. All of the Young's moduli and some of the hardness and fracture toughness values were reported by the manufacturers or they were taken from the literature. The fracture toughness values evaluated in this program were measured by an indentation technique that is described in detail in Appendix A. These measured values are listed in Table 10 with their standard errors. The measured hardness values were obtained with a diamond pyramid indenter at a fixed load of 2500 gms. There was no significant variation in fracture toughness among the polycrystalline ceramics. Cemented WC and soda-lime glass provided the upper and lower limits of the fracture toughness range investigated, while the hardness limits were obtained with B_4C and the soda-lime glass, respectively.

Ranking of the target materials evaluated in the Battelle slurry-jet impingement test is normally based on the maximum depth of the craters produced on the target surfaces. Maximum depth is an adequate parameter to compare the relative erosion rates of most of the target materials since the erosion craters produced in the different materials are similar in shape and surface extension so that the maximum crater depth is directly proportional to the volume of the crater. Some target materials, however, do not erode uniformly over their microstructure and may show localized crater depth variations due to local variations in the erosion response of the microstructure. This is particularly true in materials that erode more severely near the grain boundaries because of the presence of softer phases or grain-boundary porosity. In these materials, the use of the maximum crater depth to

TABLE 10. PROPERTIES OF TARGET MATERIALS USED IN COMPARATIVE EROSION SCREENING*

Material	Source (Grade)	Young's Modulus (GPa)	Hardness** (GPa)	Fracture Toughness† ($MPam^{1/2}$)
Cemented WC	Kennametal (K 701)	533	16.2 ± 0.7	7.8 ± 2.4
α-SiC I	Carborundum	406	26.1 ± 1.34	4.7
α-SiC II	Carborundum	406		4.7
B_4C-I (HP)	Norton (Norbide)	448	30, 31	
B_4C-II (HP)	Norton (Norbide)	448		
Al_2O_3 (HP)	AVCO (Hot-pressed)	413	17.7 ± 0.44	2.7 ± 0.3 (4.19)
SiC (HP)	Norton (NC-203)	440		4.0
Si_3N_4 (HP)	Norton (NC-132)	310	17.5 ± 0.3	4.14 ± 0.2
S.L. Glass	PPG. Ind. (Float Glass)	72	5.2 ± 0.08	0.75

* Young's moduli and hardness and fracture toughness values listed without the standard errors were reported by the manufacturers or they were obtained from the literature on identical grades.

** Vickers diamond pyramid hardness at 2500 gms indent load.

† Fracture toughness values with standard errors were measured by the indentation technique (see Appendix A).

characterize erosion response underestimates their bulk erosion resistance. To account for these local fluctuations in erosion response and derive a bulk average response, an average crater depth was defined by area averaging the crater profile over a fixed crater width (800 μm in the 90 degrees impingement test). This procedure could not be applied to the coal-slurry screening test results because the crater shape was asymmetric and the crater base width was ill-defined because of the small impingement angle (20 degrees).

Tables 11 and 12 summarize the comparative erosion rates for the reference cemented carbide and a number of ceramics evaluated with the substitute slurry and the coal-derived slurry, respectively. Some general trends in the relative erosion behavior of the materials were apparent in both types of screening tests. Thus, for example, the hot-pressed grades of SiC (NC-203) and Si_3N_4 (NC-132) showed significantly greater susceptibility to erosion while the sintered SiC (α grade) and the hot-pressed B_4C (Norbide) showed superior wear resistance relative to the cemented carbide (K 701) in both the slurry tests. The relative ranking of the test materials based on their erosion susceptibilities was nearly the same in the two test series. The sintered SiC, however, showed marked superiority with respect to both the cemented carbide and the sintered B_4C in the coal-slurry tests, while its performance in the synthetic slurry test was comparable to the B_4C.

Table 11 also indicates that average crater depths for some of the target materials were significantly less than the maximum crater depths. This was particularly the case with α-SiC-I for which the maximum crater depth and the average crater depth differed by factor of seven. The calculation of the average crater depth demonstrates the superior bulk erosion resistance of this material, while based on the maximum crater depth the material would be ranked inferior to several other candidate materials. Similar microstructural inhomogeneities in erosion rates were observed to a lesser extent in the sintered B_4C and the hot-pressed Al_2O_3. The soda-lime glass was an exception to the rule in that the calculated average crater depth was greater than the maximum crater depth. This apparent anomaly resulted from the fact that the

TABLE 11. COMPARATIVE EROSION DATA FOR REFERENCE CEMENTED CARBIDE (KENNAMETAL K 701) AND CERAMICS EVALUATED IN SUBSTITUTE SLURRY JET IMPINGEMENT TESTS[a]

Material	Grade	Source	Composition	Maximum Crater Depth d_{max}, μm	Average Crater Depth d_{avg}, μm
Cemented WC	K 701	Kennametal	WC + 10% Co + 4% Cr	3.0 4.8	1.9 4.0
Sintered SiC	-SiC-I	Carborundum	SiC	7.6	1.1
Sintered SiC	-SiC-II	Carborundum	SiC	4.0	1.8
Hot-pressed B_4C	Norbide-I	Norton	B_4C	3.0	1.1
Hot-pressed B_4C	Norbide-II	Norton	B_4C	3.6	1.0
Hot-pressed Al_2O_3	--	Avco	Al_2O_3	7.4	2.8
Hot-pressed Si_3N_4	NC-132	Norton	Si_3N_4	26.7	12.1
Hot-pressed SiC	NC-203	Norton	SiC	39.4	25.8
Hot-pressed SiC	NC-203	Norton	SiC	61.0	46.7
Soda-Lime glass	Glass	PPG, Ind.	73% SiO_2, 14% Na_2O, 9% CaO	1320	1364

(a) Test slurry: (Energol + 8 percent weight Silica).
Slurry temperature = 250 C,
Slurry jet velocity = 145 m/second,
Impingement angle = 90 degrees,
Test duration = 5 minutes,
Once-through slurry tests.

TABLE 12. COMPARATIVE EROSION DATA FOR REFERENCE CEMENTED CARBIDE (KENNAMETAL K 701) AND CERAMICS EVALUATED IN COAL-SLURRY JET IMPINGEMENT TESTS*

Material	Grade	Source	Composition	Maximum Crater Depth d_{max}, μm
Cemented WC	K 701	Kennametal	WC + 10% Co + 4% Cr	5.4
Sintered SiC	-SiC-I	Carborundum	SiC	0.6
Sintered SiC	-SiC-II	Carborundum	SiC	
Hot-pressed B_4C	Norbide-I	Norton	B_4C	3.8
Hot-pressed B_4C	Norbide-II	Norton	B_4C	2.8
Al_2O_3 (HP)	Hot-pressed	AVCO	Al_2O_3	
Si_3N_4 (HP)	NC-132	Norton	Si_3N_4	
SiC (HP)	NC-203	Norton	SiC	28
Soda-lime glass	Float glass	PPG, Ind.	73% SiO_2, 14% Na_2O, 9% CaO	

* Test slurry: 24 wt. % Wilsonville SRC in anthracene oil.
Slurry temperature = 343 C,
Slurry jet velocity = 145 m/second,
Impingement angle = 20 degrees,
Test duration = 1 hour,
Recycling test system.

surface extension of the crater for soda-lime glass was much greater than 800 μm, the nominal constant crater width used to calculate average crater depths.

III.2.3 Characterization of Erosion Behavior of Selected Target Materials Tested with the Artificial Slurry

The characteristics of erosion of selected target materials, slurry-jet impact tested with the silica-Energol slurry, were evaluated by examining the eroded target surfaces in a scanning electron microscope and assessing the material removal mechanisms, especially as they relate to the material microstructure.

In the following sections the microstructure and scanning electron micrographs of the eroded surfaces are presented for some selected target materials. The target surfaces were metallographically polished prior to subjecting them to a slurry-jet test at 145 m/s nominal slurry velocity, 90 degrees impingement angle, and 250 C temperature. The slurry used in the tests had a silica concentration of 8 percent by weight. The tests were run usually for a period of 5 minutes.

Cemented WC (Kennametal Grade K 701)

Kennamental K 701 is a grade of cemented carbide with 10% Co - 4% Cr binder and WC particles that range in size up to 2 μm. Figure 36 shows the microstructure of the K 701 grade material. Figure 36(a) is a scanning electron micrograph of an as-polished surface, while Figure 36(b) shows an electron replica of the polished and etched surface. The replica micrograph reveals jagged WC particle boundaries. This could be due to the presence of Cr in the binder and its affinity for carbon, resulting in a reactive bond at the interface.

Figure 37 shows the eroded surface on a target of the cemented WC (K 701) following a slurry-jet impingement test with the substitute slurry. The low-magnification (75X) scanning electron micrograph (Figure 37a) shows a

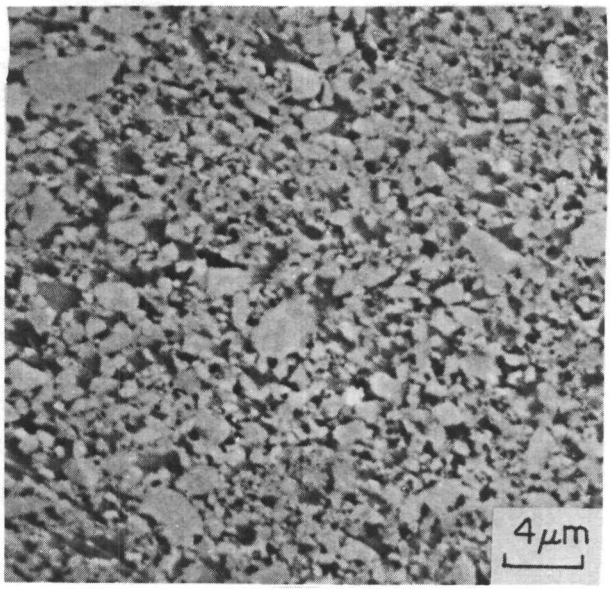

(a)

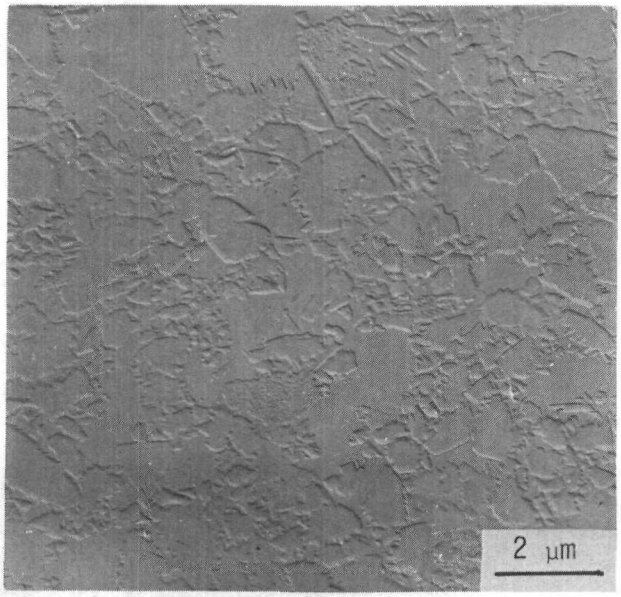

(b)

FIGURE 36. MICROSTRUCTURE OF K 701 (WC-10%Co-4%Cr)
(a) As Polished, (SEM)
(b) Surface Replica (TEM)

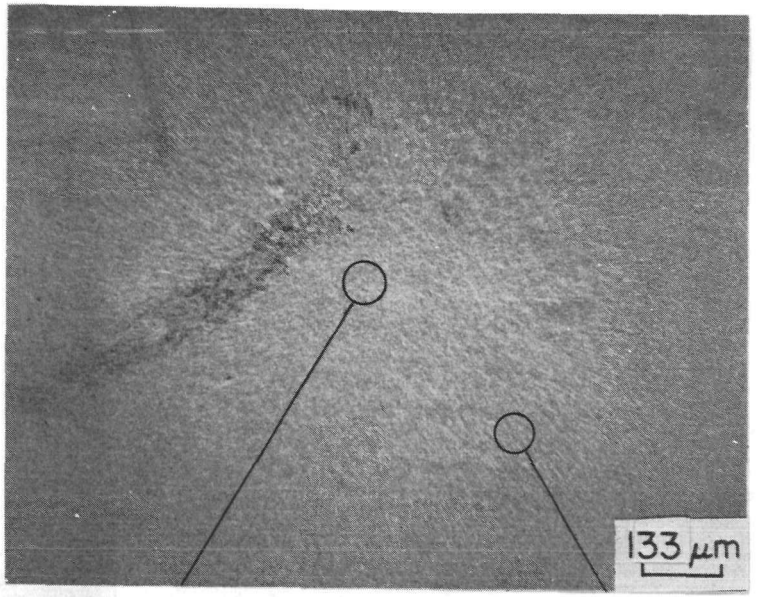

(a)

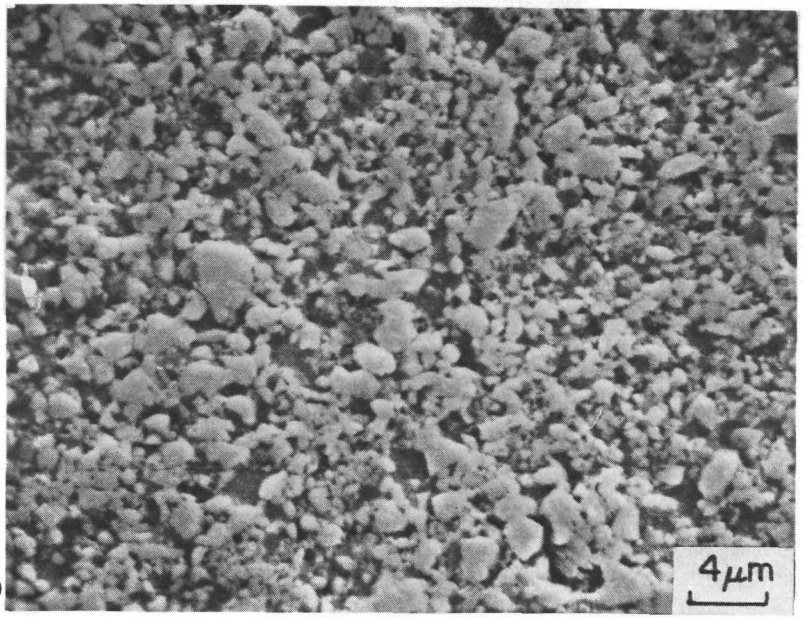

(b)

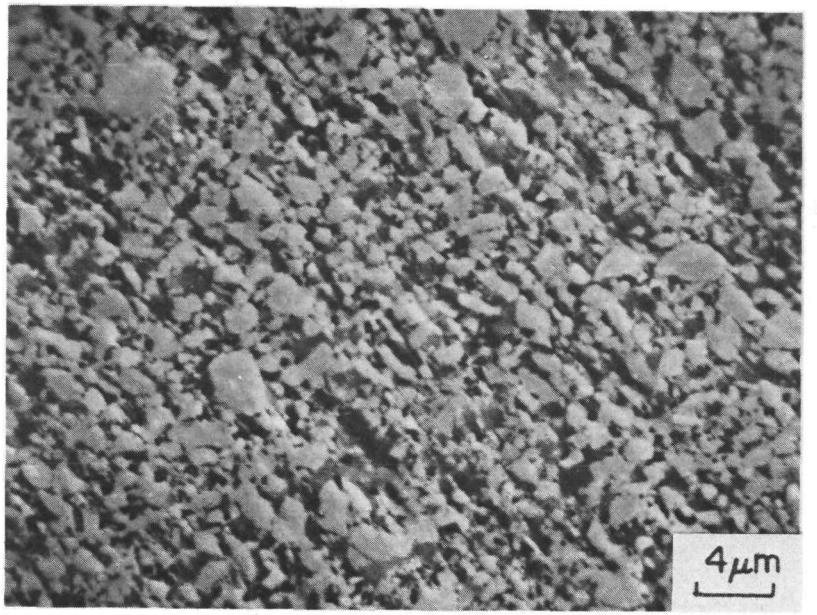

(c)

FIGURE 37. ERODED SURFACE ON CEMENTED WC (KENNAMETAL GRADE K 701)

(a) Test crater, (b) Eroded surface structure in the crater, (c) Eroded surface structure at the crater periphery

crater with characteristic features resulting from the axisymmetric flow pattern of the jet impinging at normal incidence to the target surface. In the center of the crater surface is a circular region that does not exhibit any of the radial flow features that are apparent in the outer regions of the crater. This region of the crater surface presumably corresponds to the stagnant zone that develops at the center of the impact area. Figure 37b and 37c show the eroded surface structure at higher magnification (2500X) in the center of the crater and in the outer periphery, respectively. Both surfaces show protruding WC particles with the surrounding binder preferentially removed by the slurry. The WC particles exhibit some wear resulting in rounded edges. The two eroded surfaces are different in one respect. In the center of the crater the binder is removed homogeneously without directionality. This is probably due to the fact that SiO_2 particles in the slurry impacted at near normal impingement in the center zone. In the outer periphery the eroded surface exhibits a characteristic radial wear pattern due to the preferential removal of the binder in the radial flow direction of the slurry fluid and the SiO_2 particles. No evidence of WC particle cracking or carbide carbide interface cracking was noted even at high magnifications.

Sintered SiC (Carborundum α-SiC)

The microstructure of sintered α-SiC is shown in the optical micrographs of Figure 38. Figures 38a and 38b indicate the microstructures of the same nominal material but are from specimens of two different lots. The microstructure exhibits elongated grains and some tendency for exaggerated grain growth. The latter feature is particularly evident in the α-SiC-II specimen. The elongated grains are, however, randomly oriented in a interlocking network.

Figure 39 shows the eroded surface on the α-SiC-I target following a slurry jet impingement test with the silica-Energol slurry. The macroscopic characteristics of the crater are similar to those of the K 701 target. These include the radial wear pattern along the outer edges of the crater and uniform, nondirectional wear in the crater center. Figures 39b, 39c, and 39d

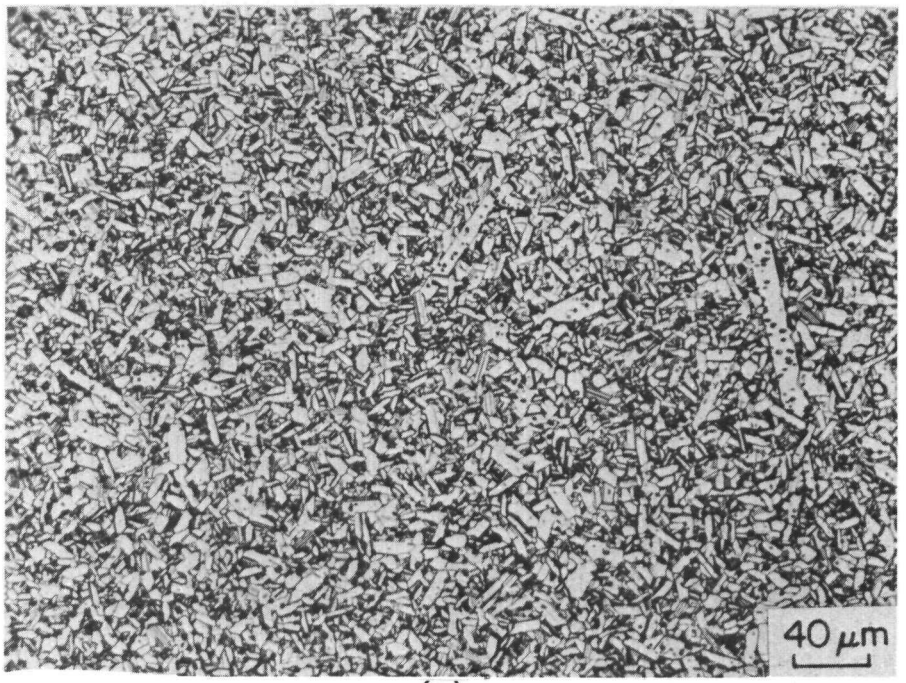

(a)

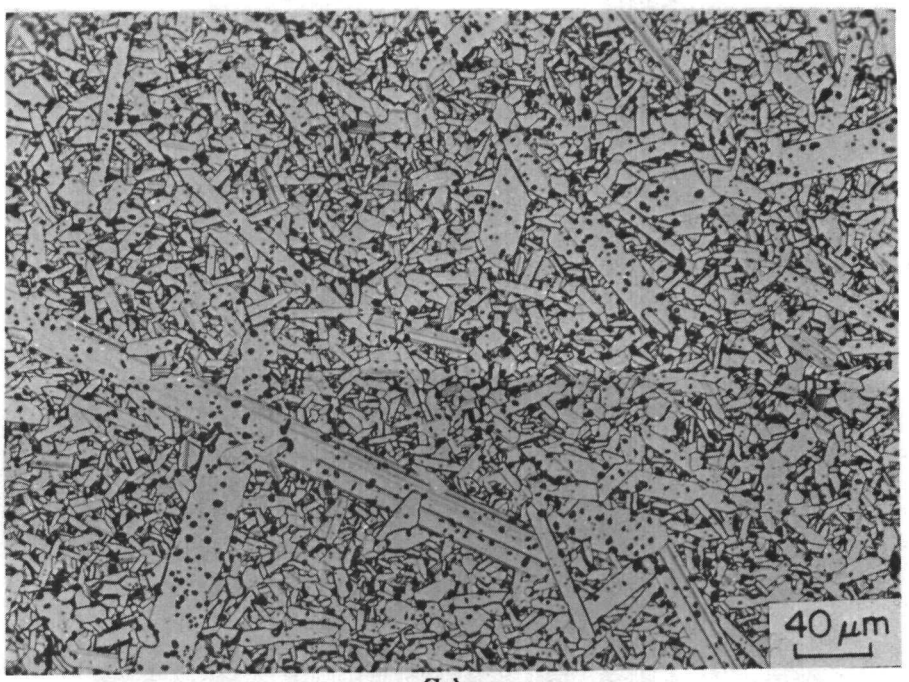

(b)

FIGURE 38. MICROSTRUCTURE OF SINTERED α-SiC

(a) Microstructure of α-SiC - I (ETCHED)
(b) Microstructure of α-SiC - II (ETCHED)

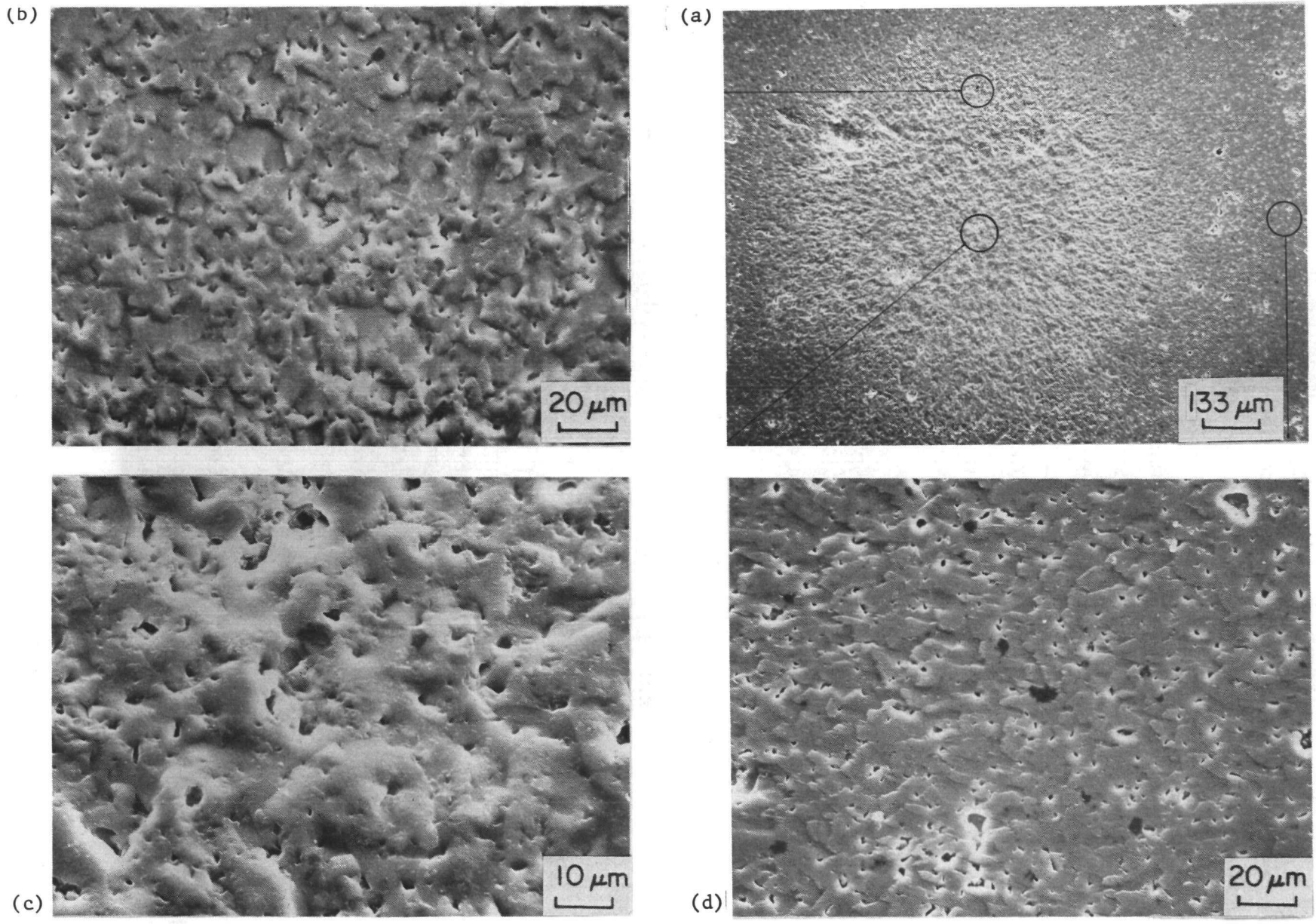

FIGURE 39. ERODED SURFACE ON α-SiC - I

(a) Wear Crater on Target Surface, (b) Periphery of the Crater, (c) Center of Crater,

show higher magnification micrographs of the crater center, crater periphery, and a remote, as-polished surface. In the crater center, sintered SiC exhibits uniform intragranular wear and the eroded surface appears generally smooth. There is no evidence of chipping or other modes of brittle cracking. The individual damage sites from SiO_2 particle impact could not be identified, perhaps due to the extremely small scale of the contact area. The bulk erosion characteristics of the sintered SiC were consistent with its superior erosive wear resistance. The periphery of the craters (Figure 39c) showed a slightly different mode of wear. In the periphery the target surface exhibited grain facets, which showed a radial directionality. SiC grains are known to exhibit anisotropic wear and this was clearly evident in a reaction-bonded SiC material that was evaluated in the earlier program.(11)

The erosive wear characteristics of the α-SiC-II specimen were very similar to those of α-SiC-I specimen in all respects except one. The large grains in the α-SiC-II specimen showed enhanced wear susceptibility on certain grain faces. This is clearly seen in Figures 40a and 40b which show test craters on the material resulting from 10-minute tests. The preferentially eroded, elongated regions of the target surface, indicated by the arrows, correspond to grain faces of two of the large grains in the vicinity of the craters. It is interesting to note that only some of the elongated grains in the crater vicinity show this tendency of enhanced erosion. This is probably related to the orientations of the grains. A particular crystallographic plane is likely to be more susceptible to erosion, so that whenever this plane is parallel to the target surface, the particular grain undergoes enhanced erosion. Miyoshi and Buckley(12) have also observed anisotropic tribological properties, coefficient of friction, microhardness and adhesive and abrasive wear resistance, in single crystals of SiC. The observations on the α-SiC-II specimen are also similar to the faceting observed on the SiC grains in the reaction-bonded grade.(11)

Figure 40c is a higher magnification micrograph showing the preferentially eroded SiC grain of Figure 40b. The grain surface shows intragrain porosity and surface features that appear to be tracks produced by the

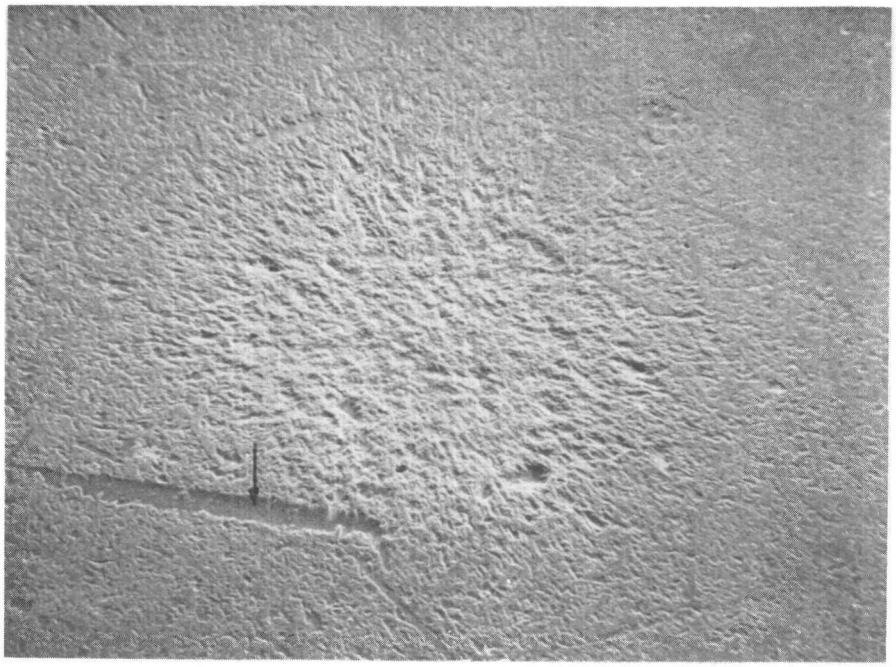

(a)

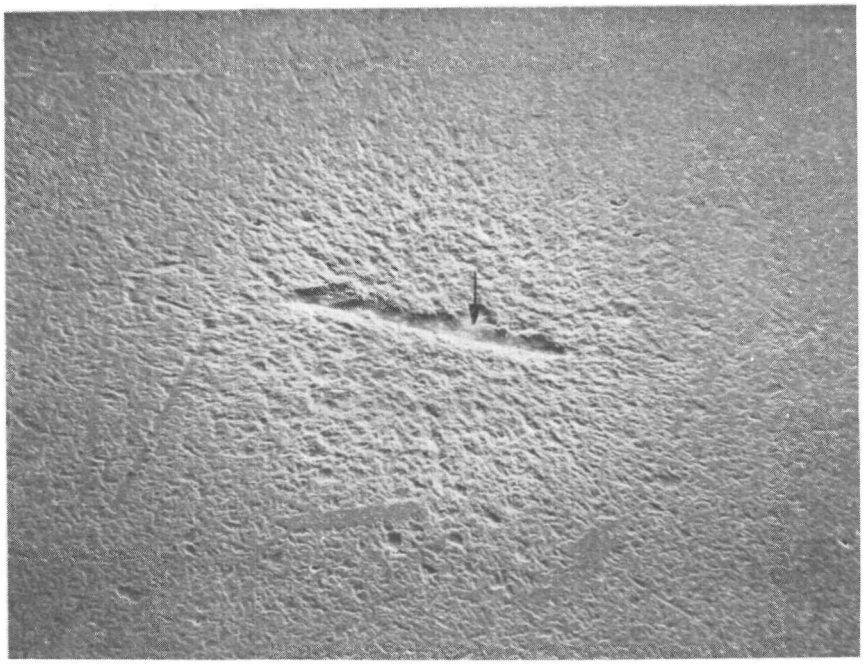

(b)

FIGURE 40. SLURRY EROSION TEST CRATERS ON α-SiC - II TARGET SURFACE (a and b)

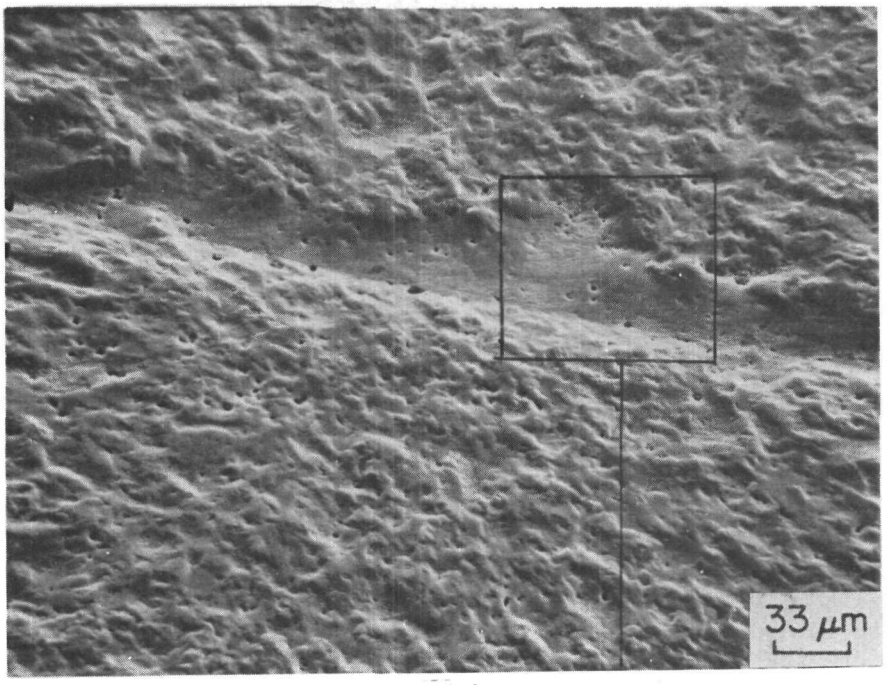

(c)

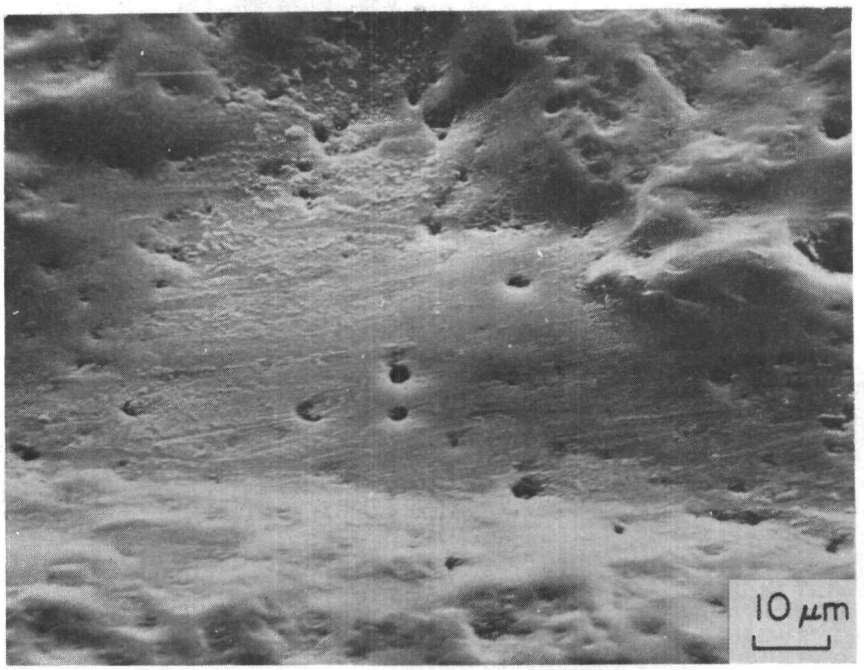

(d)

FIGURE 40. (continued) ERODED SURFACE ON A LARGE GRAIN OF α-SiC

impinging SiO_2 particles. The exact mechanism of material removal could not be identified, however.

Hot-pressed B_4C (Norton Norbide)

Test specimens from two different lots of hot-pressed B_4C were evaluated in the slurry jet test. Figures 41 and 42 show the polished (a) and etched surfaces (b) of the specimens designated B_4C-I and B_4C-II, respectively. The hot-pressed B_4C had a uniform, equiaxed grain structure with the B_4C-I specimen having a slightly larger average grain size, compared to the B_4C-II specimen. Both the specimens in the as-polished and etched surfaces showed what appeared to be grain-boundary pores. A fracture surface of the B_4C-II material, shown in Figure 43, indicated, however, that the material was fully dense. From these observations it was concluded that the pore-like features noted on the polished as well as on the etched surfaces were probably areas where a grain-boundary phase had been pulled out. The fracture surface also showed the presence of this grain-boundary phase, indicated by arrows in Figure 43. Energy-dispersive X-ray microanalysis of this grain-boundary phase did not reveal any heavy elements (those with atomic weights greater than for Neon). It was concluded on the basis of these results, and also from discussions with the manufacturer, that the grain-boundary phase was a carbon-rich nonstoichiometric boron carbide.[13] The pullout of this phase even during fine polishing suggested that it was much softer than stoichiometric B_4C.

Figure 44 shows the erosion crater on the target of B_4C-I (Figure 44a) and higher-magnification micrographs of the eroded surfaces near the crater center (Figure 44b) and crater periphery (Figure 44c) and an uneroded as-polished surface away from the crater (Figure 44d). It is clear from the structure of the eroded surface that the carbon-rich nonstoichiometric boron carbide is preferentially eroded, leaving behind grain-boundary pits. The stoichiometric B_4C showed excellent erosion resistance with characteristics similar to those of α-SiC. B_4C grains, however, eroded uniformly and there was no evidence of anisotropy resulting in grain faceting as was noted in

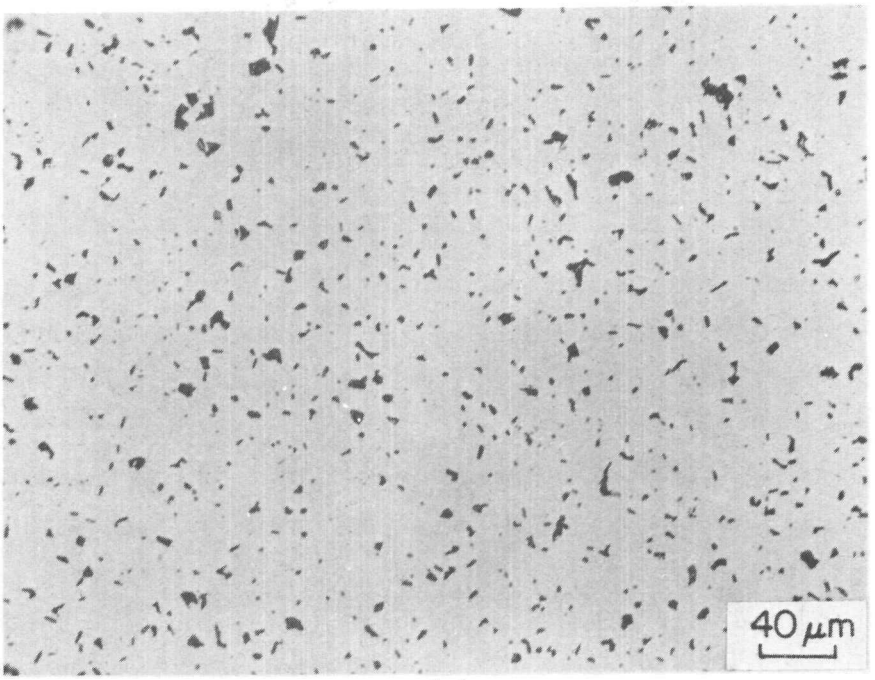

(a)

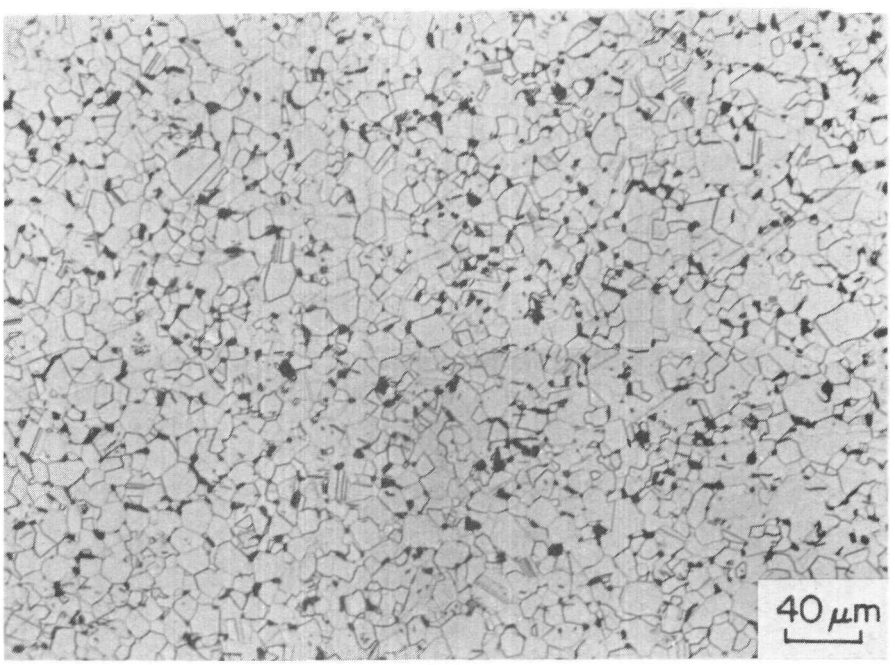

(b)

FIGURE 41. MICROSTRUCTURE OF HOT-PRESSED B_4C - I

(a) As-Polished

(b) Etched

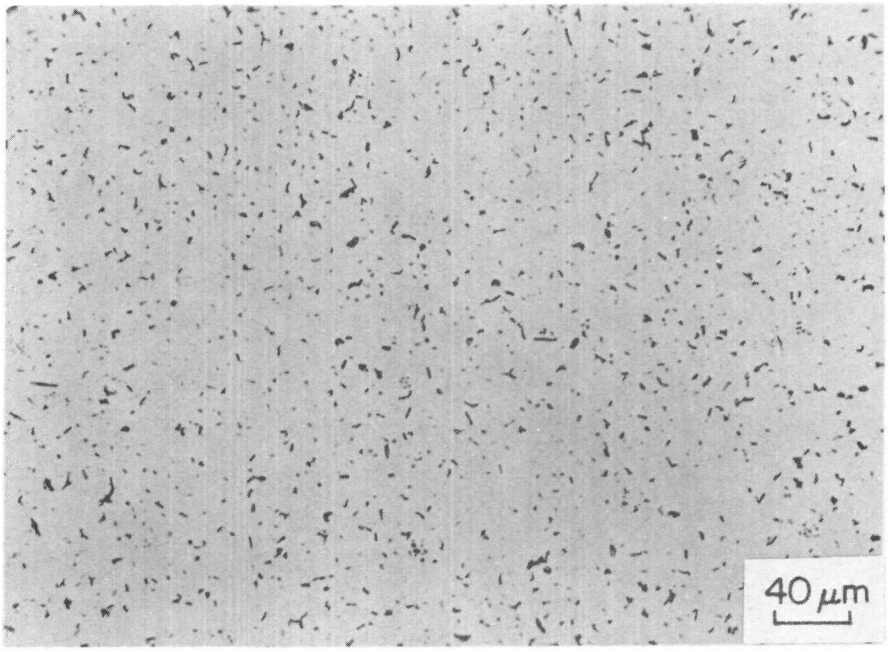

(a)

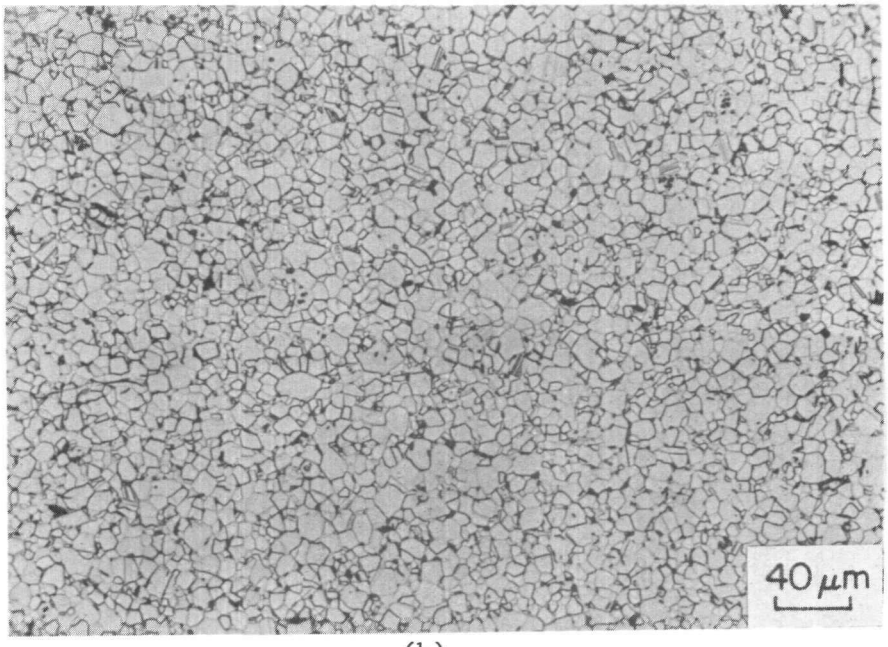

(b)

FIGURE 42. MICROSTRUCTURE OF HOT-PRESSED B_4C - II

(a) As-Polished
(b) Etched

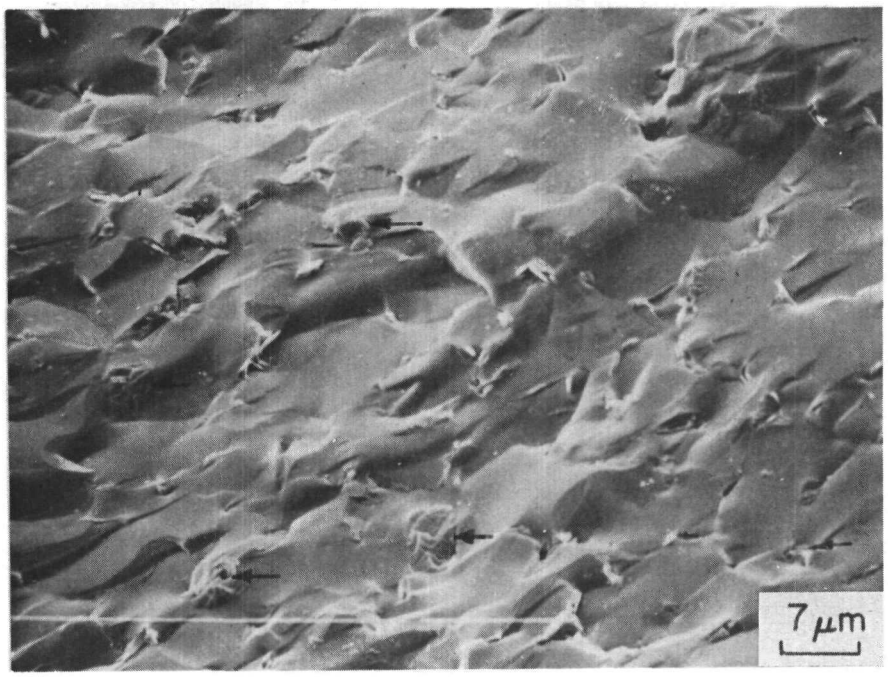

FIGURE 43. FRACTURE SURFACE OF HOT-PRESSED B_4C (B_4C - II SPECIMEN)

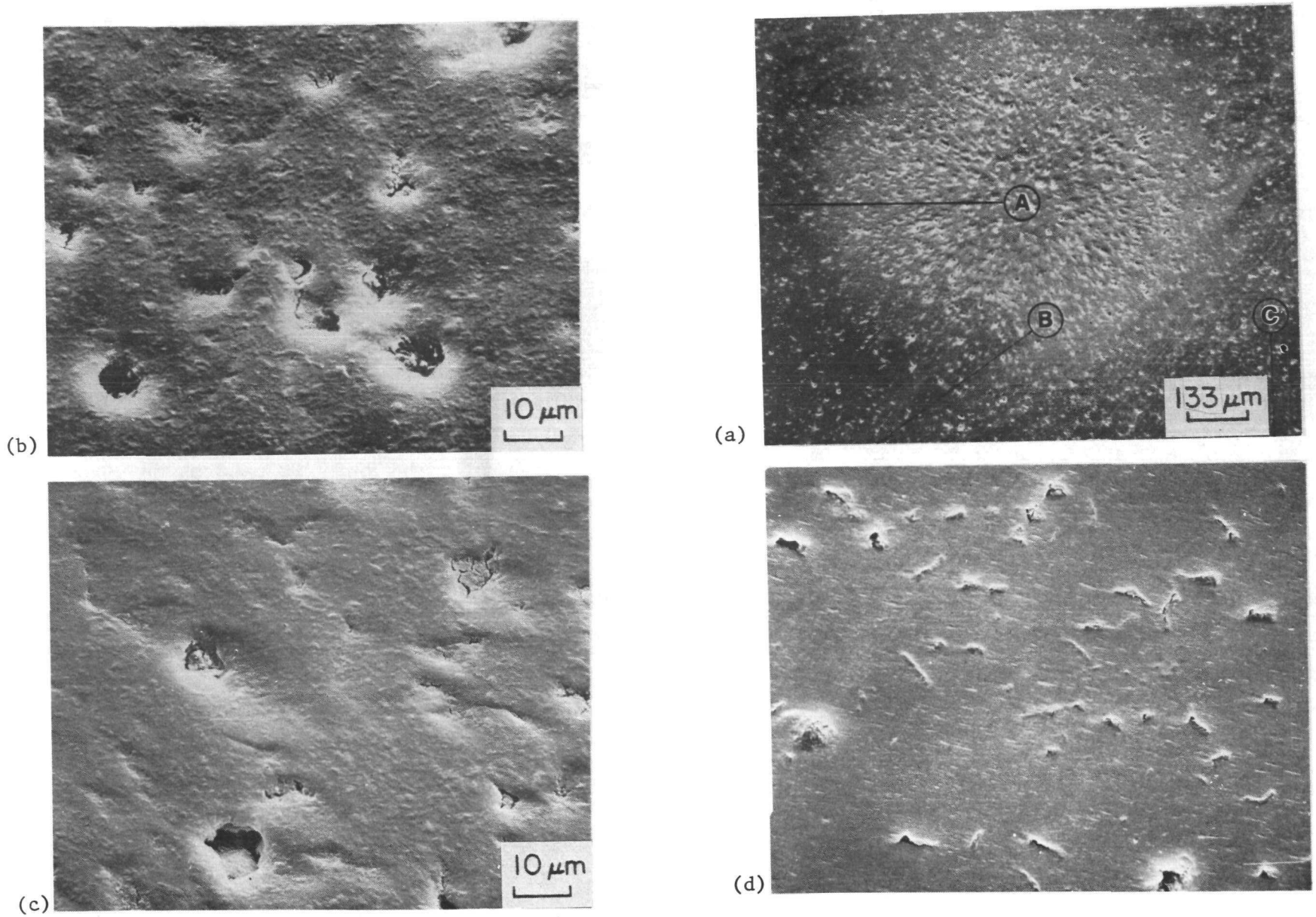

FIGURE 44. ERODED SURFACE ON HOT-PRESSED B_4C-I

(a) Wear Crater on Target Surface, (b) Center of the Crater, (c) Periphery of the Crater, (d) As-Polished Surface

the α-SiC. The grain-boundary pits in the center of the crater (Figure 44b) did not exhibit any directional features, presumably because of the normal incidence of the impinging SiO_2 particles. Near the crater periphery the grain-boundary pits showed characteristic radial streaks. These were caused by the radial flow pattern of the slurry and the streaks were downstream channels where the material had been preferentially eroded away. The enhanced erosion was caused by the higher impingement angle provided by the side of the pit in the radial direction. The erosion characteristics of the B_4C-II specimen were very similar to those of the B_4C-I specimen. Due to the smaller grain size and the higher density of the grain-boundary phase and the resulting grain-boundary pits, the characteristic streak pattern was clearly evident in the B_4C-II specimen (Figure 45).

Hot-pressed Alumina (AVCO)

The hot-pressed alumina erosion tested with the synthetic slurry was a 99.8 percent Al_2O_3 ceramic obtained from the AVCO Company. The microstructure of the material, shown in Figure 46, consisted of small (2 μm) uniform size equiaxed grains. Some grain-boundary porosity was present in the material, although this was not apparent in the as-polished specimen. An etched surface is shown in Figure 46.

The hot-pressed alumina was very similar to hot-pressed B_4C in its erosion characteristics (Figure 47). These included uniform nondirectional wear in the crater center (Figure 47b) and directional wear with the characteristic streaks near the crater periphery (Figure 47c). The intrinsic microstructural pores in the alumina generated the streaks and the resulting ripples. As in B_4C the intragranular wear was uniform and isotropic. The overall wear rate of the alumina was greater than the wear rates of α-SiC and hot-pressed B_4C (See Table 11). This was consistent with the lower hardness of Al_2O_3, relative to the hardnesses for SiC and B_4C. Hardness was expected to be the critical material property controlling the wear rate, because of the apparent ductile mode of material removal in all three materials.

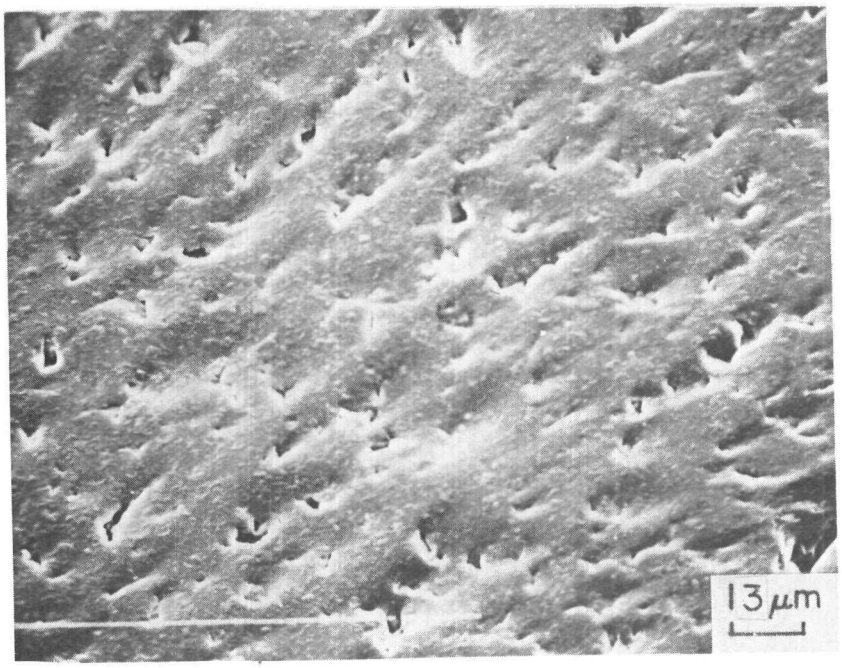

FIGURE 45. ERODED SURFACE NEAR CRATER PERIPHERY IN B_4C - II SPECIMEN

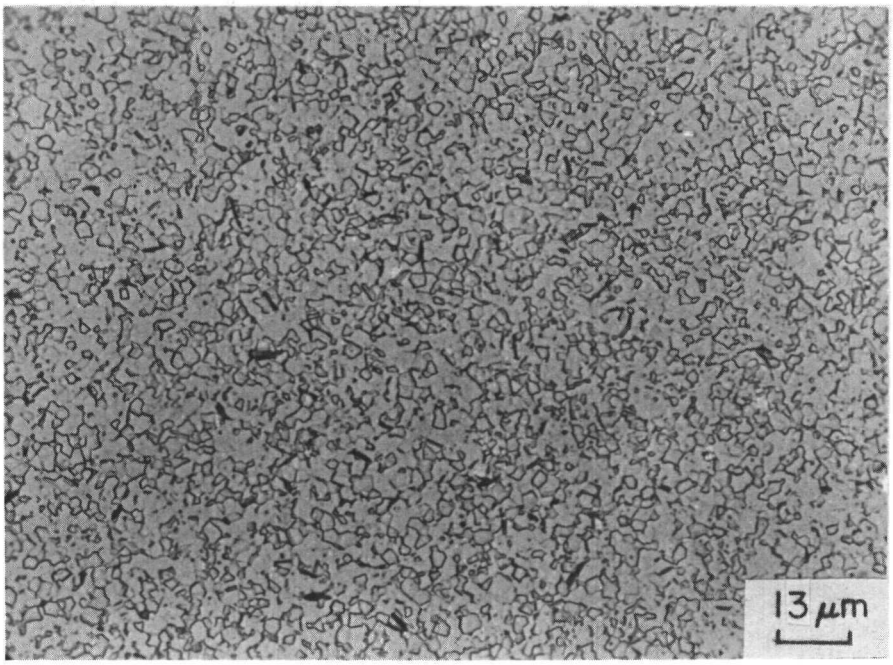

FIGURE 46. MICROSTRUCTURE OF HOT-PRESSED ALUMINA (AVCO)

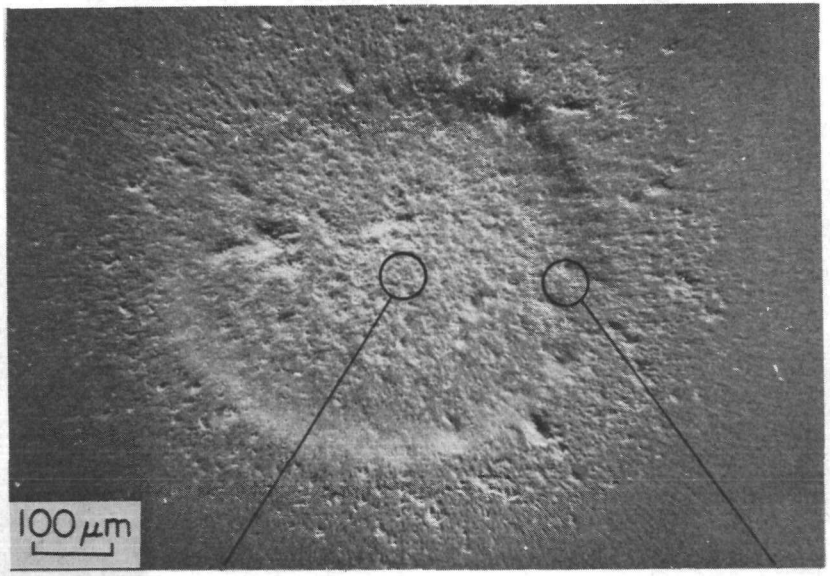

(a)

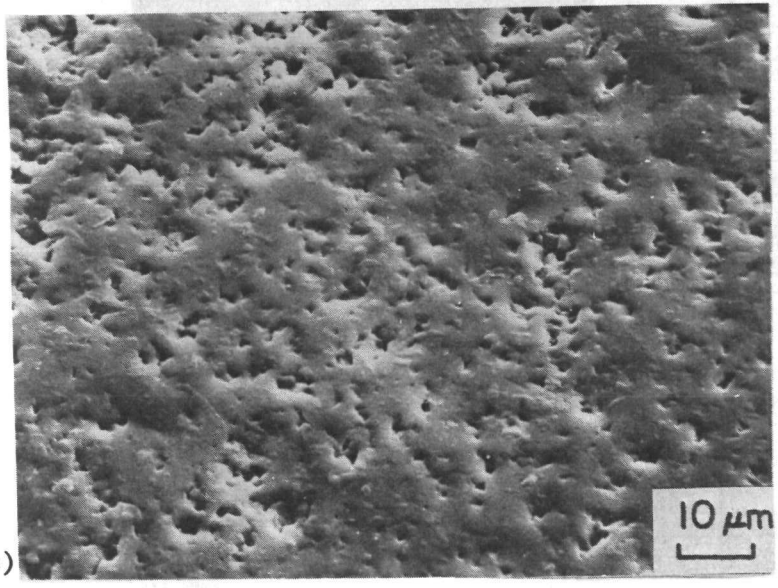

(b)

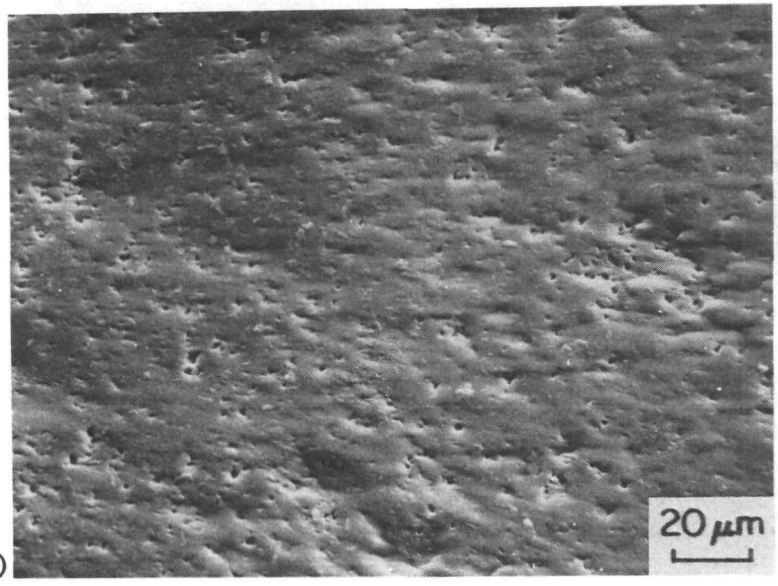

(c)

FIGURE 47. ERODED SURFACE ON HOT-PRESSED Al_2O_3

(a) Wear Crater on Target Surface, (b) Eroded Surface in the Center of the Crater, (c) Periphery of the Crater

Hot-pressed SiC (Norton NC-203)

The hot-pressed SiC had an equiaxed grain structure unlike its sintered counterpart, α-SiC. The grain size was reasonably uniform with an average size in the range 3-4 μm (Figure 48). The polished and etched microstructure shown in Figure 48 showed what appeared to be a considerable amount of porosity. Most of the apparent porosity was, however, not intrinsic, but due to grain pullout in the polishing and the etching stages.

Figure 49 shows the eroded surface on the hot-pressed SiC target. The erosion characteristics of the hot-pressed SiC material were very different from that of its generic counterpart, sintered α-SiC. As expected from the relative erosion rates of the two materials (Table 11) the test crater for the hot-pressed material was significantly deeper (Figure 49a). Detailed examination of the eroded surface near the center of the crater, Figure 49b, revealed that the material eroded in an intergranular failure mode, with only a small degree of intragranular wear. In some areas of the eroded surface the grains appeared to be covered with a coating (Figure 49c). The appearance of the coating did not indicate that it was from a foreign source. In some places it was present as an intergranular phase. Energy dispersive X-ray microanalyses conducted on areas covered with the coating (Figure 49c) and other areas without the coating (Figure 49b) indicated twice the concentration of Al in the coated area relative to the uncoated area. It is known that Al_2O_3 is added as a hot-pressing aid in the processing of this commercial grade of SiC. The coating that appears on some areas of the eroded surface may well be a segregation of this hot-pressing agent. The exact role of this intergranular phase in the erosion behavior is uncertain, but the above observations do suggest a relation between the intergranular phase that derives from the hot-pressing agent, and the intergranular mode of erosion.

An intergranular mode of erosion has also been observed in this material by Routbort and Scattergood[14] in erosion tests with alumina particles impacting the target surface in air. The erosion rates for the hot-pressed material were, however, less than the erosion rates for a reaction-bonded grade of SiC. This experimental observation is quite different from

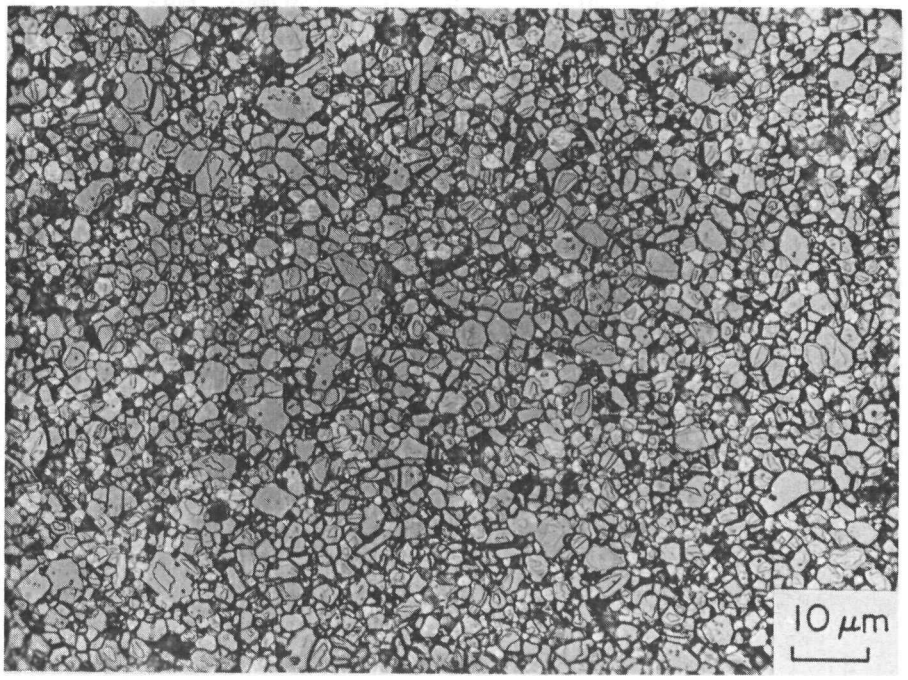

FIGURE 48. MICROSTRUCTURE OF HOT-PRESSED SiC (NORTON NC-203) ETCHED

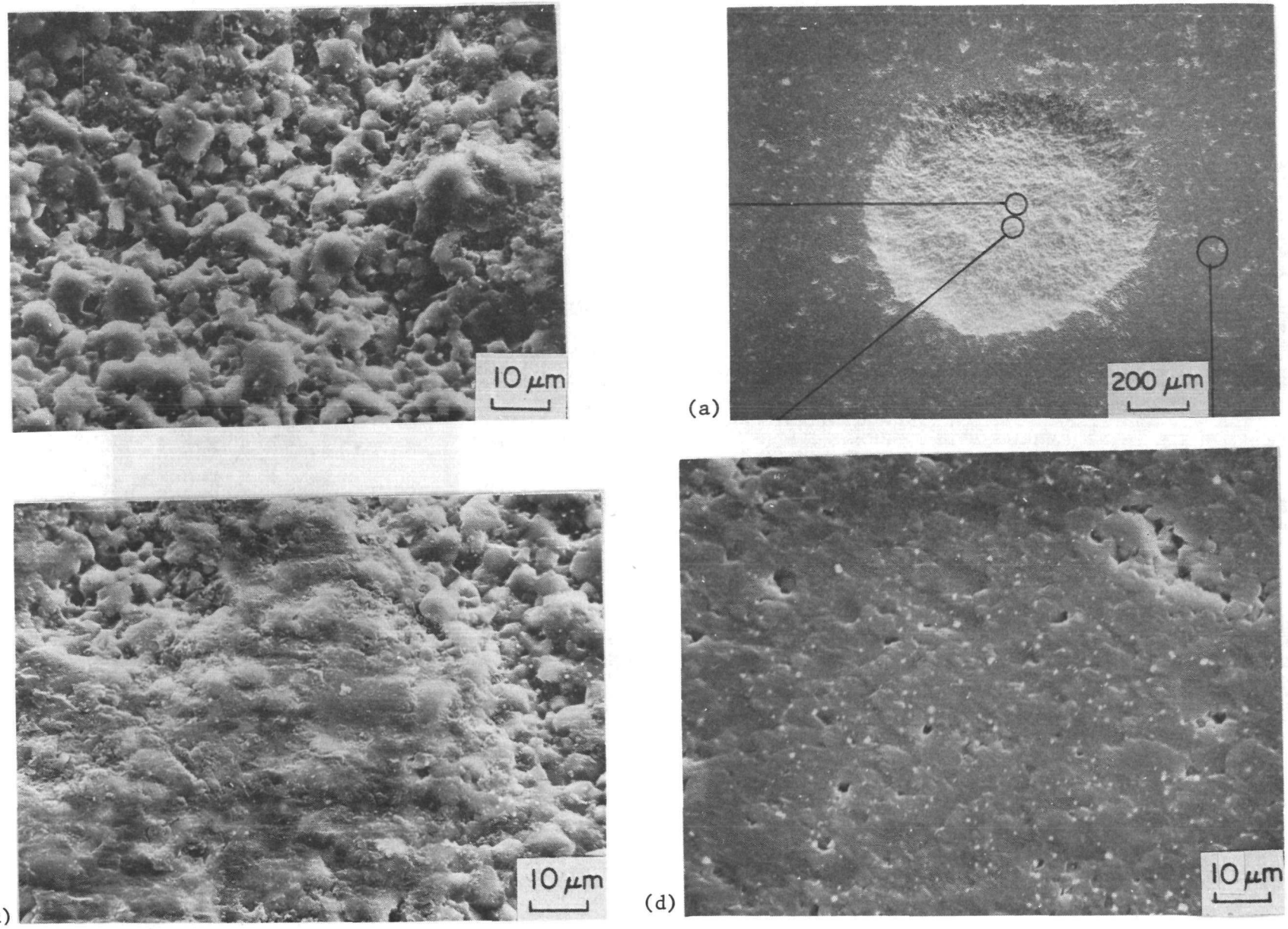

FIGURE 49. ERODED SURFACE ON HOT-PRESSED SiC
(a) Wear Crater on the Target Surface, (b) Eroded Surface near the Crater Center, (c) Intergranular Phase Covered Region, (d) As-Polished Surface of SiC

the experience in slurry erosion, which indicated a superior resistance to coal-slurry erosion for reaction-bonded SiC while the hot-pressed grade was significantly poorer.[15]

Hot-Pressed Si_3N_4 (Norton NC-132)

The microstructure of hot-pressed Si_3N_4 on a surface normal to the hot-pressing direction is shown in Figure 50. The grains were nonuniform in size and elongated. An average grain was approximately 2μm long and 0.5 μm in diameter. There was significant intergranular porosity apparent on the polished and etched surface. As was the case for hot-pressed SiC, some of this apparent porosity appeared to be due to grain pullout during surface preparation for microstructure examination.

The eroded surface of hot-pressed Si_3N_4 is shown in Figure 51. The macroscopic features of the test crater were different from those observed for hot-pressed SiC (Figure 49) in that the crater boundary was not as clearly defined and there was a significant amount of erosion damage outside the crater. The microstructural response of the material, however, appeared to be similar to that of the hot-pressed SiC. The high wear rate of the Si_3N_4 material (Table 11) appeared to be caused by an intergranular mode of wear similar to that of the hot-pressed SiC. The individual grain surfaces of Si_3N_4, however, showed significantly more wear as compared to SiC. This is probably due to the lower intrinsic hardness of Si_3N_4. Although the erosion test was conducted on the surface normal to the hot-pressing direction, the elongated-grain structure of the material was not apparent on the eroded surface (Figure 51b and 51c).

Soda-Lime Glass (Float Glass - PPG Industries)

Soda-lime glass was included in the synthetic-slurry screening test series because it provided a model material that was isotropic and amorphous, without the complications of microstructure. It also provided a brittle target material with low fracture toughness (K_{Ic} = 0.75 $MPam^{1/2}$) as well as

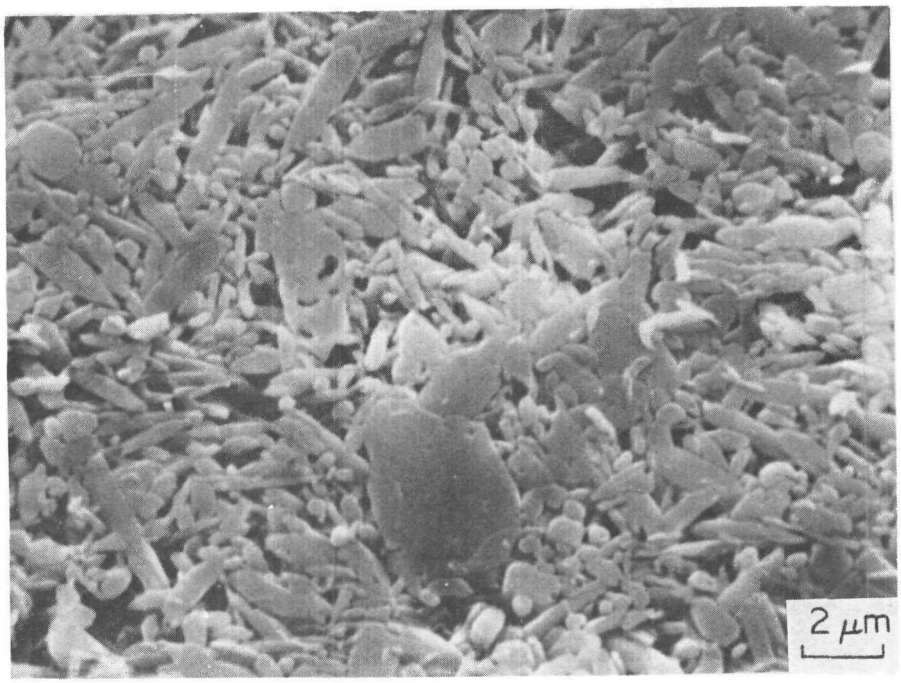

FIGURE 50. MICROSTRUCTURE OF HOT-PRESSED Si_3N_4

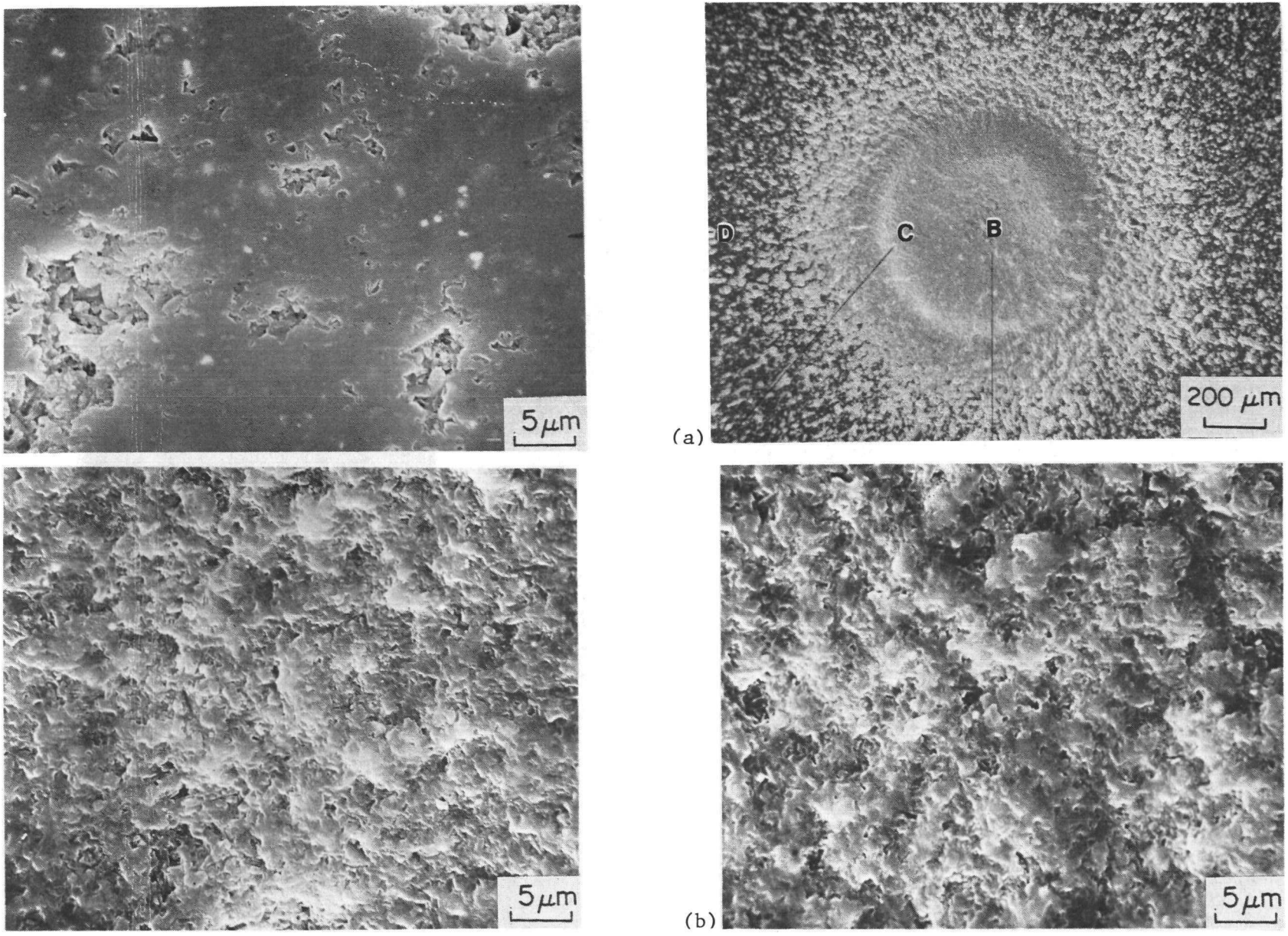

FIGURE 51. ERODED SURFACE ON A TARGET OF HOT-PRESSED Si_3N_4

(a) Test Crater, (b) Eroded Surface at Crater Center, (c) Eroded Surface at Crater Periphery, and (d) As-Polished Surface Away from the Crater

low hardness (H = 5.5 GPa). Thus, both brittle chipping and ductile cutting modes of erosive wear were expected to be enhanced in this material. Indeed, the erosive wear rate for glass was two orders of magnitude greater than, for example, the rate for α-SiC (Table 12).

Figure 52 shows the wear crater and the eroded crater surface after only 30 seconds of a slurry-jet impingement test under the standard screening conditions. The surface of the crater, Figure 52a, was relatively smooth along the outer edges and became increasingly rougher near the crater center. Detailed examination of the crater center, shown at higher magnification in Figure 52b, indicated that the glass eroded by a brittle chipping mode in this location. The morphological features of the chipped surface at the center suggested that the brittle chipping was caused by elastic-plastic indentation and the resulting subsurface lateral cracking.[6,16] The periphery of the crater did not show any evidence of brittle chipping. The crater surface exhibited ripples and the surface structure within the ripples consisted of very small, directional tracks, Figure 52c, presumably made by the impinging SiO_2 particles. Individual particle tracks could be observed at very high magnifications (10,000X) as shown in Figure 52d. It should be noted that a particle is still embedded at the end of the track in the center of Figure 52d. These characteristics of erosion indicated a ductile mechanism of wear involving ductile cutting and/or ploughing.[17,18] The origin of the macroscopic ripples observed near the crater periphery could not be ascertained, but similar rippled surfaces have been observed on plate glass by Sheldon and Finnie[19] following erosion with fine SiC particles (1000-mesh grit) at small impact angles (30 degrees). These investigators also observed a transition in the erosive wear response of plate glass to a brittle chipping mode when they used 120 mesh grit SiC particles. In the present study this transition occurred in the same test as a function of the target area relative to the jet. In the center of the jet particles are likely to impact the target surface at 90 degrees, while near the periphery particles impact at small angles because of the stream line bending away from the target surface. It is also possible that larger SiO_2 particles may impact the target surface at angles closer to 90 than smaller particles, which would have a greater tendency

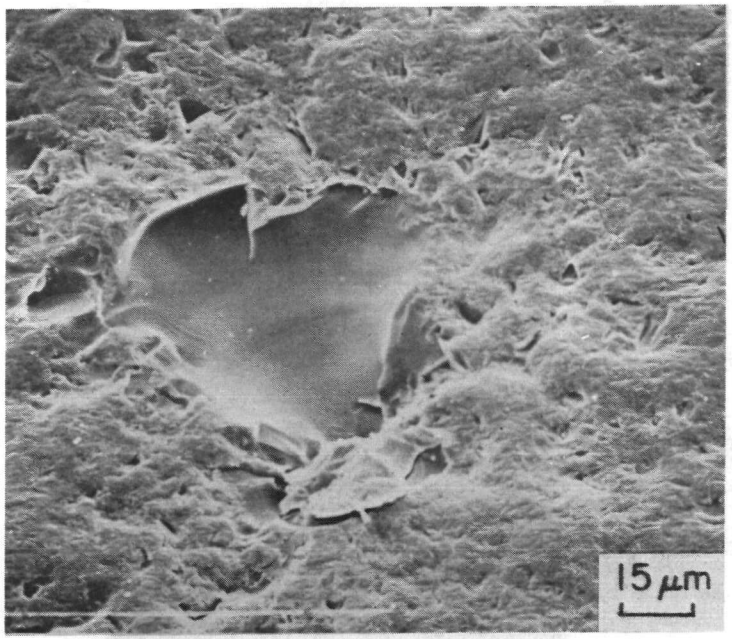

(b)

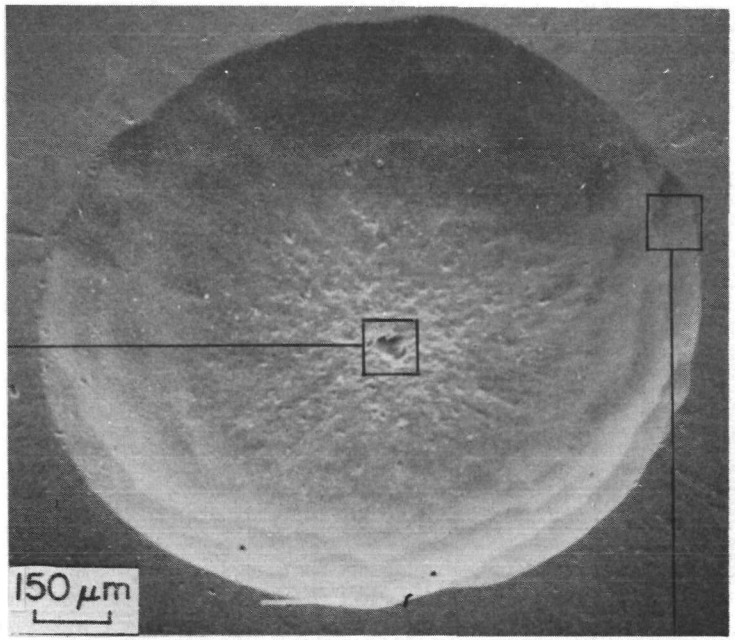

(a)

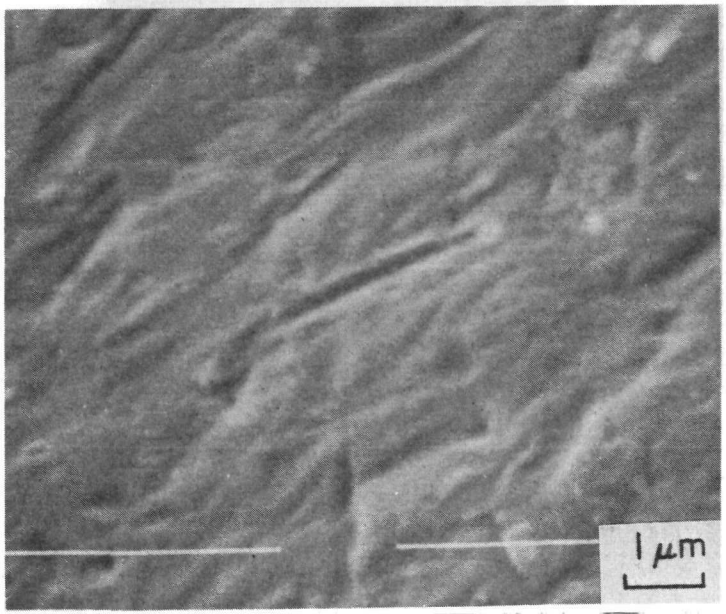

(d)

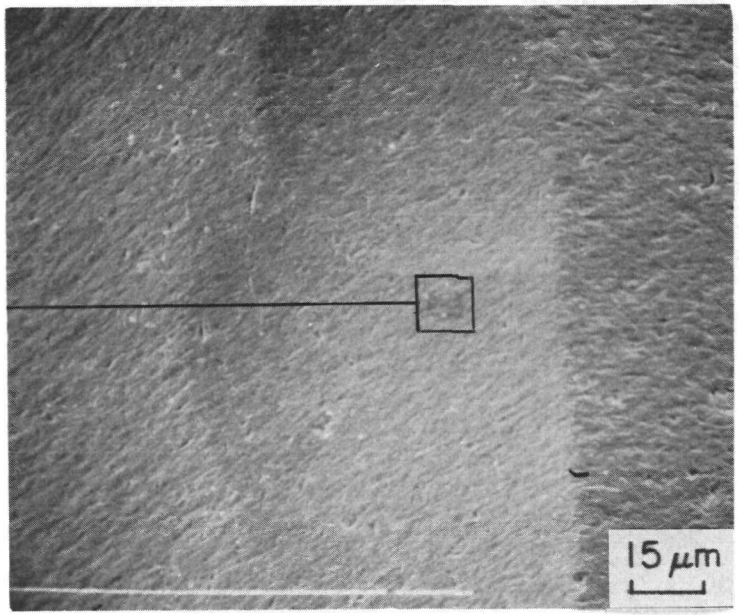

(c)

FIGURE 52. ERODED SURFACE ON SODA-LIME GLASS TARGET
(a) Wear Crater After 30 seconds of Test, (b) Typical Brittle Indentation and Fracture Damage at Center of Crater, (c) Edge of Crater, (d) Typical Ductile Ploughing Mode of Erosion at Crater

to follow the stream lines. These two factors may combine to promote brittle fracture near the target center (large particles and large angles of impingement) while ductile mechanisms prevail near the crater periphery (small particles and small angles of impingement).

III.2.4 Determination of Angle and Velocity Dependence of Erosion of Selected Materials

Characterization of the erosion behaviors of the materials listed in the synthetic slurry screening tests revealed several different modes of material removal. α-SiC, HP-B_4C, and HP-Al_2O_3 eroded in a similar manner and exhibited low wear rates. Hot-pressed SiC and Si_3N_4 eroded by an intergranular failure mechanism with an order of magnitude increase in wear rates. Finally, soda-lime glass exhibited an interesting combined mode of erosion that involved both brittle chipping (near the crater center) and a ductile cutting mechanism (near the periphery). A particularly interesting observation in the screening tests was the vastly different performances of two different grades of a same generic material: SiC. α-SiC is a 98 percent dense sintered material that is essentially 100 percent α-phase with a mixture of the polytypes 6H, 4H, and 15R.[20] The hot-pressed grade of the SiC is 99-100 percent dense and consists of nominally 85-100 percent 6H type with the SiC amounting to 94-96 percent of the final composition.[21] Thus, the difference in the wear behaviors cannot be attributed to different crystallographic phases or differences in densities. The grain morphologies are, however, different in the two materials with interlocking tabular grains in α-SiC and equiaxed grains in the hot pressed material. Significant differences are also expected in the grain-boundary chemistry because of differences in the amounts and types of sintering aids used in the processing of the two materials. The differences in the wear behaviors of the two grades may, therefore, be related to grain morphology, grain-boundary phases, and chemistry. To further evaluate the characteristics of erosive wear of the two materials by the two different mechanisms, the effects of slurry velocity and slurry-jet impingement angle on erosion rates were examined.

III. 2.4.1 Influence of Slurry Velocity. Figure 53 summarizes the slurry-velocity effects on the erosion rates of the hot-pressed and the sintered grades of SiC. The erosion tests were conducted with the substitute slurry (Energol + 8 percent by weight silica) in the once-through testing mode. The nominal slurry velocity was varied in these tests by varying the H_2/Ar overpressure in the slurry chamber. A constant jet impingement angle (90 degrees) and test duration (10 minutes) were maintained in all the tests.

Figure 53 shows the relation between the maximum and average depths of the craters and the nominal slurry velocities for the two materials. The linear relations between the crater depth, d, and the slurry-jet velocity, v, on the log-log plot suggests an empirical relation:

$$d = \bar{A} \cdot v^{\bar{b}} \tag{6}$$

where $\bar{A}$ and $\bar{b}$ are empirical parameters, dependent on experimental conditions and target material.

The apparent velocity exponents, $\bar{b}$, determined by least-squares regression analysis, are indicated by the slopes of the best-fitting lines in the figure. Since all the erosion tests at different slurry velocities were run for the same test duration (10 minutes) the apparent velocity exponent, $\bar{b}$, reflects the influence of both the slurry velocity and slurry volume. Pure velocity exponents can be obtained by rewriting Equation (6) as

$$d = A \cdot v^{b} \cdot (avt) \tag{7}$$

where

(avt) = Volume of the slurry used in each test

a = Cross section of the jet orifice

t = Time of the test (10 minutes)

b = True velocity exponent = $\bar{b}$-1

A = Erosion depth per unit slurry velocity and unit volume of the slurry = ($\bar{A}$/at).

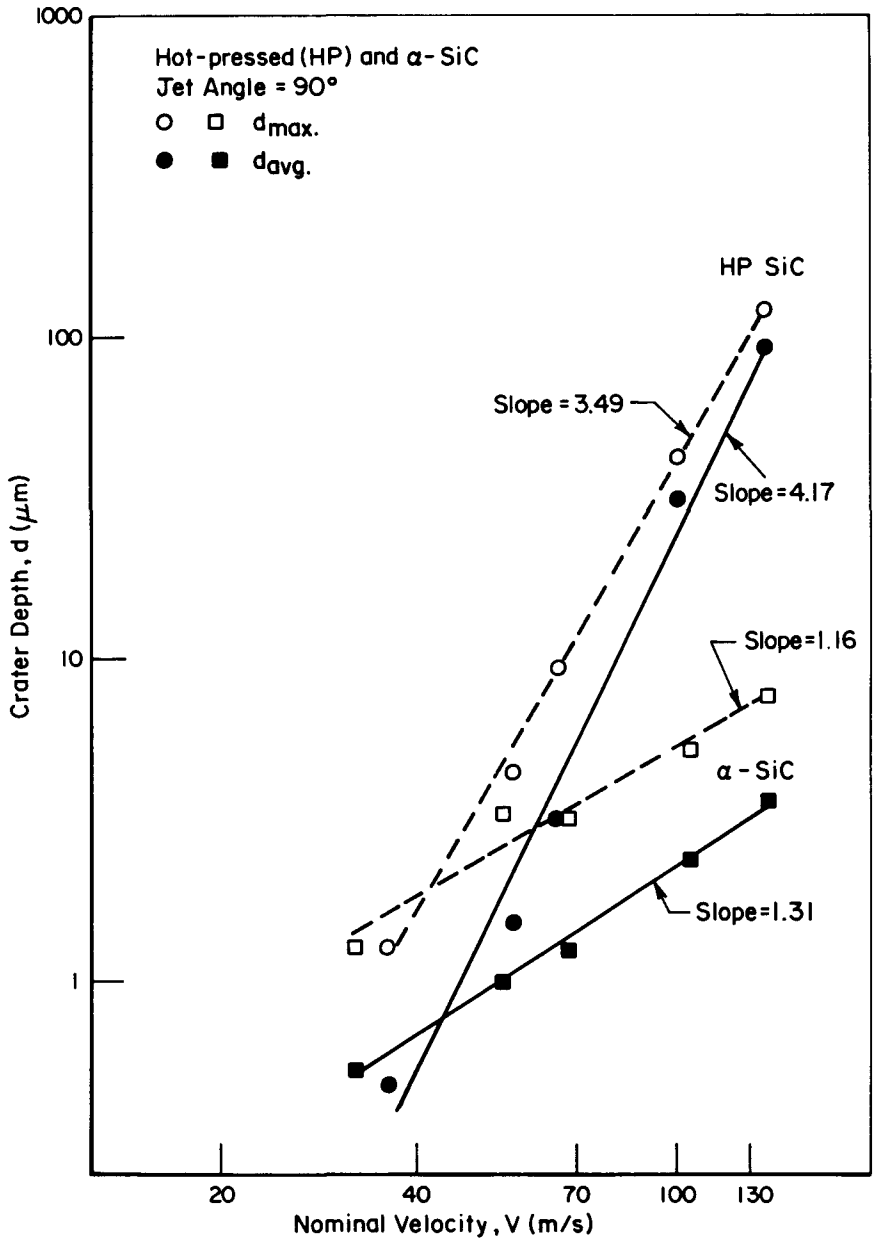

FIGURE 53.
SLURRY-JET VELOCITY DEPENDENCE OF EROSION RATES FOR HOT-PRESSED (HP) AND SINTERED (α) SiC

It is seen from Figure 53 that the true velocity exponent for the hot-pressed SiC, as inferred from the average crater depth, is 3.17 while the corresponding exponent for the sintered SiC is 0.31. The exponent observed for the hot-pressed SiC is very similar to the velocity exponents measured for the cemented carbides with coal-derived slurries[3]. But, the exponent observed for the sintered grade of SiC is unusually low. Erosion theories that are based on particle impact damage, and involve mechanisms of material removal by either plastic cutting or elastic-plastic fracture, generally predict velocity exponents in the range 2 to 3.5[3]. It is not clear as yet why the sintered SiC exhibits the low velocity exponent.

III.2.4.2 Influence of Slurry Jet Impingement Angle. The variations of the jet-impingement angle for the hot-pressed and the sintered SiC targets are shown in Figure 54. As in the velocity studies, the tests were conducted with the (Energol + 8 percent by weight silica) substitute slurry in the once-through testing mode. The nominal slurry velocity was held constant at 105 m/second and each test was run for 10 minutes.

The qualitative features of the impingement angle dependence of erosion rates are very similar for the hot-pressed and the sintered SiC. The erosion rates are maximum and nearly constant for impingement angles between 90 and 50 degrees. The erosion rates decrease rapidly for angles less than 50 degrees. Thus, it appears that the angular dependence of erosion rates are the same even though the mechanisms of material removal for the two target materials are quite different. The absolute erosion rates are quite different for the two materials in the high-angle regime, but at impingement angles less than 30 degrees the two materials appear to erode at approximately the same rates.

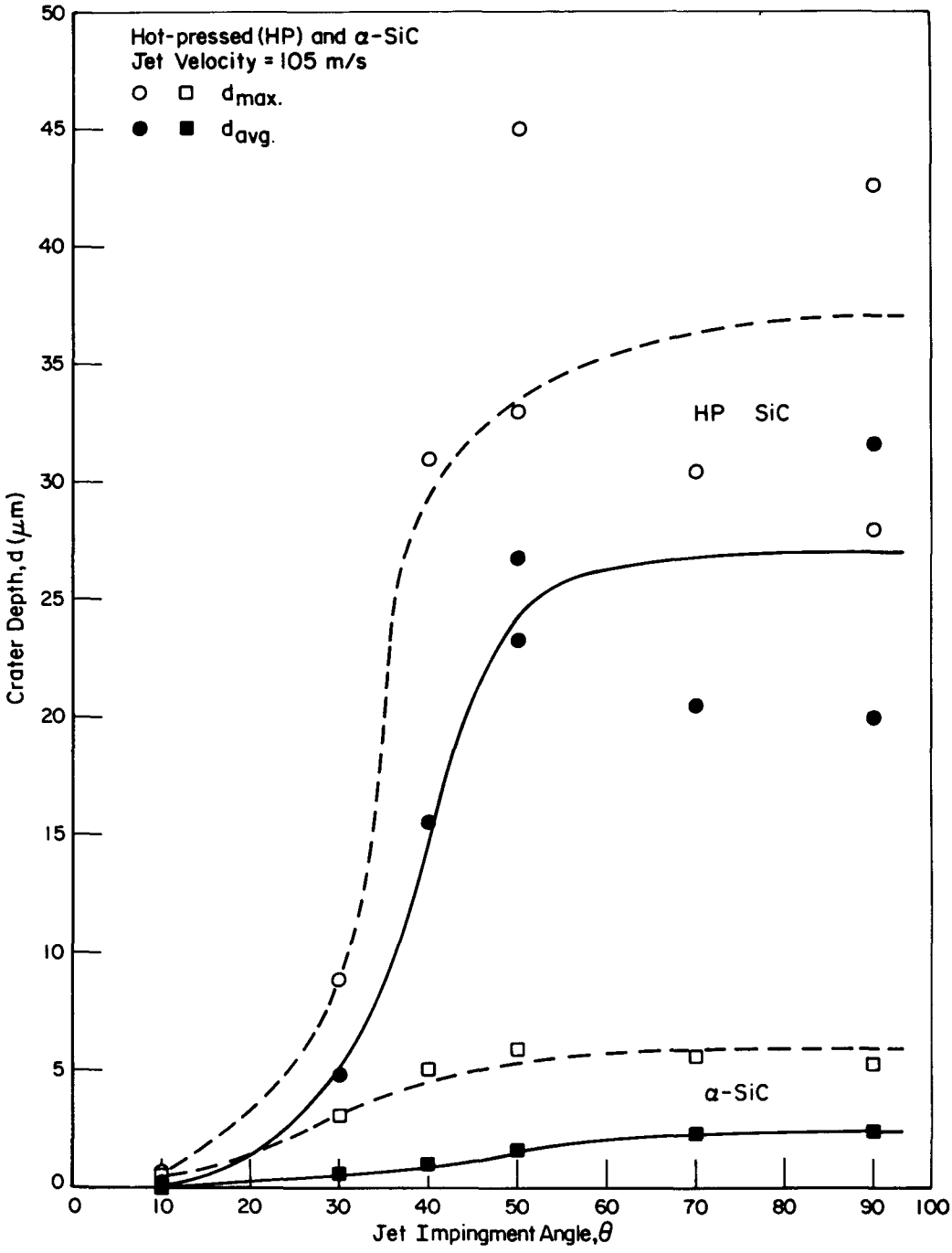

FIGURE 54.
SLURRY-JET IMPINGEMENT ANGLE DEPENDENCE OF EROSION RATES FOR HOT-PRESSED (HP) AND SINTERED (α) SiC

III.3 Approaches to the Development of New Materials

III.3.1 Laser Surface Processing

Laser surface processing methods were applied to hardfacing alloys as a means of modifying the surface microstructures to improve erosion resistance. Process development was undertaken in 3 stages--laser surface melting of bulk hardfacing materials, production of laser-fused hardfacing overlays on steel substrates, and laser cladding of mixed hard-phase particulates.

III.3.1.1. Surface Melting. The first experiments concerned skin melting of the three Stellite alloys: No. 1, No. 12, No. 6B. The purpose of the shallow melts was to refine grain size and thereby increase surface hardness. The principal differences in the alloys lay in the carbon and tungsten contents. Carbon composition ranged from 1 percent by weight in Stellite No. 6B up to 2.5 percent in No. 1; tungsten varied from 4 percent in No. 6B to 12 percent in No. 1. Stellite No. 1 was the hardest alloy in the as-received condition. The goals of this task were to produce continuous uncracked surface melted specimens with more homogeneous microstructures than normally processed alloys, so that the effects of large morphological variations could be compared in coal slurry erosion performance.

Figure 55 sketches the processing configuration for the initial surface-melting experiments. A 5-kilowatt continuous wave CO_2 laser was employed. Laser output was shaped to a square cross section using overlap integration optics. The beam size was approximately 3 x 3 mm at the workpiece, and the delivered power varied from 2 to 5 kilowatts.

Test specimens were placed on a graphite block which was translated under the laser beam at constant speeds of 10 - 100 mm/s. The interaction region was bathed in argon provided by a shielding nozzle (Figure 55). In some cases, the test pieces were preheated in a tube furnace at temperatures of 250-670 C (482-1238 F).

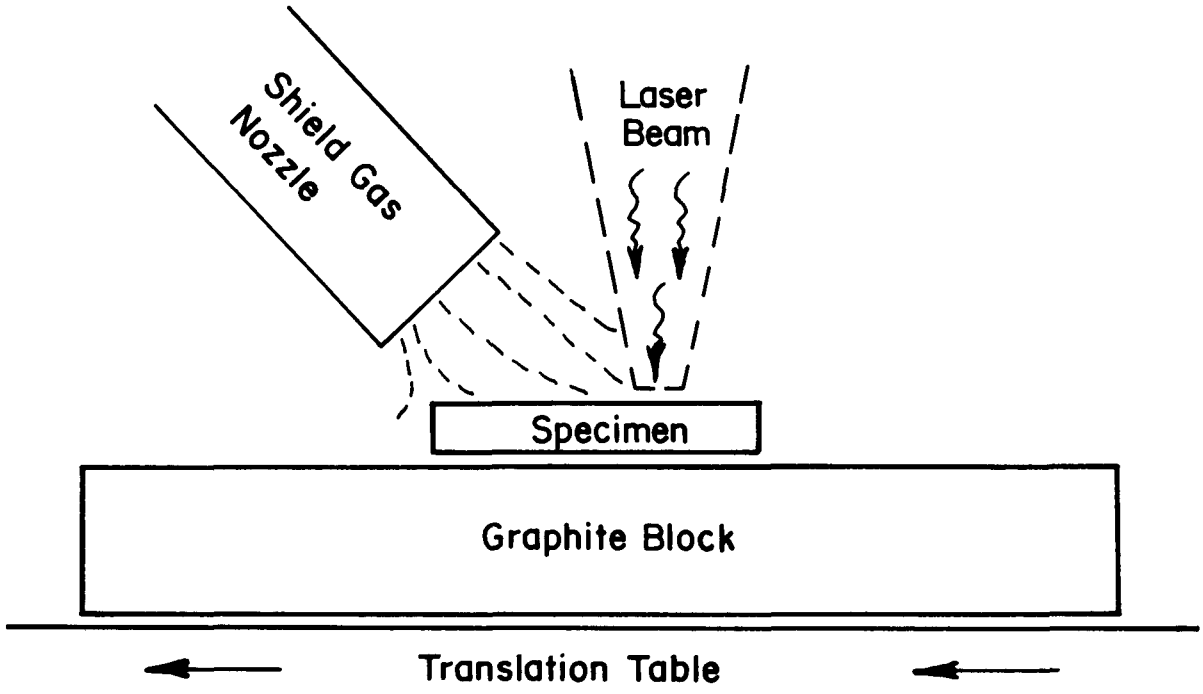

FIGURE 55. PROCESS SCHEMATIC FOR LASER SURFACE MELTING OF STELLITE COUPONS

Specimens of Stellite 1 and Stellite 12 were made by sectioning a 25 mm-wide weld bead of each material. The specimen dimensions were ~25 x 10 x 5 mm (thick). The top surfaces of these alloys were coated with flat black paint to increase laser absorption. Although the paint layer chars when a specimen is preheated, the laser absorption remains high. Coupons of Stellite 6B, about 20 x 20 mm, were prepared from 1.5-mm-thick sheet stock. The Stellite 6B coupons were given a mild grit-blasting treatment to create a matte surface finish.

With Stellite 1 -- Smooth uniform melts were obtained in single passes. Cracking was present in all cases. At the highest preheat temperature investigated, 670 C, cracking was limited to three widely spaced transverse cracks spanning the entire melt width.

With Stellite 12 -- Uniform melts about 3 mm wide and 0.3 mm deep were produced as shown in Figure 56. A preheat temperature of 670 C was employed; no cracking occurred on these specimens. The melt zone exhibited a refined dendritic solidification microstructure. A direct comparison of the fusion zone microstructure and original grain size can be made from Figure 57, showing an order of magnitude grain refinement in the laser-melted area. Note that the original grain size is larger than the average erosive particle size used in the coal-slurry test, while the laser-melted microstructure is considerably finer than the erosive particles. Microhardness measurements in the laser-processed area averaged 710 KHN versus 522 KHN for the original material. This increase in hardness can be attributed at least partially to the refined microstructure. However, the presence of different carbide species in the processed region must also be considered. Two distinct carbide phases were detected in the original microstructure, but were not evident in optical micrographs of the laser-processed cross sections up to 1200X magnification.

With Stellite 6B -- Smooth, thin melts were produced at the higher powers and faster scan rates (~100 mm/s) in the ranges previously reported. No specimen preheat was required, although in some melt passes there was evidence of localized interdendritic separation. Extended area melt layers were produced by multiple laser passes with about 50 percent overlap from pass to pass.

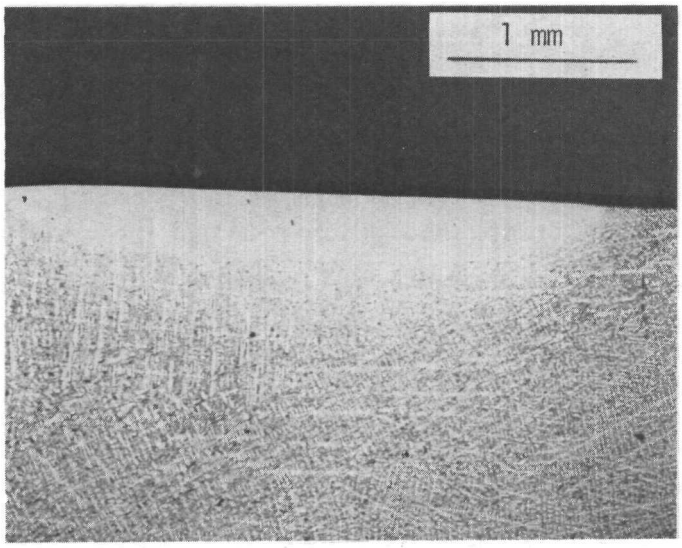

(a)

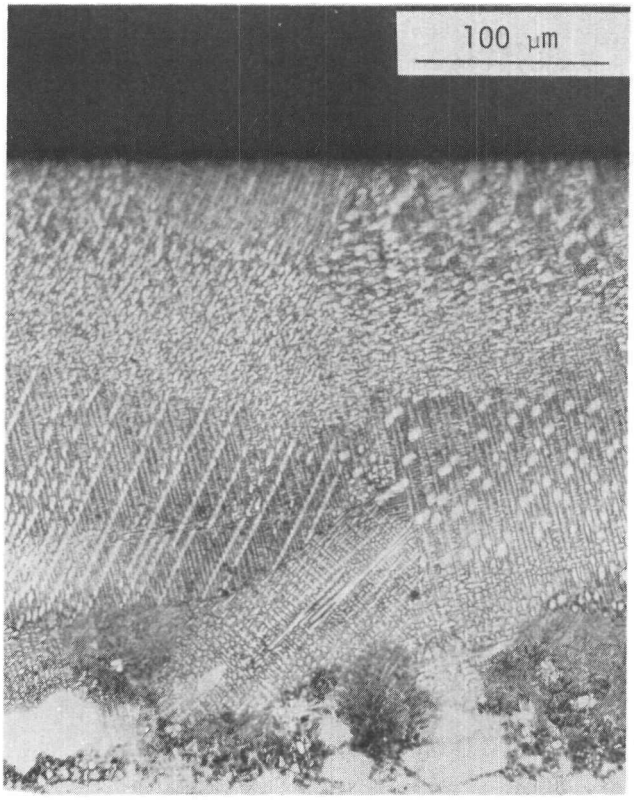

(b)

FIGURE 56. FUSION ZONE CROSS SECTION FOR SINGLE MELT PASS ON STELLITE 12 SPECIMEN

(a) View of Complete Width of Melted Zone
(b) Detail of Melted Zone

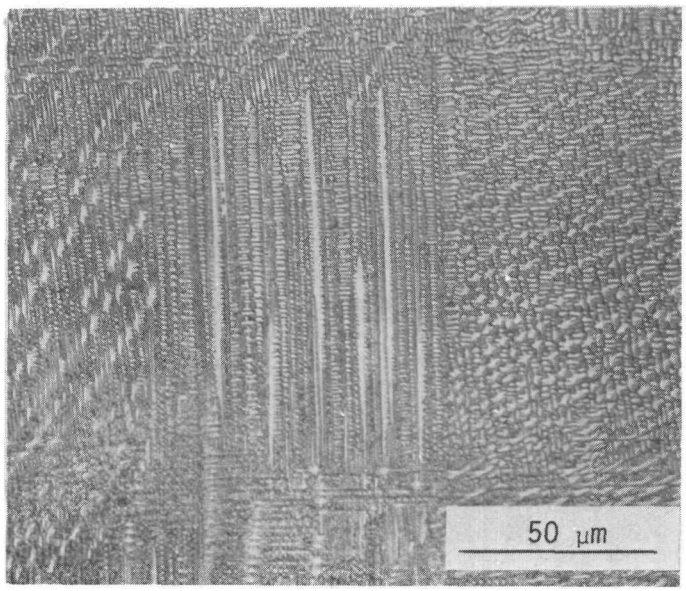

(a)

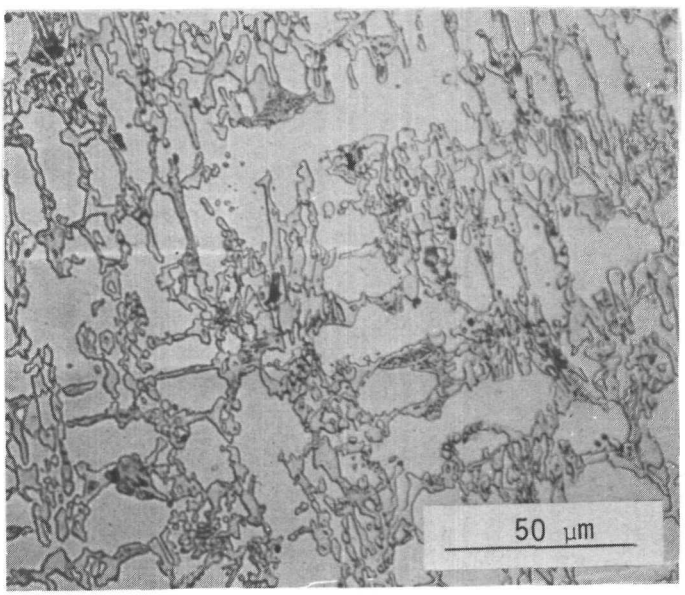

(b)

FIGURE 57. COMPARISON OF (a) The Laser Fusion Zone Microstructure With (b) Original Substrate Microstructure (Bottom) in Stellite 12.

A cross section taken perpendicular to the scan direction (Figure 58) revealed a thin dendritic surface layer of nearly uniform depth. There were no obvious microstructural changes defining a heat-affected zone although a thin partial melt zone along the bottom of the melt layer was detected. Overlapping melt passes produced no apparent differences in structure from single passes. In fact, the overlap zones are not even distinguishable in the cross section micrographs.

Figure 59 shows a high magnification view of a region in Figure 58. The dendritic grain size was comparable to that in the laser-melted Stellite 12 (Figure 57). The layer thickness averaged 60 μm, which is extremely thin for a 100 mm/s scan rate. Hardnesses for this specimen averaged 600 KHN for the laser-melt region and 450 KHN in the original material. The percentage increase in hardness in Stellite 6 was the same as that for Stellite 12.

III. 3.1.2 Laser-Fused Hardfacing Powders. Coatings of hardfacing alloys were applied to mild steel specimens by laser-melting powder that was placed on the specimen surface. An example of such a coated specimen is shown in Figure 60. The light-trapping effects of the particulate surface allow for significantly higher laser absorption than that of a flat metallic surface and apparently permit transmission of a portion of the incident laser energy to the substrate. The result is a metallurgically bonded hardfacing overlay.

The powders were applied to the specimens with a thin metal mask in place to assure a uniform deposit thickness. Masks 0.25 to 0.84 mm (0.010 to 0.033 in.) thick were used. Two Co-based powders (Stellite 6B and Haynes Alloy No. 25) produced acceptable coatings. Particle size averaged about 100 μm.

The prepared specimen was scanned under a partially focused CO_2 laser beam at powers of 2-4 kilowatt and a beam size of approximately 3.18 mm (0.125 in.) on the specimen surface. A square area 32 x 32 mm (≈ 1.25 x 1.25 in.) was covered by a set of overlapping linear passes at translation speeds of 21 to 42 mm/s (50 to 100 inches/minute) with interpass separations of 2 mm (0.08 in.) This raster pattern coverage was sufficient to melt the entire powder layer and fuse it to the test piece.

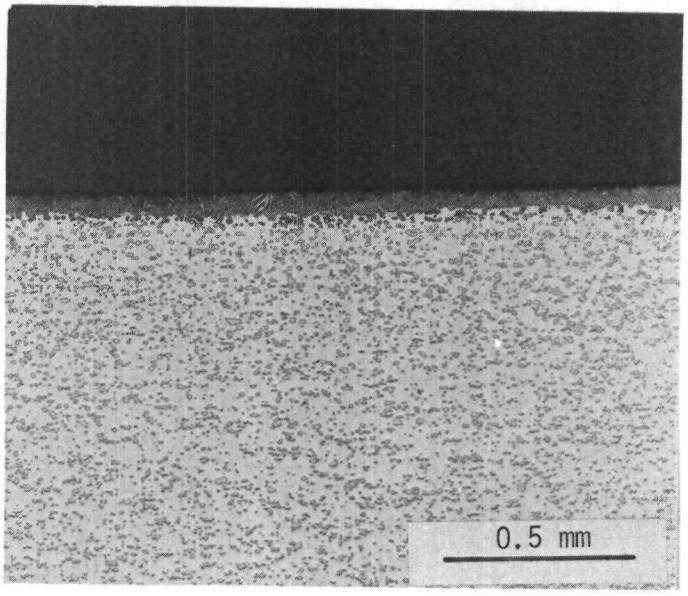

FIGURE 58. OVERLAPPING LASER MELT TRACKS ON STELLITE 6B SPECIMEN - FIELD OF VIEW EQUALS ABOUT TWO OVERLAP WIDTHS

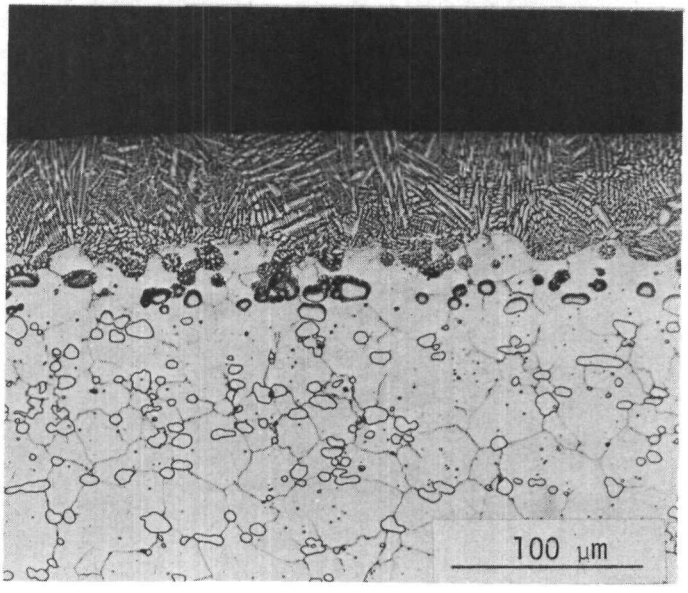

FIGURE 59. LASER MELTED STELLITE 6B SPECIMEN CROSS SECTION AT HIGH MAGNIFICATION SHOWING REFINED DENDRITIC SOLIDIFICATION STRUCTURE

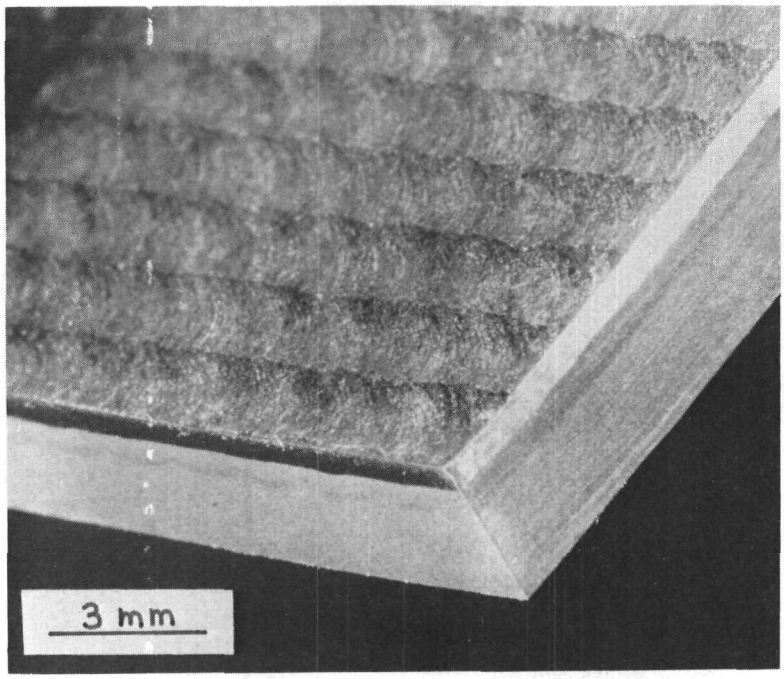

FIGURE 60. LASER-FUSED COATING OF STELLITE 6B POWDER ON 1018 STEEL

A mild flow of inert shielding gas was generally employed to keep the coating clean during processing. However, it was found that the initial powder fusion treatment could be performed with no external shield gas. Under these conditions, the underlying material seemed to melt and bond as normal, but a surface layer of oxides remained. For the Stellite 6B coating, the oxide was a light green color; with Haynes 25 the deposit was dark and glassy.

The best surface coatings were achieved employing a second laser raster coverage with the scans at right angles to the original melt passes. The second laser treatment, which used a localized Ar or He shielding gas flow, smoothed out the surface topography and eliminated surface oxidation products.

Stellite 6B powder was found to be well suited for this coating process. The overlays showed excellent interface bonding, a complete lack of internal porosity, and no tendency to crack. The coating thickness remained uniform and surface smoothness was good. The grain size and orientation for the Stellite coatings were comparable to those of the laser-melted bulk Stellite 6 alloys. The micro-hardnesses were also equivalent.

A Haynes 25 alloy coating cross-section is shown in Figure 61. The initial laser scan direction was longitudinal (in the plane of the figure); the secondary laser passes were made normal to the picture plane. The field of view surveys about 4 overlapping secondary melt passes. It can be seen that the second set of passes melted about half of the coating layer, indicating the difference in absorption between the preplaced powder and the laser consolidated overlay. This particular etch condition revealed the lateral convection currents produced in the laser melted trails.

The quality of the Haynes 25 overlays was slightly inferior to the Stellite coatings. While interface bonding and lack of porosity were as good, there was a more pronounced tendency to form oxidation products. This oxidation left the as-processed surface less smooth than the Stellite 6B surfaces. More importantly, there was a higher tendency for crack formation. Subsurface microcracks were present at the edges of overlapping melt passes.

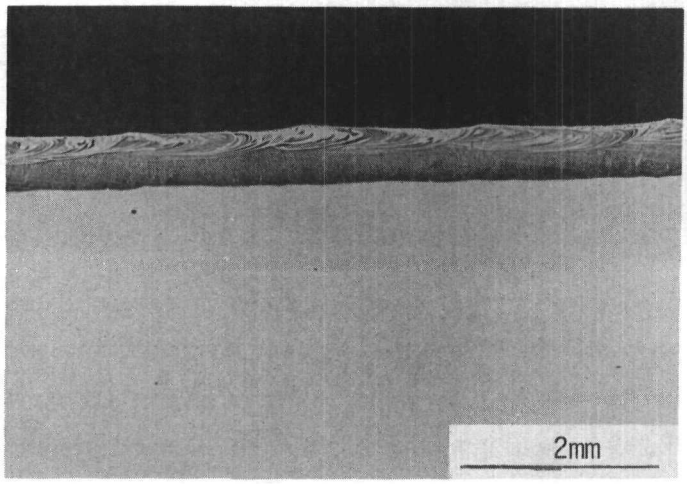

FIGURE 61. LASER CLAD HAYNES ALLOY #25 ON MILD STEEL

III.3.1.3 Dual Phase Claddings. In an initial attempt to produce controlled cermet-like surface structures, hard phase particles were added to hardfacing powders. The resultant cladding was a mixture of fused hardfacing alloy and unmelted carbide particles, as shown in Figure 62. The mixture of titanium carbide and Stellite 6 showed the most promise. The majority of the carbide material was unchanged by the laser fusion process. However, a small fraction dissolved in the melt and precipitated during cooling as a finer-scale TiC. By varying the original particle size distribution and laser processing parameters, it should be possible to influence the relative amounts of large blocky carbide and precipitated phase. The coating of Figure 62 showed few problems with cracking and no irregularities at the substrate interface. A potential problem was the random porosity which could probably be eliminated by a somewhat slower process speed.

Another set of experiments with Stellite 6 and tungsten carbide particles instead of titanium carbide particles produced coatings with severe porosity and cracking problems. However, the cross-sectional microstructure (Figure 63) revealed an encouragingly uniform composite structure. Although a small amount of carbide dissolution was expected during processing, no precipitated WC was observed. The difference between this behavior and that of Figure 62 is probably related to the difference in carbide forming tendencies between W and Ti and their diffusivity. In the WC case, additional fine carbide precipitation may be possible through tempering treatments.

The process for cladding of WC + Stellite was modified by adding a flexible diaphragm for more complete gas shielding and by reducing laser scan speed. The porosity was significantly reduced over the initial attempts using gas nozzles. In addition, the coating surface was bright and shiny and the cracking resistance was somewhat improved. However, stress cracking was not entirely eliminated.

This same process was applied to a mixture of WC and Haynes 25 powder coating. The starting volume fraction of carbide was 25 percent. It was thought that Haynes 25 would be a more suitable binder material than Stellite 6 by virtue of its lower carbon content. However, the composite overlay exhibited no improvement in crack resistance over WC and Stellite

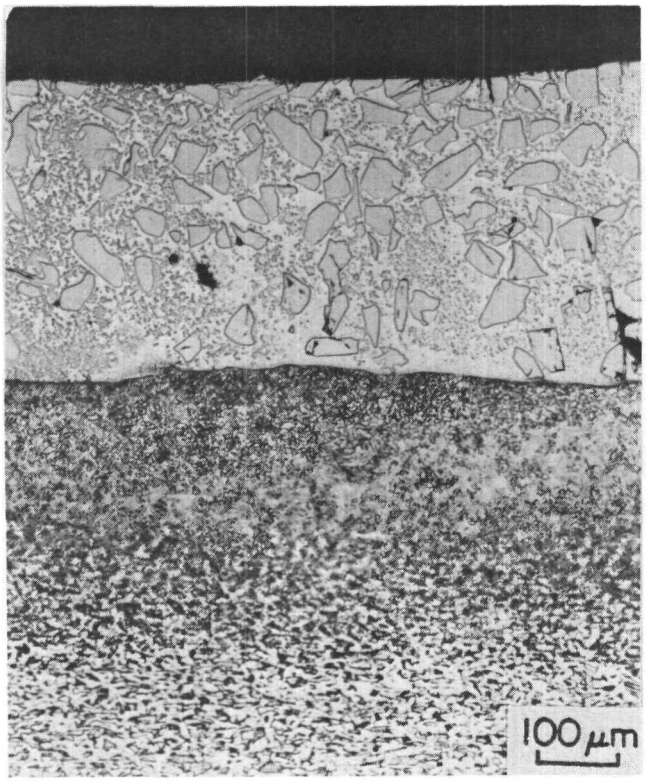

FIGURE 62. LASER-PROCESSED TiC + STELLITE 6 POWDER COATING ON COLD-ROLLED 1018 STEEL SUBSTRATE

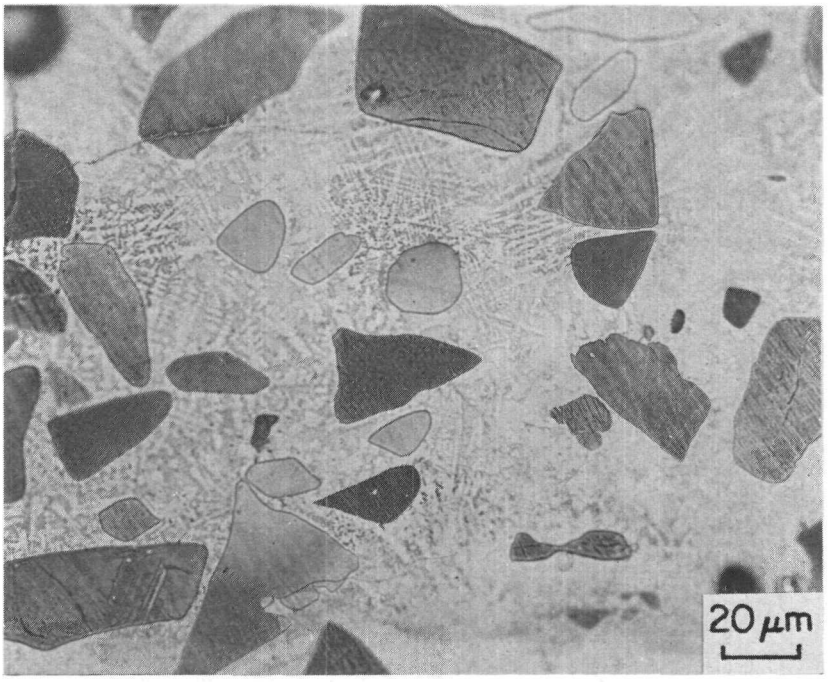

FIGURE 63. TUNGSTEN CARBIDE + STELLITE 6 MIXED POWDER COATING (ELECTROLYTIC CHROMIC ACID ETCH)

mixture. Cracks were observed in all cases down to process speeds as low as 10 mm/sec (25 inch/min.)

The general conclusion of these experiments was that WC had an embrittling effect on the matrix alloy by virtue of its dissolution in the melt and that solid solution strengthening is important to the solidified layer. The effect decreased the capacity of the overlay to relieve the solidification stresses and greatly increased cracking tendencies. For that reason, tungsten carbide composites do not appear promising as overlay coatings. TiC, on the other hand, did not seem to increase the brittleness of the overlay coating. The differences probably lay in the tendency of TiC to precipitate out of the melt on cooling rather than remain in solution.

III.3.1.4 Erosion Behavior. Results of erosion testing of some of the laser-modified materials, under less severe conditions than those used for screening cermets and ceramics, are listed in Table 13. In general, little or no superiority was found compared to the starting alloys. Figures 64 and 65 for Stellite 6B indicate that, even in the modified test, the laser-affected zones had been completely penetrated. Figure 65 also illustrates the erosion mode of this material; the chromium-rich carbides are eroded at a slower rate than the alloy matrix, so that removal of matrix eventually reveals carbide particles, which gradually protrude from the surface and then influence the erosion pattern by shielding the matrix immediately downstream from further erosion.

The TiC-Stellite 6B coating performed slightly better than unmodified Stellite 6B. Although the spacing of the large TiC particles was in many areas closer than that of the large chromium-rich carbides in Stellite 6B, the former were cracked (Figure 66a) and susceptible to loss of loosened pieces to the slurry. It is not known how much of the cracking resulted from the laser treatment, since in some areas the carbides appeared almost crack-free (Figure 66b).

Refinements of this technique to increase the volume fraction of TiC in the surface layer would obviously be beneficial. However, this type of

TABLE 13. LASER-PROCESSED MATERIALS, MODIFIED TEST[a]

Material	Max depth (μm)	Remarks
Stellite 6B (standard)	80	Co-30Cr-4W-1C, wrought plate
6B + single laser pass	147	
6B + double laser pass	101, 106	
Stellite 12 - low speed pass	322, 366	Co-30Cr-8W-1.5C, weld deposit; surface ground after laser processing
Stellite 12 - high speed pass	271	Co-30Cr-8W-1.5C, weld deposit; surface ground after laser processing
Stellite 1, as laser melted	34-84	Co-30Cr-12W-2.5C, weld deposit
Stellite 1, surface ground	189	Co-30Cr-12W-2.5C, weld deposit
(Stellite 6 + TiC) coating	74	Fairly low volume fraction of hard particles; eroded by same mode as wrought Stellite 6B

[a] Test conditions: Wilsonville product dissolved in anthracene oil to give 8 wt. percent solids; 56 m/sec (185 ft/sec), 315 C (600 F), 20° for 10 min.

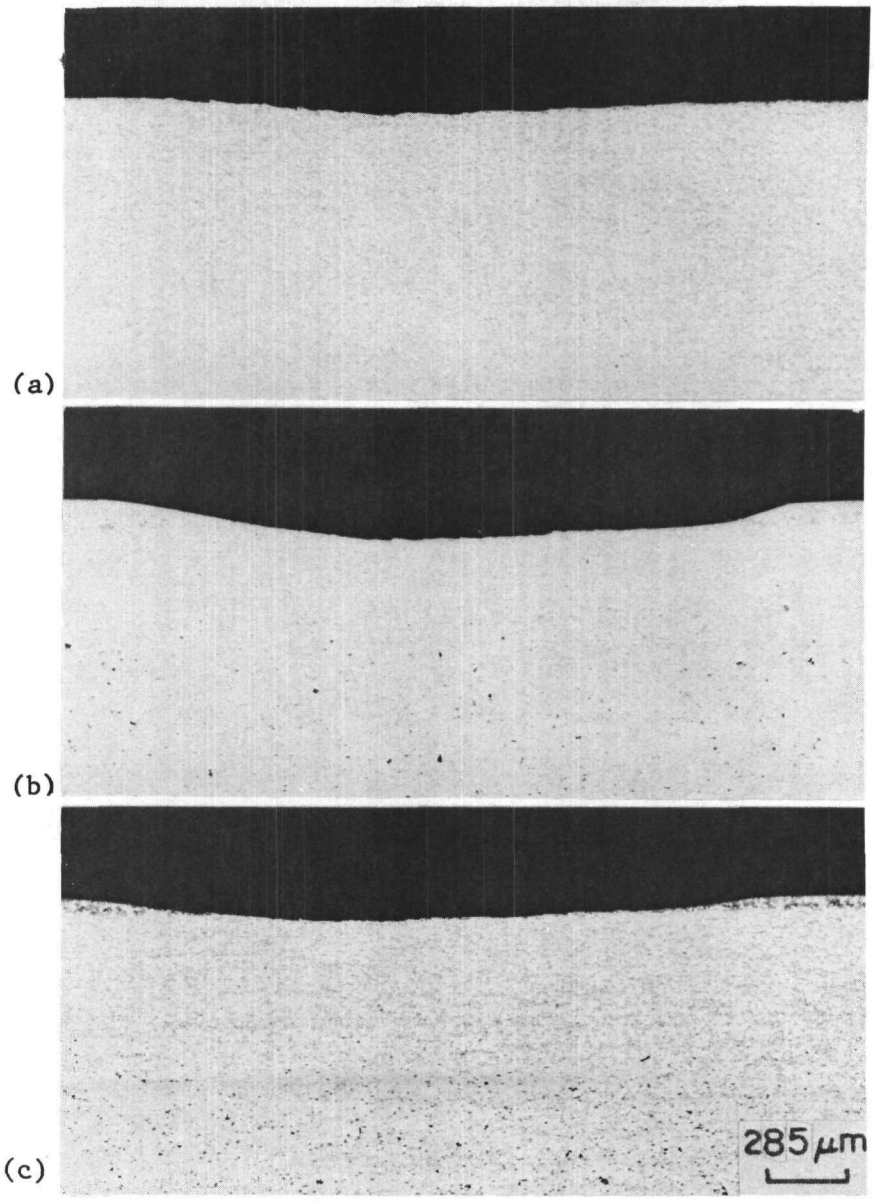

FIGURE 64. EROSION CRATERS ON LASER-MODIFIED STELLITE 6B SURFACES (SLURRY JET ENTERED AT LEFT)
(a) Standard Wrought Alloy
(b) Single Laser Pass
(c) Double Laser Pass

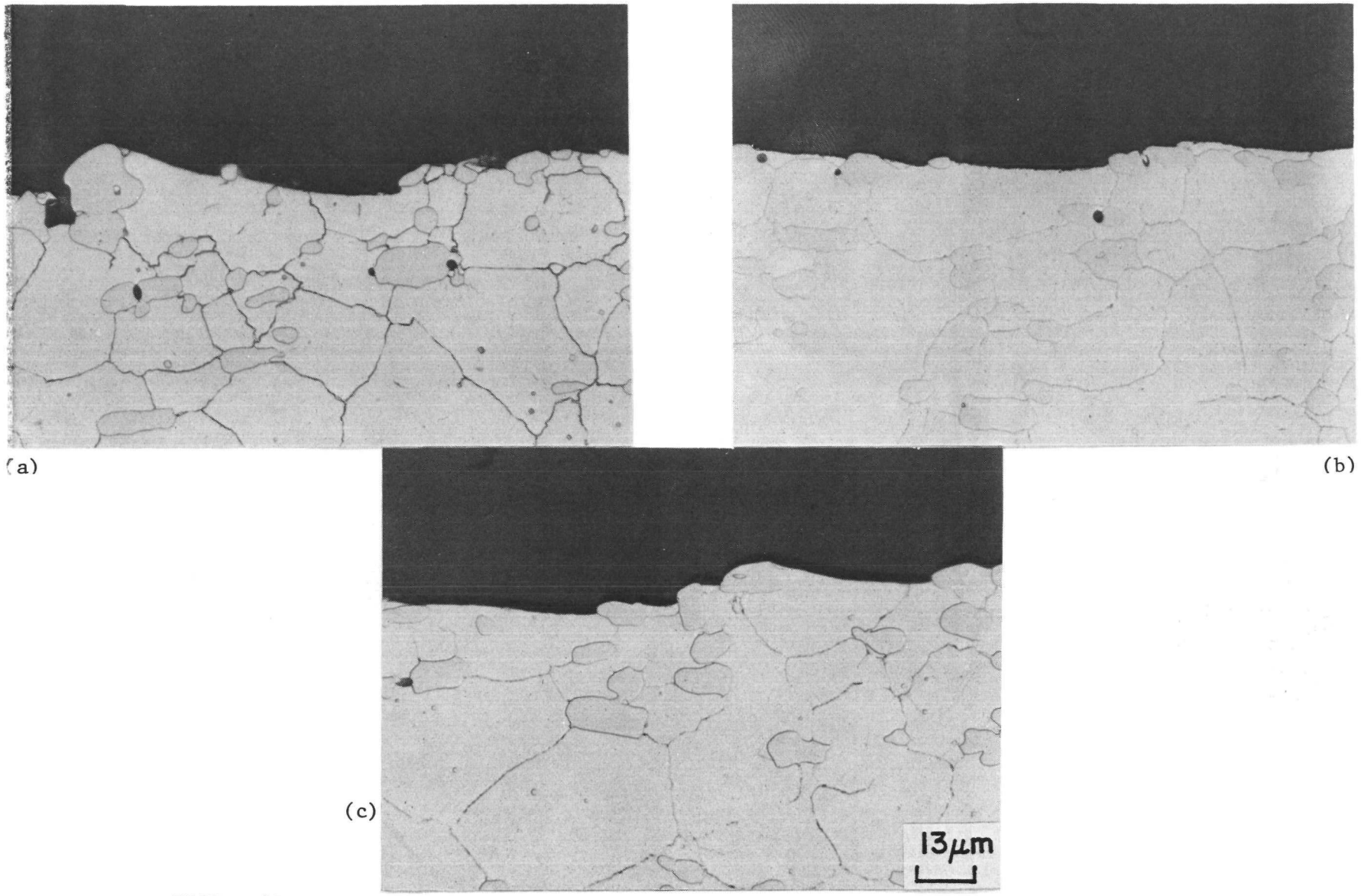

FIGURE 65. DETAILS OF ERODED SURFACES ON LASER-MODIFIED STELLITE 6B
(a) Standard Wrought Alloy, (b) Single Laser Pass, (c) Double Laser Pass

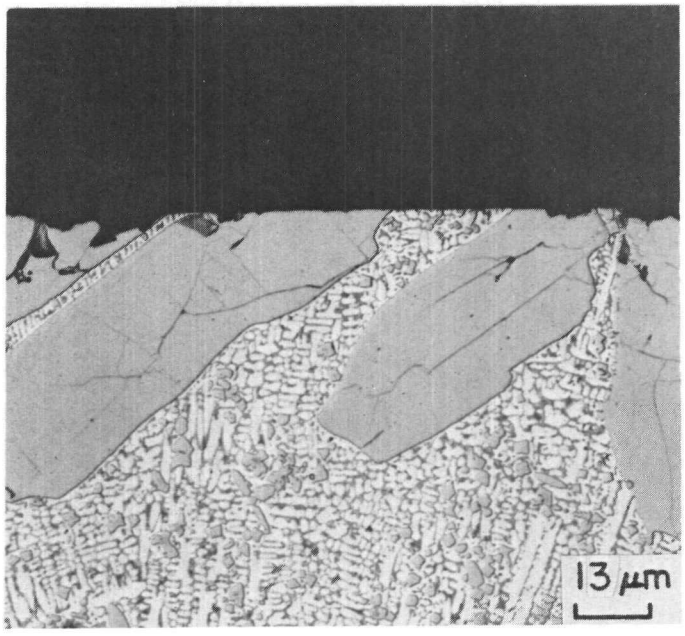

(a)

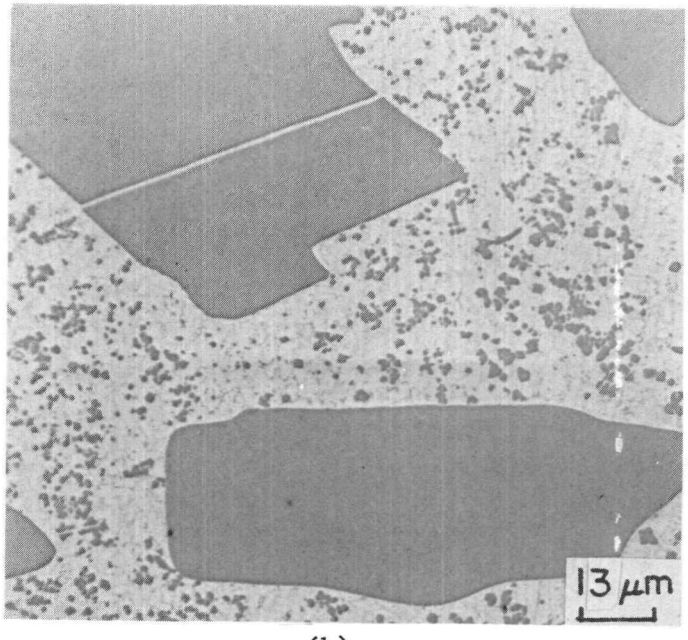

(b)

FIGURE 66. STRUCTURE OF LASER-FUSED PRE-PLACED STELLITE 6 + TiC POWDER

(a) Structure at Surface, Showing Cracking in Carbides
(b) Structure in Body of Coating

coating structure already suggests promise for use in sliding wear applications, in which the large carbides act as "lands" on which the majority of the sliding contact is borne.

III.3.2 Chemical Vapor Deposition of Silicon Carbide

SiC coatings prepared in earlier work were determined to have a laminar structure consisting of dense, apparently structureless layers separated by a porous band presumed to be the result of dust inclusion.[3] The erosion/behavior of the SiC was observed to be degraded by the porous bands. Accordingly, the effort described here was made in an attempt to prepare SiC free of this laminar structure.

III.3.2.1 Apparatus. The apparatus used to prepare the previous SiC[3] samples consisted of a horizontally positioned quartz tube (50 mm ID) and suitable fixturing for (a) the introduction of the SiC precursor, methyltrichlorosilane (MTS), and hydrogen, and (b) the venting of reaction by-products. The approach for preparing SiC was to thermally decompose MTS on a rotating (6 rpm), heated graphite (Stackpole 2020 grade) substrate (~13 mm x ~13 mm x ~130 mm). The graphite substrate was positioned in a radiofrequency (rf) coil with its long axis parallel to the long axis of the horizontal quartz tube. The graphite tube was heated using rf to minimize the formation of gas-phase-nucleated SiC particles (SiC dust), which would be expected to be incorporated in the SiC coating on the graphite, and hence result in an undesirable SiC morphology. In an effort to prepare a uniformly thick coating along the long axis of the graphite substrate, a closed end quartz tube (feed tube), positioned parallel with and below the long axis of the graphite substrate, was used to introduce MTS. The feed tube was slotted so that the gas flow was directed perpendicular to the long axis of the graphite substrate. Analysis of this approach suggested that the laminar structure developed in the SiC might have resulted from SiC dust falling onto the side of the graphite substrate farthest from the feed tube; when this side was rotated closer to the feed tube, the dust was coated with dense SiC.

Accordingly, the preliminary runs (BCL Lot 34568-76-1A and -83-2) in the current program were made using a coater similar to the one discussed above, except that the chamber was vertical instead of horizontal. This was intended to allow a minimal amount of SiC dust to "settle out" on the graphite substrate, compared to the previous horizontal configuration.

III.3.2.2 CVD Processing. The experimental conditions (Table 14) used to perform the first run were similar to those used to prepare the SiC sample which showed good erosion properties in the previous study, except that the coating chamber was vertical. Visual inspection of the prepared SiC suggested that the SiC had a growth cone structure; such a structure is not atypical of CVD-SiC. Metallography confirmed that the growth cone structure was present and that the SiC possessed some voidage, especially at the intersection of growth cones. Few growth cones were observed on the edges of the graphite.

The next SiC sample was prepared at ~1600 C (BCL Lot 34568-83-2) as opposed to ~1500 C, to test the assumption that the growth cones could be minimized by increasing the mobility of the deposited SiC during deposition. Examination of the SiC indicated that growth cones and associated voids in the SiC were still present and not well adhered to each other. Further review of the coating procedures did not suggest any obvious modifications of the approaches used which would eliminate the growth cones. Accordingly, it was decided to revert to the horizontal mode used to prepare samples during the previous program.

Four runs (34568-88-3, -90-4, -91-5, and -93-6) were performed in the horizontal mode in an effort to develop correlations between SiC process parameters and SiC performance. To obtain baseline data, the first run (BCL Lot 34568-88-3) was accomplished using the experimental conditions used to prepare the SiC sample which exhibited good performance in the previous program. Inspection of the prepared SiC indicated that growth cones were present (Figure 67a,b), but that they were well adhered to the graphite, and to each other, and that the growth cones appeared to be smaller in diameter compared to those typically obtained in the vertical coater. There were very

TABLE 14. SUMMARY OF EXPERIMENTAL DATA ON THE DEPOSITION OF SiC ON GRAPHITE

BCL Lot	MTS Flowrate (g/min)	mole percent MTS	Coating Time (hr)	Nominal Deposition Temperature (C)	System Pressure (atm)	Nominal Deposition Rate (mil/hr)	Deposition Efficiency (%)
34568-76-1A	94.3	11.3	~2 1/4	~1500	~1	~27	58.5
-83-2	123.7	14.3	~2	~1600	~1	~37	42.4
-88-3	78.2	9.5	~2	~1500	~1	~25	68.6
-90-4				- RUN ABORTED -			
-91-5	27.3	3.3	~7	~1500	~1	~11	70.8
-93-6	95.0	22.1	~2 1/4	~1500	~0.5	~25	55.6

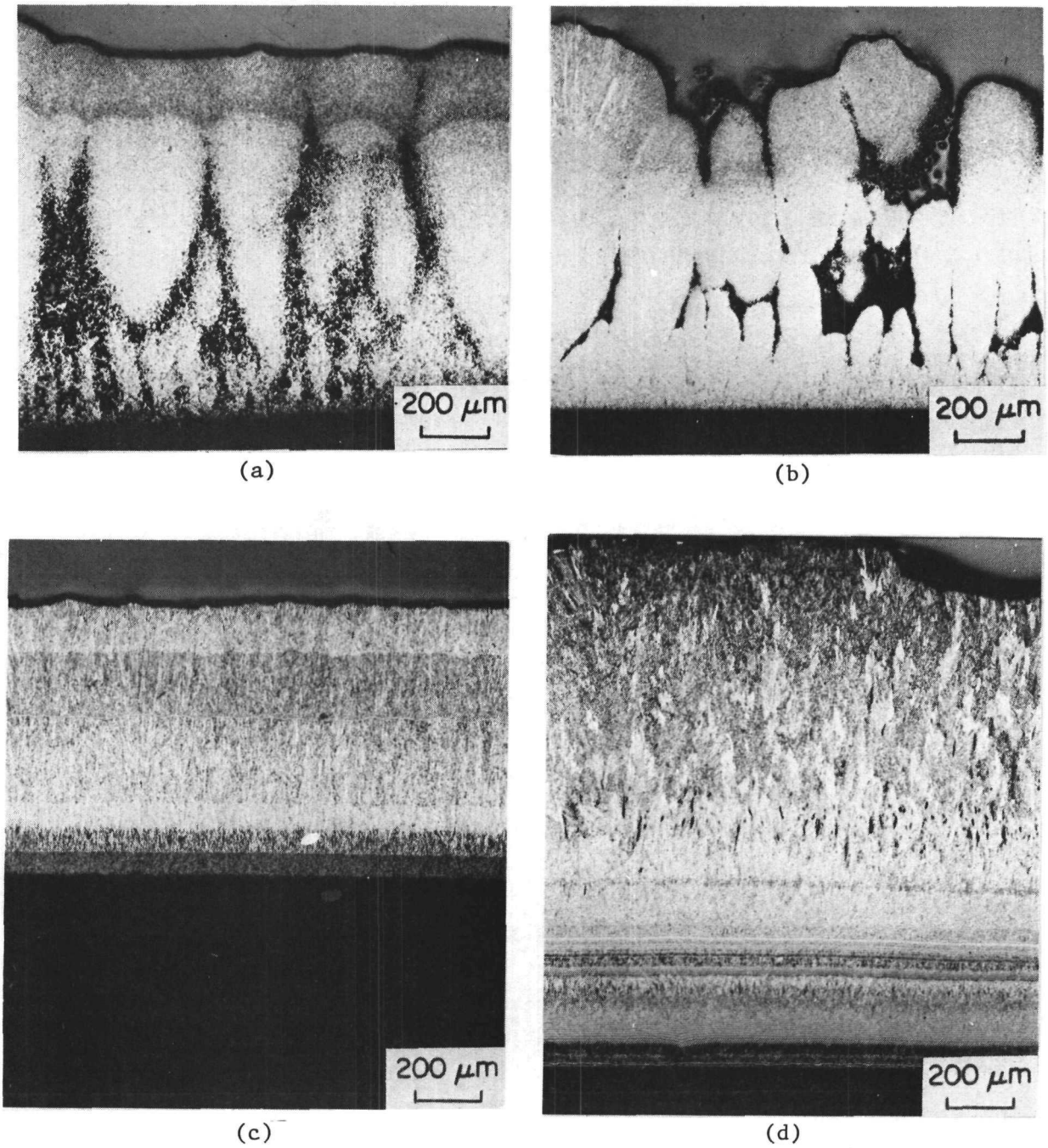

FIGURE 67. CROSS SECTIONS OF CVD SiC
(a) and (b) 34518-88-3
(c) 34568-91-5
(d) 34568-93-6

few growth cones on the edges of the substrate similar to that noted above for coatings prepared in a vertical system. Some voids were observed metallographically in the SiC, but were probably associated with pull out of dust inclusions during polishing.

The process parameters used to prepare BCL Lot 34568-91-5 were similar to those used to prepare BCL Lot 34568-88-3, except that the concentration of MTS was lower during the preparation of Lot -91-5. It was presumed that a lower MTS concentration would result in less supersaturation of the gas stream and hence result in less SiC dust being formed and trapped in the SiC coating. As would be expected, since the MTS concentration was low, the coating time was proportionally longer to prepare the target SiC coating thickness of ~1.3 mm. Inspection of the prepared SiC indicated that growth cones were present (Figure 67c), but on the average they appeared to be smaller and less predominant compared with BCL Lot 34568-88-3. One end of the prepared sample was significantly thicker (~3.8 mm) than target, presumably due to a non-optimum gas distribution pattern, which could be easily corrected. The thicker end appeared to have a larger density of growth cones compared to the portion of the specimen with a SiC thickness closer to target. Metallography of the end having a thickness closer to target showed that the coating appeared to have minimal voids.

The next run (BCL Lot 34568-93-6) was performed to preliminarily evaluate a trade-off between coating rate and coating quality. The data for BCL Lot 34568-88-3 and -91-5 suggested that slow coating rates (i.e., low MTS concentration) may improve coating quality by reducing the supersaturation of the gas stream; however, the coating time may be economically prohibitive. Another approach to reducing supersaturation in the gas stream would be to operate the coating system at reduced pressure. Hence the approach used for the next run was to operate at reduced pressure (~51 kPa) and at MTS concentration sufficiently high that it was expected that the coating rate would be similar (0.65 mm/hr) to the baseline run, (BCL Lot 34568-88-3). The target coating rate of 0.65 mm/hr was achieved. Visual inspection of the SiC indicated that the outer surface was relatively smooth and hence relatively free of large size growth cones. Furthermore, the color of the SiC coating

appeared to be variable. Examination of metallographic mounts prepared from sections from both ends of the specimen further indicated a change in the character of the SiC from one end to the other end. A ring structure was noted in the SiC mount prepared from the downstream end of the graphite (Figure 67d), while none was detected in the upstream end. It is expected that some of the rings close to the graphite might reflect a problem early in the run associated with establishing a steady system of 51 kPa. The rings further out from the graphite may reflect unintentional changes in the coating conditions. Some voids were observed in both the SiC mounts. The extent of these voids appeared to be comparable to, or slightly greater than, that in the SiC prepared as BCL Lot 34568-88-3. This observation seems to indicate that the system pressure was not low enough for the MTS concentration used, and consequently gas-phase nucleation of dust was not significantly reduced.

Conclusions drawn from this investigation are:

- SiC prepared on graphite substrates in a horizontal coater appeared to be better adhered to the graphite, to have growth cones which were smaller in size, and to contain fewer voids due to dust inclusions, than SiC prepared in a vertical coater.
- The quantity of voids due to dust inclusions in prepared SiC specimens appeared to decrease as the SiC coating rate decreased.
- Preparation of SiC at reduced pressure appeared to show some promise for improving surface smoothness of deposited SiC, and potentially minimizing dust formation.
- Deposition efficiencies at 1500 C were typically 55 to 70 percent.
- Deposition efficiency and MTS concentration appeared to be inversely related. This might be expected since less premature reaction of MTS is expected at low MTS concentrations.

III. 3.2.3. Erosion Testing. Results of erosion testing in the standard slurry test are presented in Table 6. The specimens of Lots 34568-93-6 and -91-5, with the structures shown in Figure 67c and d, exhibited more

resistance to erosion than the standard K 701 reference by factors of ~6 and 3, respectively. This is of the same order of magnitude of improvement as that measured previously for a batch of CVD SiC having a fully laminar structure, in which the erosion rate appeared to be controlled by loss of a porous or cracked phase. Presumably similar considerations apply to the present CVD SiC samples, in which the structure of the surfaces contacted by the slurry was more randomly heterogeneous than in the previous laminar structures.

III.3.3 Hot Isostatic Pressing

The erosion rates of the as-received B_4C material (Norton Norbide) have been found to be higher than expected, based on hardness, although they are consistent with other materials when based on the hardness/fracture toughness combined parameter.[3] Examination of the eroded surfaces indicated that microstructural features such as residual porosity may be contributing to these high rates. If this is the case, elimination of this porosity or other inhomogeneities in the microstructure could improve the wear properties. This could be accomplished by hot isostatic pressing (HIP) of the B_4C.

A coupon of B_4C was HIPped in a laboratory HIP unit. Because of the high strength of the material, high temperature and pressure conditions were applied in the HIP cycle; 190 MPa at 2000 C with a 1-hour hold. The microstructure of the coupon before HIP treatment is shown in Figure 68a. In addition to the equiaxed grain structure, which has an average size of ~9 μm (line intercept), a dark phase (or porosity) was evident, predominantly at grain boundaries. After HIP treatment the dark phase was still present (Figure 68b), and ranged in size and shape from very small (< 1 μm) dispersed particles to elongated flakes some 40 μm long by 2 μm wide. The etched microstructure, Fiugure 68c, shows that the dark phase was still mostly located at grain boundaries, but that intragranular location was also possible. The grain size of the HIP-processed B_4C was found to have increased to ~12 μm.

Analysis of the dark phases using an X-ray dispersive attachment on a scanning electron microscope did not reveal any detectable elements. Boron

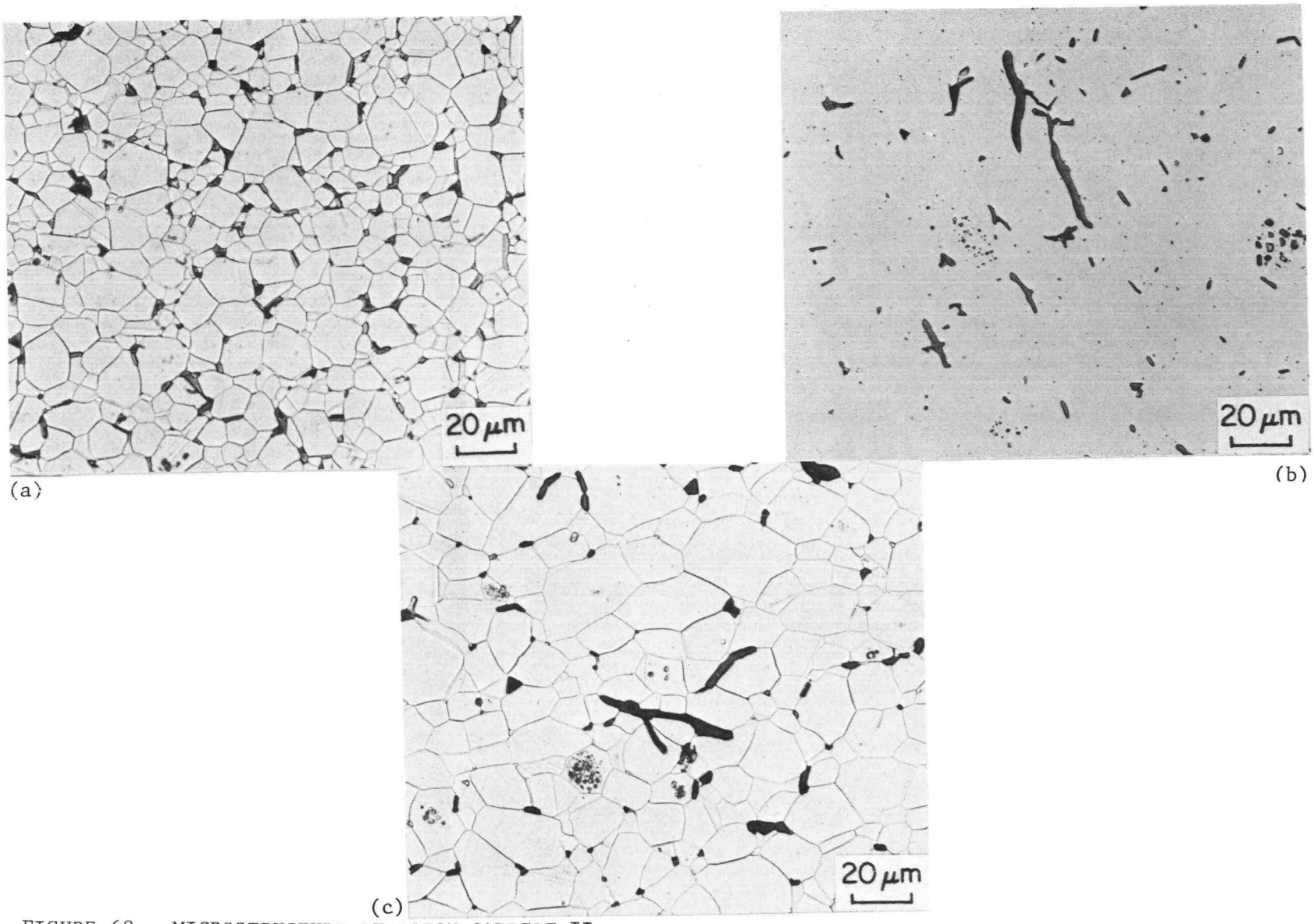

FIGURE 68. MICROSTRUCTURE OF BORON CARBIDE II
(a) As Received, Etched; After Hot Isostatic Pressing, (b) Unetched, (c) Etched.

and carbon are both undetectable by this technique. Hence the dark phase inclusions may be residual carbon, or a different form of carbide.

Erosion results for the HIP processed material in the standard erosion test were not significantly different from the as-received material. The results are reported in Table 5. Hence, if the erosion resistance of this material is to be improved, alternative means of processing to minimize or eliminate the inclusions is probably required.

IV. GENERAL DISCUSSION

Examination of the eroded surfaces of the many candidate valve materials following coal slurry erosion testing has provided information that can be usefully employed to design microstructures for improved wear resistance. In two-phase systems, such as cemented WC-Co, diamond-Si-SiC, and reaction-bonded SiC, the binder is clearly more susceptible to wear and, thus, controls the wear rate of the composite, at least in the initial stages. This suggests that reduction of the binder level is one approach to improving the wear resistance of the composite. This is partly true, as observed, for example, in the cemented-WC system. Grades with lower binder levels exhibited better erosion resistance, but this trend did not persist indefinitely with decreasing binder level. Below an optimum binder level the erosion rate increased with increasing hardness. This optimum binder level for maximum erosion resistance appeared to be approximately 5-6 percent, as inferred from the data on K 703 grade. The mechanism of erosion of the low binder level grades, K 602 (~1.5 percent by weight) and K 11, must be different from the high binder level grades. It is known from microstructural characterization studies that continguity of carbide particles, i.e., the fraction of the total surface area of the carbides shared by other carbides, increases rapidly at low binder levels. Hence, cracking of the carbide-carbide interfaces and intergranular failure is a likely mechanism of wear in the low-binder grades. Such a mechanism is characterized as brittle erosion and the mechanical

property controlling the erosion resistance in this regime is the fracture toughness. This interpretation is consistent with the experimental results at high hardness levels, where the erosion rate increased with increasing hardness, i.e., decreasing binder level and fracture toughness.

The trend of erosion resistance of cemented carbides with hardness may, therefore, be described as a transition in erosion behavior from one of ductile erosion involving deformation processes at high-binder levels, to a brittle, intergranular erosion mechanism at low-binder levels. Although the details of the erosion mechanisms are yet to be determined, the trend of the erosion rates with the key mechanical properties--hardness and fracturetoughness--are consistent with some of the established theories of erosion. Thus, optimization of hardness and fracture toughness with a fully dense microstructure appears to be the key to achieving maximum erosive wear resistance in these two-phase, cemented-WC systems.

Interestingly, in two other cermet systems (B_4C-Co, and B_4C/SiB_4-Ni or Co) a trend to increased erosion resistance with increased binder content was observed over a binder range of about 2 to 10 percent. In these cases, the degraded erosion resistance at lower binder levels resulted from porosity or unfilled interstices between the grains of the cemented phases. Variation of the size range of the cemented phase to achieve better packing seems an obvious route to improvement of some of these materials.

Evaluation of the erosion behavior of single-phase, monolithic ceramics and coatings tested in this program revaled three basic modes of material removal:

- Ductile cutting and/or ploughing
- Intergranular failure
- Elastic-plastic indentation and fracture.

Soda-lime glass in the crater periphery region provided the clearest evidence of a ductile cutting mechanism of wear (Figure 52d). Material removal was by a cutting action of the impinging particle in a manner very similar to those postulated in the well-known theories of ductile erosion by particle impingement.[17,18] As discussed in Section III.2.1 the volume loss by the cutting mechanism is expected to be inversely proportional to the

target hardness and is most efficient at small angles of particle impingement (Equation 1). Both of these conditions were satisfied with a glass target (low hardness, H ~5 GPa) and crater periphery location where particles tend to impact at small angles because of the stream-line effect.

A group of polycrystalline ceramics also exhibited a wear mechanism that might be loosely characterized as ductile wear. This included α-SiC, B_4C, hot-pressed Al_2O_3 and some coatings, such as CVD-SiC and CVD-TiB_2. The wear behavior of these ceramics was characterized as ductile because the eroded surfaces were smooth without any evidence of brittle chipping or cracking. The magnitude of the wear rates observed for these materials was small and this was consistent with the high hardnesses of these targets (Equation 1). Although the erosive wear processes in these materials were characterized as ductile, specific mechanisms of material removal could not be clearly established. Scanning-electron microscopy at high magnification did not reveal particle trajectories on the target surface, as noted for soda-lime glass. Instead, the surfaces were covered with features at a very fine scale that appeared to be small surface "humps" (Figures 69a and 69b). It could not be ascertained, however, whether these features resulted from local fluctuations in erosion rate or whether they were the result of an entirely different mechanism of wear. Irrespective of the nature of the mechanism, one of its strong characteristics was an apparent insensitivity to changes in slurry velocity (Figure 53).

The microstructure of the polycrystalline ceramic targets had a significant influence on the severity of the ductile wear. The most dramatic of these influences was the apparent sensitivity of the ductile wear rate to crystallographic orientation as noted in sintered α-SiC targets. The preferential wear of some of the grain faces of α-SiC was rationalized as due to intrinsic anisotropy of target properties, primarily hardness. Hot-pressed B_4C and hot-pressed Al_2O_3 did not exhibit this anisotropy in wear, but they were susceptible to local enhancements in wear rates caused either by a soft second-phase (carbon-rich phase in B_4C) or grain boundary porosity. These local enhancements in erosion rates resulted in a characteristic "streak" pattern near the periphery of the craters. Performance of these ceramics is

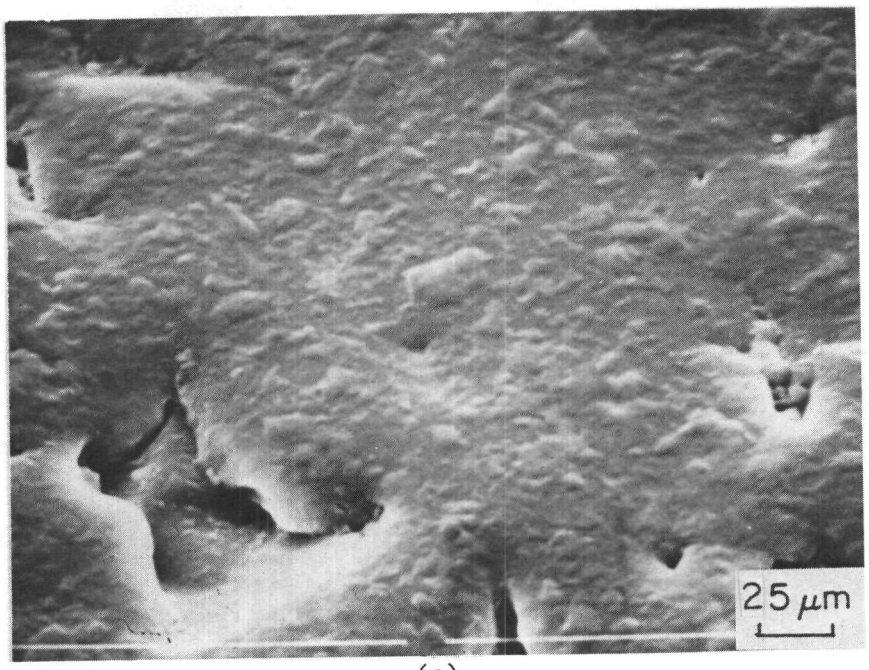

(a)

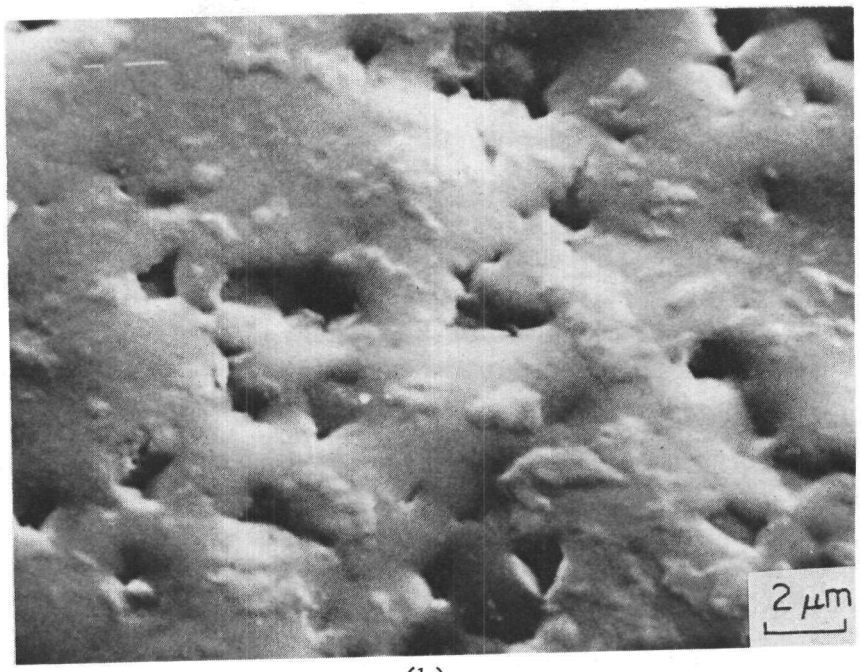

(b)

FIGURE 69. SURFACE STRUCTURE ON SLURRY-ERODED TARGETS OF (a) Hot-Pressed B_4C and (b) Hot-Pressed Al_2O_3

likely to improve with fabrication techniques that yield better overall density, and minimize the presence of softer second phases.

Hot-pressed grades of SiC and Si_3N_4 exhibited the type of wear that is characterized as intergranular failure. The wear rates resulting from this mechanism were typically an order of magnitude greater than those caused by the ductile wear mechanisms. Another characteristic of this wear mechanism was a strong sensitivity of the wear rate to slurry velocity (Figure 53). Since sintered α-SiC and hot-pressed SiC differed only in grain shapes and grain-boundary chemistry, the different mechanisms of wear in these two materials appear to be due to different grain morphologies and grain-boundary chemistries. One hypothesis is that the enhanced grain-boundary failure and wear rate in the hot-pressed materials may be due to a glassy grain-boundary phase derived from the hot-pressing agents. The grade of Si_3N_4 studied contained MgO as a hot-pressing agent, and there is direct evidence[23] of glassy grain boundary phases in a similar grade of material. The hot-pressed SiC contained an addition of Al_2O_3 as a sintering agent, which possibly may have contributed to the formation of a grain-boundary phase. The erosive wear resistance of these ceramics may be improved if they can be fabricated to full density without the addition of glass-forming agents. Advanced fabrication techniques, such as hot-isostatic pressing, should yield ceramics with better erosion resistance. The grain-boundary failure mechanism of wear is not always associated with hot-pressed grades of polycrystalline ceramics, although that is the case with SiC and Si_3N_4 ceramics. In the case of Al_2O_3, a hot-pressed grade eroded by a ductile mode while earlier experiments with coal slurries had indicated that a sintered grade (Lucalox) eroded by an intergranular mechanism. Thus, the wear mechanism appears to be dictated by the individual material chemistry rather than by its processing history.

The third type of erosion mechanism observed in the study was the elastic-plastic indentation cracking mechanism. Although this mechanism has received most of the attention in recent studies of brittle material erosion[6], it was observed only in a limited number of targets in this study. These included soda-lime glass, sapphire[3], and some grades of alumina. The primary reason for the limited observation of the indentation fracture

mechanism of wear was the small average size of the impinging particles employed in the slurry-erosion tests. It is known from indentation fracture mechanics theory that threshold conditions for brittle cracking in a target impacted by a particle are dictated by the target material properties, K_{Ic} and H, and the impacting force of the particles. A quasi-static analysis of the indentation crack initiation event relates the minimum threshold force for cracking, F*, to target properties through the equation[6,22]:

$$F^* = w^* K_c^4/H^3 \tag{8}$$

where w* is a dimensionless constant related to the details of the contact stress field. A high fracture toughness and a low hardness favor a high threshold force for cracking and hence reduce the potential for erosion by the elastic-plastic indentation fracture mechanism. Under these conditions erosion occurs by the less severe ductile cutting mode of erosion. Conversely, low fracture toughness and/or high hardness targets like soda-lime glass and sapphire would require a small threshold impact force to generate indentation cracks. This explains the indentation fracture mode of material removal in these targets in the slurry-erosion tests.

V. CONCLUSIONS

Conclusions which may be drawn from the results described are:

- Cemented tungsten carbides with a binder level in the range of 5-6 percent exhibited the best resistance to erosion for this class of materials.
- Hardness and fracture toughness control the erosion behavior of cemented tungsten carbides, and a binder level of 5-6 percent represents the best compromise of these properties for erosion resistance.
- Other practical cermet materials which exhibited erosion resistance comparable to the best cemented tungsten carbides were diamond - Si/SiC, Al_2O_3-B_4C-Cr, and B_4C-Co. For the former, erosion resistance increased with increasing volume fraction of diamond particles; for the latter the erosion resistance increased with increased binder content over the range of 2 to 8 percent.
- A sample of SiAlON exhibited erosion resistance equivalent to the best WC-cermet.
- The only coating system to show promise of a significant increase in erosion resistance over the best WC-cermet in the standard slurry erosion test was CVD TiB_2 on cemented TiB_2-Ni. Similar coatings on cemented WC and TiC eroded to depths similar to the uncoated reference WC cermet.
- Cracking and/or spalling of a TiC coating and a proprietary TMT coating occurred in the standard slurry erosion test.
- Ranking of cemented tungsten carbide materials in the laboratory erosion test was the same as that found for the same specimens in service in the Wilsonville pilot plant.
- Specimens from the Fort Lewis pilot plant which performed well in service exhibited low rates of erosion and developed similar erosion morphologies in the laboratory test.

- A substitute slurry, based on silica particles in a hydraulic oil and intended to provide a convenient and well-controlled substitute for the coal-derived slurry used for erosion testing, was found to be 2-4 times more erosive than the latter for a solids content of 8 percent by weight.
- Ranking of materials in the substitute slurry was nearly identical to that in the coal-derived slurry, with a few exceptions.
- Three modes of erosion were characterized: ductile cutting; elastic-plastic indentation and fracture; and intergranular fracture. The particular mode of erosion of a given material was closely related to its microstructure, hence processing route.
- In the substitute slurry, the angle-dependence of erosion of two forms of SiC, hot-pressed and sintered, were qualitatively very similar, but the absolute rates of erosion were quite different with the sintered material eroding slower.
- The velocity-dependencies of erosion of these two materials were very different, with velocity exponents of 2.5-3.2 for the hot-pressed, and 0.2-0.3 for the sintered. The former values correspond to those predicted by applicable erosion theories; the latter are unusually low.
- Laser fusing of preplaced powder mixtures can produce cermet-like structures with potential for erosive and sliding wear resistance. Structures of TiC particles in a Stellite 6 matrix proved less prone to cracking during this processing procedure than did WC particles, in the same matrix.

VI. REFERENCES

(1) G. Sorrell, "Materials Experience in the EDX Liquefaction Systems", Proceedings of the Sixth Annual Conference on Materials for Coal Conversion and Utilization, Gaithersburg, MD (October, 1981).

(2) T. L. Dahl, "Coal Liquefaction Letdown Valve Operating Experience at Coal Liquefaction Pilot Plants", presented at the 4th Annual SCIEP-DOE Seminar on Instrumentation and Control for Fossil Energy Processes, Clearwater Beach, FL (1982).

(3) I. G. Wright, et al, "Evaluation of Advanced Materials in Laboratory Tests and Pilot Plant Service for Use in Liquefaction Letdown Valves", DOE Final Report, DOE/ET/13537-T3.

(4) I. G. Wright, A. H. Clauer, D. K. Shetty, and T. R. Tucker, "Evaluation of Advanced Materials for Slurry Erosion Service", work in progress on ORNL Subcontract No. 85X-69611C (1982).

(5) C. B. Finch, V. J. Tenerey and R. M. Curlee, "Erosion Behavior of CVD TiB_2 Coatings on TiB_2-Based Ceramic Substrates in High-Velocity Coal-Oil Slurries", in Proc. Int. Conf. on Recent Developments in Specialty Steels and Hard Materials, Pretoria, South Africa, Nov. 8-12, 1982 (Pergamon Press, in press).

(6) A. W. Ruff and S. M. Wiederhorn, "Erosion by Solid Particle Impact", in Erosion, Treatise on Materials Science and Technology, Vol. 16, C. M. Preece, Ed., pp 69-124 (1979).

(7) J.L. Chermant, A. Deschanvres and A. Iost, "Fracture Mechanics, Statistical Analysis and Fractography of Carbides and Metal Carbide Composites", in "Fracture Mechanics of Ceramics, Vol. 1: Concepts, Flaws and Fractography", R. C. Bradt, P.P.H. Hasselman and F. F. Lange, Eds., Plenum Press, NY (1973).

(8) I. Finnie, "The Mechanism of Erosion of Ductile Metals", Proc. 3rd U.S. National Cong. of Appl. Mechanics, p. 527 (1958).

(9) H. C. Lee and J. Gurland, "Hardness and Deformation of Cemented Tungsten Carbide", Mat. Sci. and Eng., 33 pp 125-133 (1978).

(10) J. R. Pickens and J. Gurland, "The Fracture Toughness of WC-Co Alloys Measured on Single-edge Notch Beam Specimens Precracked by Electron Discharge Machining", Mat. Sci. and Eng., 33 pp 135-142 (1978).

(11) D. K. Shetty, I. G. Wright, and A. H. Clauer, "Coal Slurry Erosion of Reaction-Bonded SiC", Wear, 79, pp 275-279 (1982).

REFERENCES
(Continued)

(12) K. Miyoshi and D. H. Buckley, "Anisotropic Tribological Properties of SiC", Wear, 75, pp 253-268 (1982).

(13) Private Communication with N. Ault, Norton Company, December (1981).

(14) J. L. Routbort and R. O. Scattergood, "Anomalous Solid-Particle Erosion Rate of Hot-Pressed Silicon Carbide", J. Am. Ceram. Sec., 63 (9-10), pp 593-595 (1980).

(15) D. K. Shetty, I. G. Wright, A. H. Clauer, J. H. Peterson, and W. E. Merz, "Erosive Wear of Advanced Ceramics in Coal-Slurry Streams", Corrosion-NACE, 38 (9), pp 500-509 (1982).

(16) A. G. Evans, M. E. Gulden, and M. Rosenblatt, "Impact Damage in Brittle Materials in the Elastic-Plastic Response Regime", Proc. R. Soc. London, Ser. A, 361, pp 343-65 (1978).

(17) I. Finnie, A. Levy, and D. H. McFadden, "Fundamental Mechanisms of the Erosive Wear of Ductile Metals by Solid Particles", Erosion: Prevention and Useful Applications, ASTM STP 664, W. F. Adler, Ed., ASTM, pp 36-58 (1979).

(18) I. M. Hutchings, "Mechanisms of the Erosion of Metals by Solid Particles", Erosion: Prevention and Useful Applications, ASTM STP 664, W. F. Adler, Ed., ASTM, p 59-76 (1979).

(19) G. L. Sheldon and I. Finnie, "On the Ductile Behavior of Nominally Brittle Materials During Erosive Cutting", Trans. ASME, J. Eng. Ind., 88, pp 387-392 (1966).

(20) J. A. Coppola, M. Srimivasan, K. T. Faber, and R. H. Smoak, "High Temperature Properties of Sintered Alpha Silicon Carbide", Carborundum Technical Paper (1979).

(21) G. Q. Weaver and B. A. Olson, "High-Strength Silicon Carbide For Use in Severe Environments", Silicon Carbide - 1973, R. C. Marshall, J. W. Faust, Jr., and C. E. Ryan (Ed.), Proc. 3rd Int. Conf. on SiC, Miami Beach, Florida, September (1973).

(22) S. M. Wiederhorn and B. Lawn, "Strength Degradation of Glass Impacted with Sharp Particles: I. Annealed Surfaces", J. Amer. Ceram. Soc., 62, 66-70 (1979).

(23) D. R. Clarke and G. Thomas, "Grain Boundary Phases in a Hot-Pressed MgO-Fluxed Si_3N_4" J. Am. Ceram. Soc. 60 (11-12) pp 491-495 (1977).

APPENDIX A

INDENTATION TECHNIQUE FOR MEASURING FRACTURE TOUGHNESS OF BRITTLE MATERIALS

APPENDIX A

INDENTATION TECHNIQUE FOR MEASURING FRACTURE TOUGHNESS OF BRITTLE MATERIALS

Introduction

The occurrence of cracks at the corners of hardness impressions, such as that produced with a Vickers diamond pyramid indenter (see Figure A1), has been observed for a long time in the hardness testing of brittle ceramics. Initially, the cracks were regarded as a nuisance and a detriment to effective hardness measurements on brittle materials. Palmqvist[1,2] was the first to recognize that the length of these cracks reflected the fracture toughness of the indented materials. He used the indent-load crack-length relation as an empirical parameter to characterize the fracture toughness of cemented carbides.

A resurgence of interest in indentation fracture occurred in the mid-seventies, following the work of Lawn and coworkers[3-5] on glass and subsequently the work of Evans and coworkers[6-8] on a number of polycrystalline ceramics. The basic principles underlying indentation fracture and the methodology of fracture-toughness evaluation emerged from their pioneering work.

Theory of Indentation Fracture and Fracture-Toughness Evaluation

Several experimental observations were instrumental in the development of the theory of indentation fracture. Chief among them was the unique relation between the radial-crack length, C, and the indentation load, P, observed in indentation experiments on a number of brittle materials:

$$C = kP^{2/3} \quad , \qquad (A1)$$

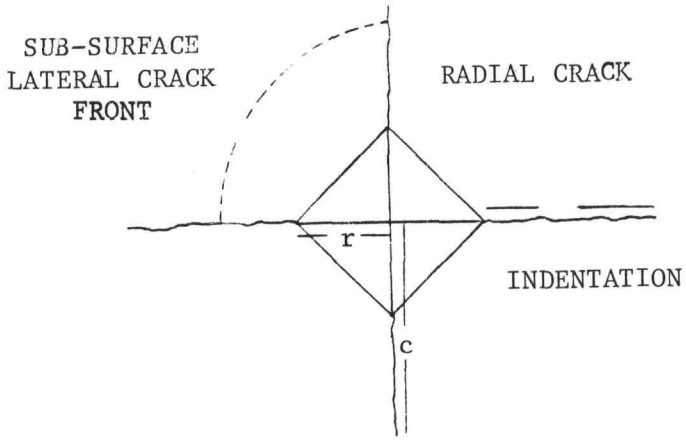

(a)

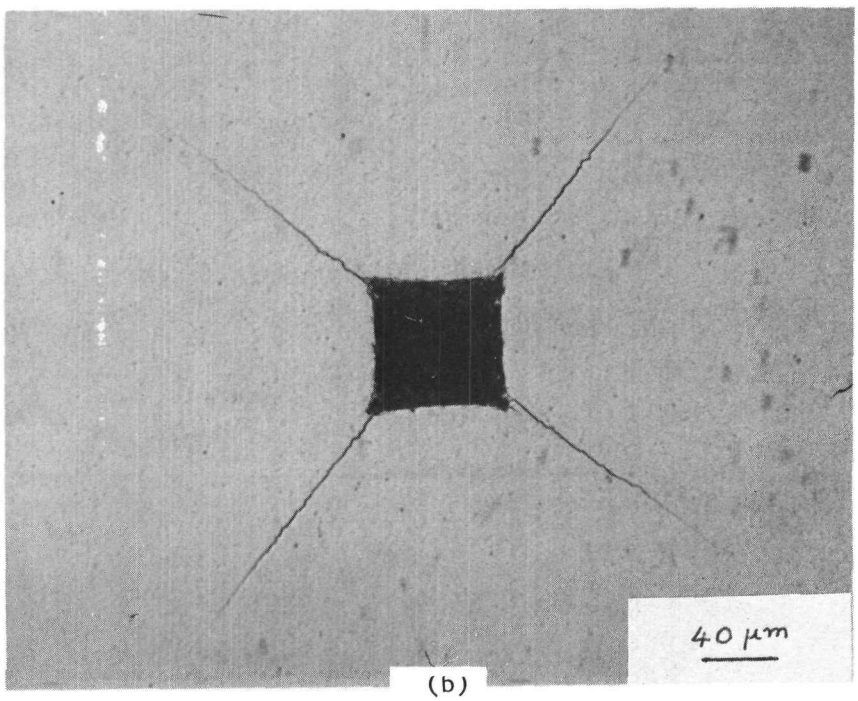

(b)

FIGURE A1. INDENTATION CRACKS INTRODUCED BY A VICKERS INDENTER (a) SCHEMATIC SHOWING THE PARAMETERS USED IN THE TEST, (b) A TYPICAL CRACK PATTERN OBTAINED IN Al_2O_3.

where the constant k was found to be a function of the properties of the indented material and the details of the contact geometry[5]. Examination of the fracture surfaces produced by extending one of the radial cracks in a post-indentation strength test revealed that the radial cracks were the surface traces of two orthogonal semicircular (half-penny) cracks, as is illustrated in Figure A2. Finally, in-situ observations of the penny-crack evolution in a transparent material revealed that a residual tensile force, caused by the wedging action of the deformation zone at the hardness impression, was primarily responsible for the equilibrium growth of the radial cracks during the unloading cycle in the indentation process. For sufficiently well-developed cracks, $C \geq r$ (where $2r$ is the diagonal of the indentation), the indenter-induced penny cracks were considered to be "center-loaded" at the deformation zone, in which case the driving force may be suitably characterized by a residual stress-intensity factor of the simple form [9]:

$$K_r = \chi_r P/C^{3/2} \quad , \tag{A2}$$

where χ_r is a material- and indenter-geometry-dependent constant that relates the load on the indenter to the point-wedging force. The fracture-mechanics interpretation of the formation of the penny cracks, as embodied in Equation A2, provides an explanation of the experimental observation of Equation A1 and is also the basis for evaluating fracture toughness, K_{Ic}. It is assumed that the crack system is subject to conditions of mechanical equilibrium, both during and after the contact event, such that the radial cracks remain stable at $K_r = K_c$. Denoting C_o as the crack dimension appropriate to the post-indentation equilibrium configuration, one obtains:

$$K_c = \chi_r P/C_o^{3/2} \quad . \tag{A3}$$

Two different approaches have been suggested for evaluating χ_r, the parameter that characterizes the residual crack-driving force. In one approach, the residual crack-driving force is calculated by assuming that the

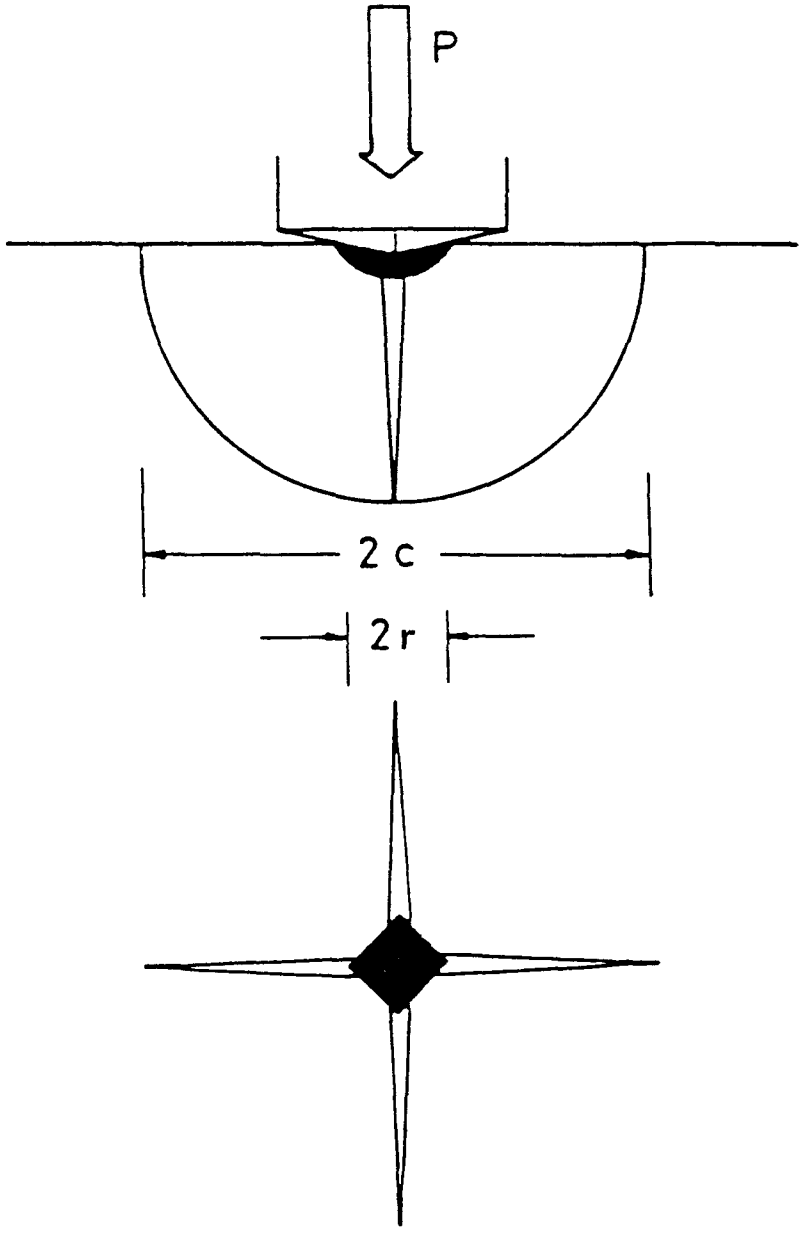

FIGURE A2. SCHEMATIC OF VICKERS-PRODUCED INDENTATION-FRACTURE SYSTEM, PEAK LOAD P, SHOWING CHARACTERISTIC DIMENSIONS c AND a OF PENNY-LIKE RADIAL/MEDIAN CRACK AND HARDNESS IMPRESSION, RESPECTIVELY. (From Ref. 11)

volume of the hardness (plastic) impression is accommodated by the surrounding elastic matrix[10]. This approach leads to:

$$\chi_r = \zeta_V^R \quad (E/H)^{1/2} \quad , \tag{A4}$$

where

E = Young's modulus of the material

H = Hardness of the material

ζ_V^R = A material-independent cp constant for a given indenter geometry, such as Vickers.

Substitution of Equation A4 in Equation A3 leads to a relation that can be used for fracture-toughness evaluation provided that a proper value for the constant, ζ_V^R, can be established. Anstis et al[11] established a mean value, $\zeta_V^R = 0.016 \pm 0.004$, for the standard Vickers' diamond pyramid indenter by calibrating indentation-fracture-toughness values for a number of reference ceramics against fracture-toughness values measured by conventional techniques. This calibration leads to the following final equation for fracture toughness:

$$K_{Ic} = 0.016 \ (E/H)^{1/2} \ (P/C_o^{3/2}) \tag{A5}$$

Equation A5 can be rewritten in terms of only the variables that are measured in a typical indentation test, as follows:

$$K_{Ic} = \frac{0.0235 \ E^{1/2} \ P^{1/2}}{Co} \ r \ . \tag{A6}$$

Evans[8] treated the residual stress field of an indentation by making an analogy with the elastic-plastic solution for a spherical cavity subjected to an internal pressure. He derived an equation for fracture toughness based on dimensional arguments and empirical curve-fitting of fracture-toughness data for a number of ceramics. In the large-crack-length range ($C_o \geq 3r$), his equation reduces to[12]:

$$K_{Ic} = \frac{0.036\ E^{0.4}\ P^{0.6}\ r^{0.8}}{C_o^{1.5}} \qquad (A7)$$

In summary, Evans' equation (Equation A7) was derived on empirical grounds, and it fits the fracture-toughness data more closely. This is to be expected, however, since the functional form of the equation was adjusted to fit the data. The equation derived by Lawn, Evans, and Marshall[10] (Equation A6) was based on more rigorous, theoretical grounds, but it does not fit the data for different materials so well as does Equation A7.

Fracture Toughness Evaluation of Candidate Valve Materials

Figures A3, A4 and A5 show indentation-fracture data obtained for cemented carbide (K 701),a hot-pressed grade (Norton NC-132) of Si_3N_4 and a hot-pressed grade (AVCO) ofAl_2O_3, respectively. The size of the semi-circular surface crack, C_o, and the indentation half-diagonal, r, are plotted versus the indentation load, P, on a log-log plot. The plots are linear and the slopes of the lines are consistent with the expected relations:

$$P\ C_o^{-3/2} = \text{constant} = Z \qquad (A8)$$

and

$$0.4636\ P\ r^{-2} = \text{constant} = H \qquad (A9)$$

It should be noted that observations of the relations of Equations A8 and A9 are evidence of characteristic values of the material properties, fracture-toughness (K_{Ic}) and hardness (H), respectively. The optimum values of the constants Z and H were obtained by least-squares linear regression using the expected slopes and calculating the intercepts. K_{Ic} values were calculated by substituting the values of the constants Z and H in Equation A5 along with a value of the modulus, E, reported by the supplier of the commercial grade materials. The calculated fracture toughness and hardness values and their 95 percent confidence limits are indicated in the figures.

The fracture toughness of the hot-pressed grade of Si_3N_4 has been measured by a number of investigators using a variety of techniques. The

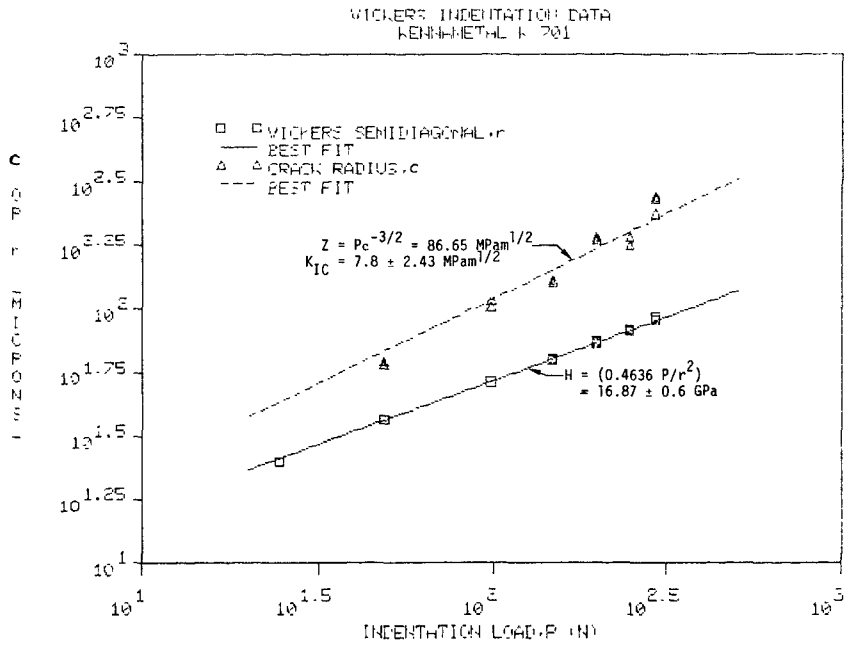

FIGURE A3. VARIATION OF SEMICIRCULAR SURFACE CRACK SIZE, Co, AND INDENTATION HALF-DIAGONAL, r, WITH INDENTATION LOAD, P, FOR CEMENTED CARBIDE (KENNAMETAL K 701)

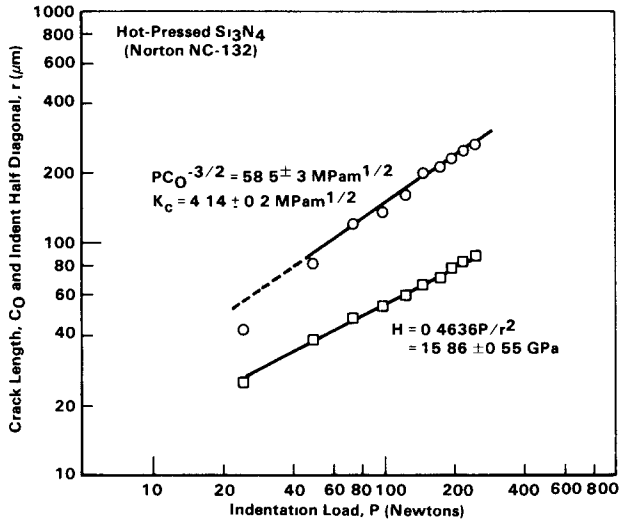

FIGURE A4. VARIATION OF SEMI-CIRCULAR SURFACE CRACK SIZE, C_o, AND INDENTATION HALF-DIAGONAL, r, AS A FUNCTION OF INDENTATION LOAD, P, FOR HOT-PRESSED Si_3N_4 (NORTON NC-132)

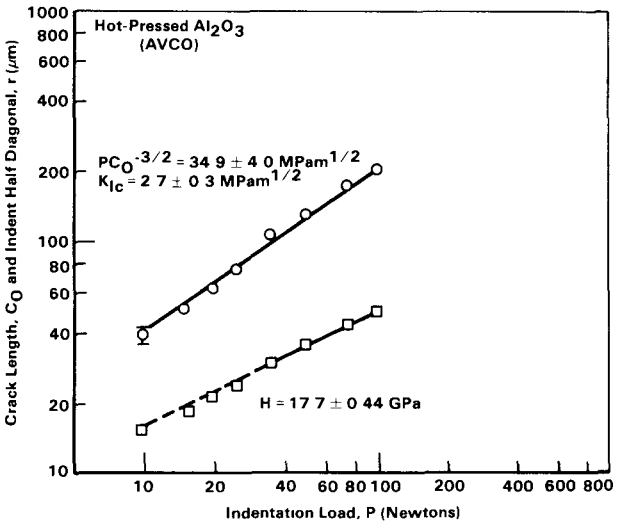

FIGURE A5. VARIATION OF SEMI-CIRCULAR, SURFACE CRACK SIZE, C_o AND INDENTATION HALF-DIAGONAL, r, AS A FUNCTION OF INDENTATION LOAD, P, FOR HOT-PRESSED Al_2O_3 (AVCO)

reported K_{Ic} values, listed in Reference 13, are in the range 3.6 - 4.5 $MPam^{1/2}$. Thus, the value measured in the present study, $K_{IC} = 4.14 \pm 0.2$ $MPam^{1/2}$, is in good agreement with the reported data. Bansal and Duckworth[14] have measured a value of $K_{Ic} = 4.19$ $MPam^{1/2}$ for the hot-pressed grade of Al_2O_3 using the double torsion test technique. The value measured by the indentation method, in this study, $K_{Ic} = 2.7 \pm 0.3$ $MPam^{1/2}$, is, therefore, significantly lower. This difference can, however, be rationalized in the following manner. The hot-pressed grade of Al_2O_3 is probably one of the brittle materials in a class that exhibits a behavior referred to as "crack growth resistance curve". In these materials K_{Ic} is a function of the crack size, increasing with crack size and saturating at a value characteristic of the bulk material at large crack sizes. The indentation technique yields lower values of K_{Ic} in these materials because of the small sizes of the cracks relative to the large cracks in fracture mechanics specimens like the double-torsion specimens.

There is no independently reported value for K_{Ic} of the cemented carbide (Kennametal K 701). The accuracy of the value measured by the indentation technique could not be assessed. However, the K_I value appears to be reasonable since it compares well with the K_{Ic} values of cemented carbides of similar hardness.

The indentation technique was applied to characterize the fracture toughness of a number of candidate valve materials. Fracture-toughness values obtained on some of the materials are listed in Table A1. The technique, however, was not applicable to all the materials. Sintered B_4C (Norton Norbide) and a hot-pressed SiC (Norton NC-203), for example, showed severe chipping under the indenter. The indentation technique has several unique advantages as well as limitations. These are discussed in the following section.

Advantages and Limitations of the Indentation Technique

The indentation technique has two unique advantages. It can be applied to very small specimens, and it is capable of measuring the local

crack-growth resistance of a material, for example, the microtoughness pertinent to cracks with lengths on the order of the microstructural dimensions. The technique is particularly useful for evaluating the fracture toughness of surface coatings, which normally are not thick enough for use of the conventional techniques.

Some guidelines can be suggested for the minimum specimen size that can be used in indentation measurements of toughness. The minimum specimen thickness generally is dictated by the requirement that the thickness/crack-depth ratio be large enough so that the lower-free-surface effects can be neglected. A specimen thickness that is 10 times the crack depth generally meets this requirement. Indentation-crack depths generally do not exceed 200 μm. Thus, a specimen thickness of 2 mm is a useful minimum-thickness specification. Surface dimensions of the specimen are dictated by the number of indentations to be used and the minimum spacing of indentations. For an upper-bound surface-crack length of $2C_o$ = 400 μm, a minimum indentation spacing of 2 mm is recommended in order to avoid crack interactions. For an arbitrarily selected minimum of four indentations per material, the above guidelines translate to a minimum specimen size of 6 x 6 x 2 mm.

There are a number of limitations to the indentation technique that must be considered before applying it in any material-evaluation program. The technique is useful in those situations where relative-fracture-toughness values rather than absolute values are of interest. The technique is not expected to measure fracture-toughness values at absolute accuracies greater than 30 percent. One indication of this is the difference in the toughness values predicted by Equations A6 and A7. Equation A7 typically predicts a K_{Ic} value that is 30 percent greater than that based on Equation A6. This difference may be attributed to the approximations involved in the treatment of the elastic-plastic indentation stress field and the description of the indentation crack as a center-point-loaded half-penny crack. The analysis also neglects any interaction between the two orthogonal half-penny cracks. In principle, the indentation analysis is strictly valid for large values of (C_o/a) where the center-point-loading approximation is justified. In experiments this is achieved in the case of materials with high hardness and low

toughness. But experiments of Anstis and coworkers[11] and Evans[8] show that reasonable toughness measurements can be obtained when (C_o/a) is as low as 2 for such materials as glass and cemented tungsten carbides. It also should be noted that calculation of K_{Ic} from either Equation A6 or Equation A7 requires a knowledge of the modulus, E. Any errors in the value of the modulus used in the calculations would add to the uncertainties in the values of toughness calculated. In material-development programs, however, one is more interested in the relative variation of the toughness with processing or heat-treatment variables. In these situations, the indentation technique can serve a useful purpose.

A second limitation of the indentation technique is that in materials that exhibit subcritical crack growth in the ambient environment, the indentation cracks can grow subcritically under driving forces, $K_r < K_{Ic}$. In these situations, the final crack lengths are greater than the equilibrium cracks assumed in the theory for $K_r = K_{Ic}$. The technique then can give underestimated values of K_{Ic}, depending on the extent of slow-crack growth. However, this is a serious problem only in the case of glasses and ceramics that contain significant amounts of glass. Even in these cases, slow-crack-growth effects can be minimized by indenting the test samples in an inert environment, for example, mineral oils that contain very low contents of water.

Residual stresses on the indented surfaces, as in tempered glasses or grinding-induced compressive stresses in ceramics, can significantly affect indentation-load/crack-length relations. The fracture-mechanics relations developed for annealed materials will no longer hold good for these materials. Either the test materials should be stress relieved by annealing or polishing, or the residual stress fields should be properly taken into account in the fracture-mechanics analyses. The latter course can be complicated in those cases where the residual stress fields are not well defined, for example, ground surfaces or chemically strengthened glasses.

Finally, the indentation techniques are not suitable for certain materials. In single-crystal materials or anisotropic materials in general, the crack symmetry and shapes can be affected significantly. In some poly-

crystalline materials, for example Al_2O_3 sintered with MgO (Lucalox), severe microcracking at the indentations prevent the development of well-developed radial cracks. This problem is particularly severe when the grain size approaches the hardness-indentation size. Generally, the indentation technique is satisfactory for grain sizes less than 5 μm and radial-crack sizes greater than at least 10 grains. The indentation technique is also not applicable to some glasses. Certain anomalous glasses, for example high-silica glasses, densify under indentation, rather than deform plastically and, therefore, do not develop radial-crack systems.

REFERENCES TO APPENDIX A

(1) S. Palmqvist, Jernkontorets Ann., 141, 300 (1957).

(2) S. Palmqvist, Archiv Eisenhuttenwesen, 33, 629 (1962).

(3) B. R. Lawn and T. R. Wilshaw, J. Mater. Sci., 10, (6), 1049-1081 (1975).

(4) B. R. Lawn and M. V. Swain, J. Mater, Sci., 10 (1), 113-122 (1975).

(5) B. R. Lawn and E. R. Fuller, J. Mater. Sci., 10 (12), 2016-2024 (1975).

(6) A. G. Evans and T. R. Wilshaw, Acta Metallurgica, 24, 939 (1976).

(7) A. G. Evans and E. A. Charles, J. Amer. Ceram. Soc., 59, 371 (1976).

(8) A. G. Evans in Fracture Mechanics Applied to Brittle Materials, ASTM STP 678, S. W. Feiman, Ed., American Society for Testing and Materials, Philadelphia, Pennsylvania, pp 112-135 (1979).

(9) G. C. Sih, Handbook of Stress-Intensity Factors for Researchers and Scientists, Institute of Fracture and Solid Mechanics, Lehigh University, Bethlehem, Pennsylvania (1973).

(10) B. R. Lawn, A. G. Evans, and D. B. Marshall, J. Amer. Ceram. Soc., 63 (9-10), 574-581 (1980).

(11) G. R. Anstis, P. Chantikul, B. R. Lawn, and D. B. Marshall, J. Amer. Ceram. Soc., 64 (9), 533-538 (1981).

(12) D. B. Marshall and A. G. Evans, J. Amer. Ceram. Soc., 64 (12), C182-C183 (1981).

(13) T. T. Shik and J. Opoku, "Application of Fracture Mechanics to Ceramic Materials - A State-of-the-Art Review", Engg. Frac. Mech., 12, pp 479-498 (1979).

(14) G. K. Bansal and W. H. Duckworth, "Effects of Specimen Size on Ceramic Strengths", in Fracture Mechanics of Ceramics, Vol. 3, R. C. Bradt, D. P. H. Hasselman and F. F. Lange (Ed.), pp 189-204 (1978).

☆U S GOVERNMENT PRINTING OFFICE 1983-646-069/623